

AD-A113 085

PANAMETRICS INC WALTHAM MASS

**F/6 9/3**

DESIGN, FABRICATION, CALIBRATION, TESTING AND SATELLITE INTEGRA--ETC(U)

DEC 81 B SELLERS, R KELLIHER, F A HANSER

F19628-78-C-0247

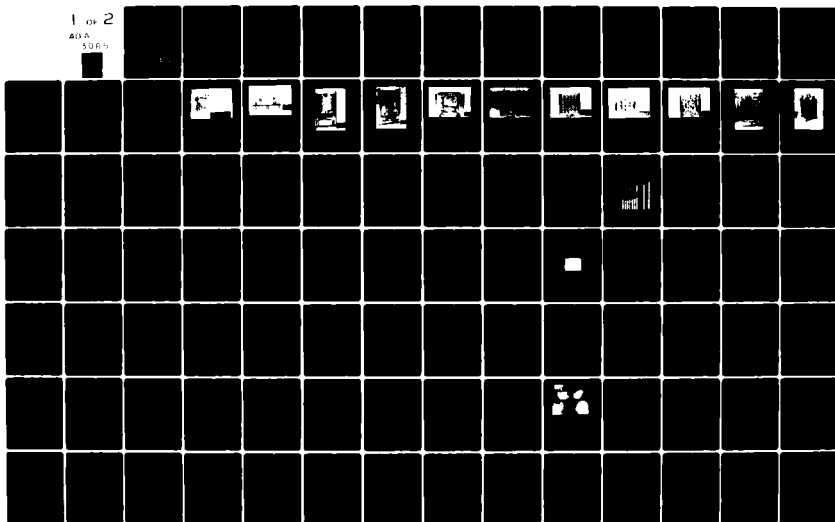
UNCLASSIFIED

AFGL-TR-81-0354

NL

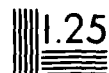
1 of 2

AD A  
3065





28 25



MICROCOPY RESOLUTION TEST CHART  
NBS 1010-A

12

AD A11 3085

AFGL-TR-81-0354

DESIGN, FABRICATION, CALIBRATION, TESTING AND SATELLITE  
INTEGRATION OF A SPACE-RADIATION DOSIMETER

Bach Sellers  
Ralph Kellher  
Frederick A. Hanser  
Paul R. Morel

Panametrics, Inc.  
221 Crescent Street  
Waltham, Massachusetts 02254

December 1981

Final Report

September 1978 - December 1981

Approved for public release; distribution unlimited.

AIR FORCE GEOPHYSICS LABORATORY  
AIR FORCE SYSTEMS COMMAND  
UNITED STATES AIR FORCE  
HANSCOM AFB, MASSACHUSETTS 01731

DTIC  
ELECTE  
APR 6 1982  
B

82 04 06 047

DTIC FILE COPY

Qualified requestors may obtain additional copies from the Defense Technical Information Center. All others should apply to the National Technical Information Service.

UNCLASSIFIED

SECURITY CLASSIFICATION OF THIS PAGE (When Data Entered)

REPORT DOCUMENTATION PAGE		READ INSTRUCTIONS BEFORE COMPLETING FORM
1. REPORT NUMBER AFGL-TR-81-0354	2. GOVT ACCESSION NO. AD-A113085	3. RECIPIENT'S CATALOG NUMBER
4. TITLE (and Subtitle) Design, Fabrication, Calibration, Testing and SATELLITE Integration of a Space- Radiation Dosimeter		5. TYPE OF REPORT & PERIOD COVERED Final Report Sept. 1978 - Dec. 1981
7. AUTHOR(s) Bach Sellers Frederick A. Hanser Ralph Kelliher Paul R. Morel		6. PERFORMING ORG. REPORT NUMBER
8. PERFORMING ORGANIZATION NAME AND ADDRESS Panametrics, Inc. 221 Crescent Street Waltham, MA 02254		9. CONTRACT OR GRANT NUMBER(s) F 19628-78-C-0247
11. CONTROLLING OFFICE NAME AND ADDRESS Air Force Geophysics Laboratory Hanscom AFB, MA 01731 Contract Monitor: Roger P. Vancour, PHG		10. PROGRAM ELEMENT, PROJECT, TASK AREA & WORK UNIT NUMBERS 62101 F 760112 AB
14. MONITORING AGENCY NAME & ADDRESS (if different from Controlling Office)		12. REPORT DATE December 1981
		13. NUMBER OF PAGES 123
		15. SECURITY CLASS. (of this report) Unclassified
		16. DECLASSIFICATION/DOWNGRADING SCHEDULE
16. DISTRIBUTION STATEMENT (of this Report)  Approved for public release; distribution unlimited.		
17. DISTRIBUTION STATEMENT (of the abstract entered in Block 20, if different from Report)		
18. SUPPLEMENTARY NOTES		
19. KEY WORDS (Continue on reverse side if necessary and identify by block number)  Dosimeter Particle Fluxes Electron Dose Nuclear Stars Proton Dose Space Radiation Dosimeter Space Radiation		
20. ABSTRACT (Continue on reverse side if necessary and identify by block number)  → A space-radiation dosimeter has been designed, fabricated, calibrated, tested, and integrated into a DMSP satellite payload. The dosimeter is primarily designed to measure the dose from electrons of greater than 1 MeV to greater than 10 MeV in four channels. Each channel has a different thickness aluminum dome shield over a silicon		

DD FORM 1 JAN 73 1473 EDITION OF 1 NOV 65 IS OBSOLETE

UNCLASSIFIED

SECURITY CLASSIFICATION OF THIS PAGE (When Data Entered)

UNCLASSIFIED

SECURITY CLASSIFICATION OF THIS PAGE(When Data Entered)

20. Abstract (Continued)

solid state detector. The solid state detector outputs are processed to provide the dose from electrons (low energy loss), the dose from protons (high energy loss), the flux of electrons, the flux of protons, and the rate of high energy loss nuclear star events. The dosimeter was extensively calibrated with nuclear radiation sources, electron beams, and proton beams. The dosimeter also has a calibration mode in which the alpha particles from a weak source behind each detector are used to check for total detector depletion and proper operation of the electronics.

UNCLASSIFIED

SECURITY CLASSIFICATION OF THIS PAGE(When Data Entered)

## FOREWORD

The work described in this report was carried out under contract to the Air Force Geophysics Laboratory, Hanscom Air Force Base, Massachusetts. The contract monitor was Dr. Roger P. Vancour of the Space Physics Group (PHG). The help of Dr. Vancour and of Dr. Paul R. Rothwell, also of the Space Physics Group, in carrying out the dosimeter project was instrumental in its successful completion. The dosimeter particle beam calibrations were carried out at the AFGL Linear Accelerator for electrons, and at the Harvard Cyclotron for protons. The help and cooperation of the personnel at these accelerators is also appreciated.

Accession For	
DATE SENT	
DATE REC'D	
BY	
DISTRIBUTION/	
Availability Codes	
Avail and/or	
Dist	Special
A	

DTIC  
COPY  
INSPECTED  
9

## TABLE OF CONTENTS

	<u>Page</u>
FOREWORD	iii
LIST OF ILLUSTRATIONS	vii
LIST OF TABLES	ix
1. INTRODUCTION	1
1.1 Overall Description	1
1.2 Review of Related Documentation	4
2. DESIGN CONSIDERATIONS	18
2.1 Basic	18
2.2 Operational Environment	19
2.2.1 Inner and Outer Zones in General	19
2.2.2 DMSP Orbit	25
2.2.3 Brief Summary	31
2.3 Dome Design	33
2.4 Dose Measurement Concept	40
2.4.1 Approximate Geometrical Factor	40
2.4.2 Separation of Electrons, Protons and Nuclear Stars	41
2.4.3 In-Flight Calibration Concept	46
2.5 Design Features	47
2.5.1 Electronic Dose Measurement Concept	48
2.5.2 Flux and Dose Capacity	51
2.5.3 Compression Counter Characteristics	55
2.5.4 Accuracy Characteristics	56
2.6 Calibration Data	58
3. DOSIMETER GENERAL DESCRIPTION	64
3.1 Physical Details	64
3.1.1 Domes	64
3.1.2 Housing	66



TABLE OF CONTENTS (Concluded)		<u>Page</u>
3.2	Electronic Design	68
3.2.1	Overall Instrument	68
3.2.2	Detection Assembly	83
3.2.3	Digitizer Board	85
3.2.4	Digital Data Board	89
3.2.5	Digital Control Board	91
3.2.6	Interface/Monitor Board	95
3.2.7	DC-DC Convertor	97
3.3	Ground Support Equipment	99
4.	OPERATIONAL DESCRIPTION	100
4.1	Calibration Constants	100
4.2	Operating Instructions	103
4.3	Environmental Precautions	105
4.4	Data Stream Format	106
5.	CONCLUSIONS AND SUMMARY	110
	REFERENCES	111

# LIST OF ILLUSTRATIONS

<u>Figure No.</u>		<u>Page</u>
1.1	Isometric View of the Energetic Particle Dosimeter	2
1.2	Cutaway View of the Energetic Particle Dosimeter	3
1.3	Detection Assembly Photo, Bottom	5
1.4	Detection Assembly Photo, Top	6
1.5	Backplane Photo, Inside	7
1.6	Backplane Photo, Outside	8
1.7	DC-DC Converter Photo, Top	9
1.8	Digitizer Board Photo	10
1.9	Digital Data Board Photo	11
1.10	Digital Control Board Photo	12
1.11	Interface/Monitor Board Photo	13
1.12	Instrument Partial Assembly Photo	14
1.13	Final Unit Photo	15
2.1	Comparison of ATS-6 with AE4 Data Base	20
2.2	Equatorial average dose rate as a function of L-shell	21
2.3	Composite equatorial radial profiles of the overall environment models for electrons with $E > 500$ keV	22
2.4	AE4 radial profile of equatorial omnidirectional flux for various energy thresholds, epoch 1967	23
2.5	Radial distribution of AP8MIN omnidirectional fluxes of protons in the equatorial plane with energies above threshold values between 0.1 and 400.0 MeV	24
2.6	Annual and Cumulative Solar Cycle 20 Proton Fluxes	26
2.7	Dosimeter Nominal Design Spectra	28
2.8	Estimated Integral Fluxes behind Aluminum Hemispherical Shields of Indicated Range Thickness for Nominal Design Spectra	29
2.9	Dome Sensor Concept	33

<u>Figure No.</u>	LIST OF ILLUSTRATIONS (Continued)	<u>Page</u>
2.10	Contribution of Electrons, Protons and Bremsstrahlung to the Total Dose-depth Curve	35
2.11	TIROS Dome Detectors	37
2.12	Results of Monte-Carlo Energy Transport Calculations for the AE4/5 and OV3-3 "Average" Spectra	38
2.13	Spectrum of Sn <sup>119</sup> with YAG-100 Diffused Junction Silicon Semiconductor Detector	39
2.14	Energy Deposition Curves for Dome 1	42
2.15	Energy Deposition Curves for Dome 2	43
2.16	Energy Deposition Curves for Dome 3	44
2.17	Energy Deposition Curves for Dome 4	45
2.18	Basic Dose Measurement System	48
2.19	Dose Counter Bit Assignments	56
3.1	Cross Section View of Dome 1	65
3.2	Detector Carrier Photo	67
3.3	Block Diagram, Energetic Particle Dosimeter	69
3.4	Detection Assembly Block Diagram (One Channel)	84
3.5	Digitizer Board Block Diagram	86
3.6	Digitizer Timing Diagram	88
3.7	Digital Data Board Block Diagram	90
3.8	4 x 4 Compression Counter	92
3.9	Digital Control Board Block Diagram	93
3.10	Interface/Monitor Board Block Diagram	96
3.11	DC-DC <del>converter</del> Block Diagram	98
4.1	Am3 Vs Temperature	104

# LIST OF TABLES

<u>Table No.</u>		<u>Page</u>
1.1	Specifications	17
2.1	Design Parameters of Dome Sensors	18
2.2	Approximate Ratio of High Energy Dome Doses to that of Dome #1 for $L = 0.0$	19
2.3	Peak and Integrated Proton Fluxes for large Solar Events May 1967 - August 1972	27
2.4	Estimated Doses Behind Aluminum Spherical Shields of Indicated Thickness for Nominal Design Spectra	30
2.5	Estimated Doses and Fluxes Behind Chosen Aluminum Hemispherical Shields for Nominal Design Spectra	31
2.6	"Peak" Fluxes in DMSP Orbit, Due to South Atlantic Anomaly	32
2.7	Energy Window Limits	47
2.8	Dose Capacity, Flux Capacity & Processing Rate Limit with Estimates of Expected Doses & Fluxes	50
2.9	Compression Counter Characteristics	58
2.10	List of Calibration Data Taken for Protons at the Harvard Cyclotron	60
2.11	List of Calibration Data Taken for Electrons at the AFGL Linac	61
2.12	Relative Response of D2 Dome for Electrons at Normal Incidence	62
2.13	Relative Angular Response of D2 Dome for 8.5 MeV Electrons	62
2.14	Relative Response of D3 Dome for Protons at Normal Incidence	63
2.15	Proton Energy Losses in the D3 Dome Detector at Normal Incidence	63
3.1	Dome Sensor Specifications	64
3.2	Digitizer Classification	68
3.3	Backplane Node List	70
3.4	Digitizer Pulse Energy Constant Vs Mode	76
3.5	Data Register Assignment	76
3.6	Data Address	77
3.7	Field Designation	78
3.8	Channel Code Vs Channel Number	79

LIST OF TABLES (Continued)		
<u>Table No.</u>		<u>Page</u>
3.9	Command, Monitor and Data Sequence	80
4.1	Dosimeter Detector Properties and Prescaler Values	101
4.2	Threshold and Digitizer Levels for the Dose Channels	101
4.3	Dose Channel Calibration Constants from Different Measurement Methods	102
4.4	Final Channel Dose Calibration Constants	103
4.5	Compression Counter Assignments for the Data	107
4.6	Breakdown of One Basic 36-bit Data Block	108
4.7	Breakdown of One Complete Cycle of Normal Mode Data	109

## 1. INTRODUCTION

### 1.1 Overall Description

The increasing use of complex solid state electronic devices in the space radiation environment makes it important to have reliable data on the radiation doses these devices will receive behind various thicknesses of shielding. As part of the effort to obtain this data a Dosimeter (the SSJ\* Dosimeter) has been designed, fabricated, calibrated, and integrated into the payload of a DMSP satellite. The Dosimeter measures the accumulated radiation dose in a silicon solid state detector behind four different thicknesses of aluminum shielding.

The SSJ\* Dosimeter described in this report was designed, fabricated, and calibrated by Panametrics, Inc. of Waltham, Mass. under contract with the Air Force Geophysics Lab. This instrument is designed to interface to the Operational Linescan System (O. L. S.) of the DMSP Spacecraft. The data registers are optimally scaled for the approximate circular 800 km orbit expected. (The basic design is, of course, adaptable to other orbits.) The instrument specifications are listed in Table 1.1.

The Dosimeter separates the total radiation dose into that from electrons (50 keV to 1 MeV energy deposits) and protons (1 to 10 MeV energy deposits). The four aluminum shields provide energy thresholds (range thickness values) of 1, 2.5, 5, and 10 MeV for electrons, and 20, 35, 51, and 75 MeV for protons. The primary measurement, and that most accurately calibrated, is the accumulated dose. Onnidirectional electron and proton fluxes are also measured, and data on the detailed response of each channel to energy and angle for electrons and protons have been obtained. There is also a high energy loss event channel which counts the rare nuclear star events caused by high energy protons, and the low flux of high energy high - Z cosmic rays. Information on these high energy loss events is important, since they can cause logic upsets or memory bit loss in some types of low power micro-circuits.

Fig. 1.1 is an isometric view of this sensor showing its top and 2 sides. The 4 domes shown on top house the solid state detectors. The dome thickness increases with the size and results in four different incident particle energy thresholds. Power is supplied through P1 and 3 analog and 3 digital housekeeping monitors are available at this connector. The telemetry (including Power Enable, Read Gate and Clock, Mode Control, Reset, Serial Data and Off Indicator) connects to P2. J12 is a test connector and is capped during flight. Fig. 1.2 is another isometric view. This view is 90° from Fig. 1.1 and is cut away to show the PC Boards and detector. The four preamp test inputs shown are also capped for flight.

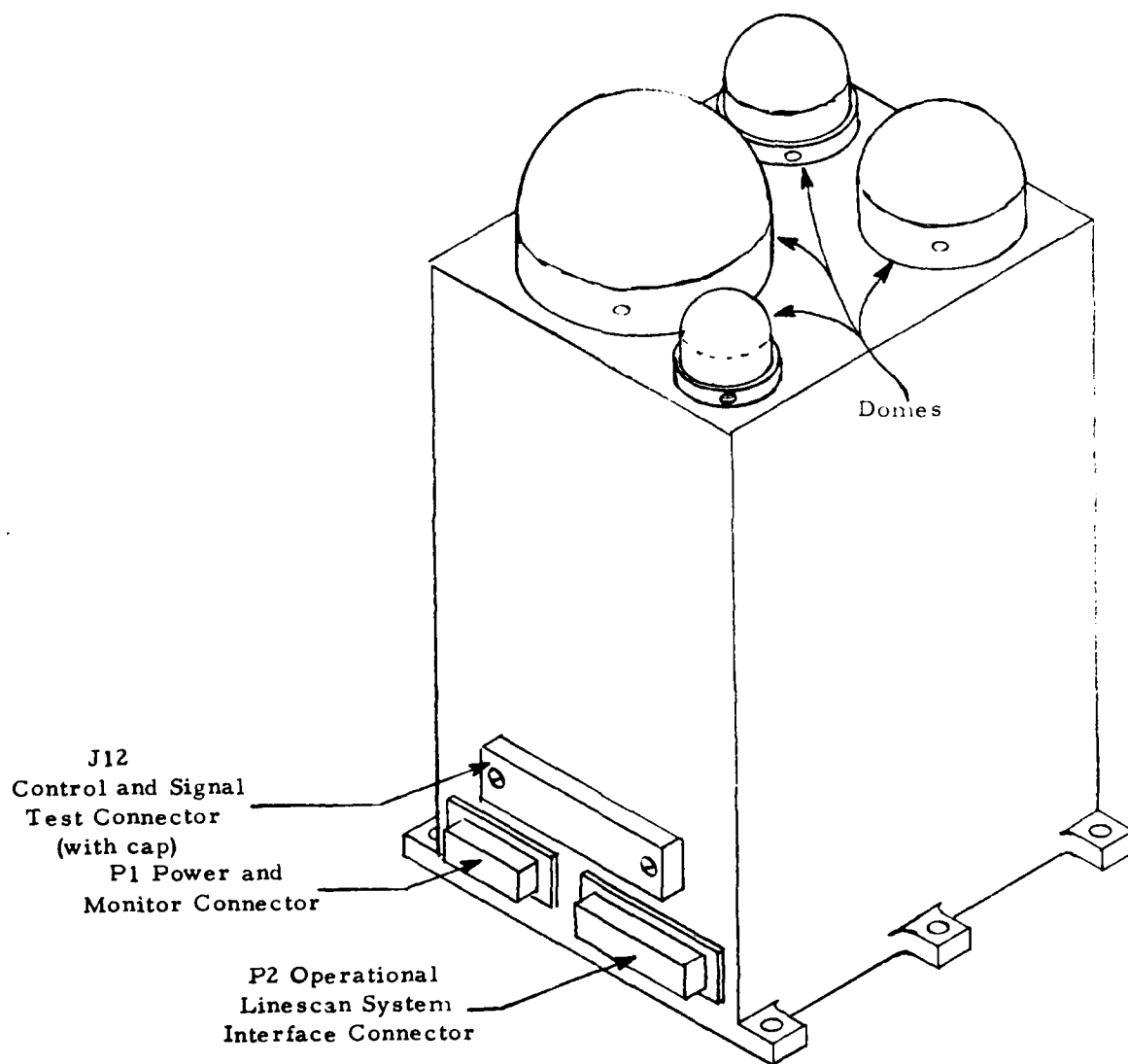


Fig. 1.1 Isometric View of the Energetic Particle Dosimeter

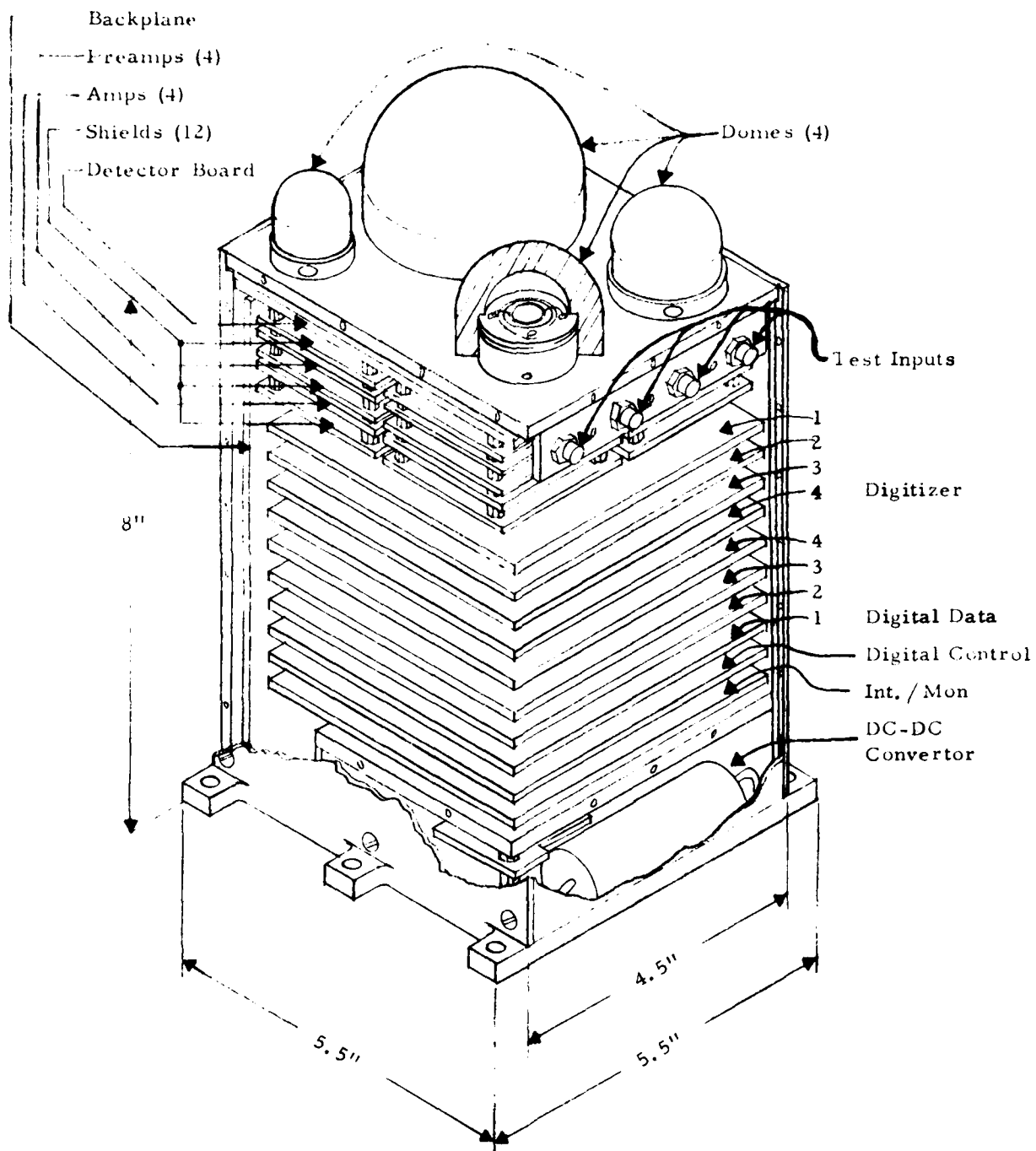


Fig. 1.2. Cutaway View of the Energetic Particle Dosimeter



The instrument components can be separated into four categories as follows: 1) The detection assembly (Figs. 1.3 and 1.4) consisting of: the top plate, including test inputs and bracket, 4 domes complete with detectors, Cal sources, and tungsten backshields, the detector board, 4 charge sensitive preamp boards, 4 shaping and star amp boards, 4 each of 3 electrostatic shields, and components and hardware as required. 2) The backplane/DC-DC convertor assembly. (Figs. 1.5 and 1.6) consisting of the backplane, three DC-DC convertor PC assemblies; the HV section, the LV section (Fig. 1.7) and the Enable and Over Voltage section, the top shield, the side shield and feedthrus, the transistor bracket, and the required hardware. 3) The PC board complement consisting of 10 full size PC boards complete with components and connectors. The boards are as follows: 4 each digitizer boards (Fig. 1.8), 4 each digital data board (Fig. 1.9), one digital control board (Fig. 1.10) and an interface and monitor board (Fig. 1.11). 4) The four side covers complete with card guides and fasteners. Fig. 1.12 is the complete instrument missing the PC board complement and the access cover. Fig. 1.13 shows the final unit.

## 1.2 Review of Related Documentation

The present report has been adapted to a significant extent from previous documents. The original technical proposal (Ref 1.1) was a response to solicitation No. F19628-78-R-0129 (Ref 1.2). This proposal, submitted on 22 May 1978, resulted in contract No. F19628-78-C-0247. At this time a review of the design considerations and a description of a simpler electron-only Dosimeter were presented.

By 3 December 1979 when the R & D Design Evaluation Report (Ref 1.3) was first submitted, the design had evolved to essentially its final form and the spacecraft's orbit and interface were known. The final design expanded on the initial electron-only version to include a higher energy-loss proton channel, and a much higher energy loss nuclear star channel. The Special Sensor/Spacecraft Interface Specification (Ref 1.4) applies to the Power Connector P1. The P2 interface was designed to the Special Sensor /OLS Interface Specification (Ref 1.5). This document was later superseded by Ref 1.6 (with the same title).

The Design Evaluation Report adapted and expanded the design considerations of the technical proposal. A detailed description of the revised electronics design was also included. This document was later revised to correct some minor details that could not be anticipated at the time the report was first issued.

Shortly before delivery of the Dosimeter, Westinghouse issued the Electrical Interface Test (Ref. 1.7). This test was performed at Westinghouse in Baltimore, Maryland and reported in the Technical Operating Report (Ref 1.8).

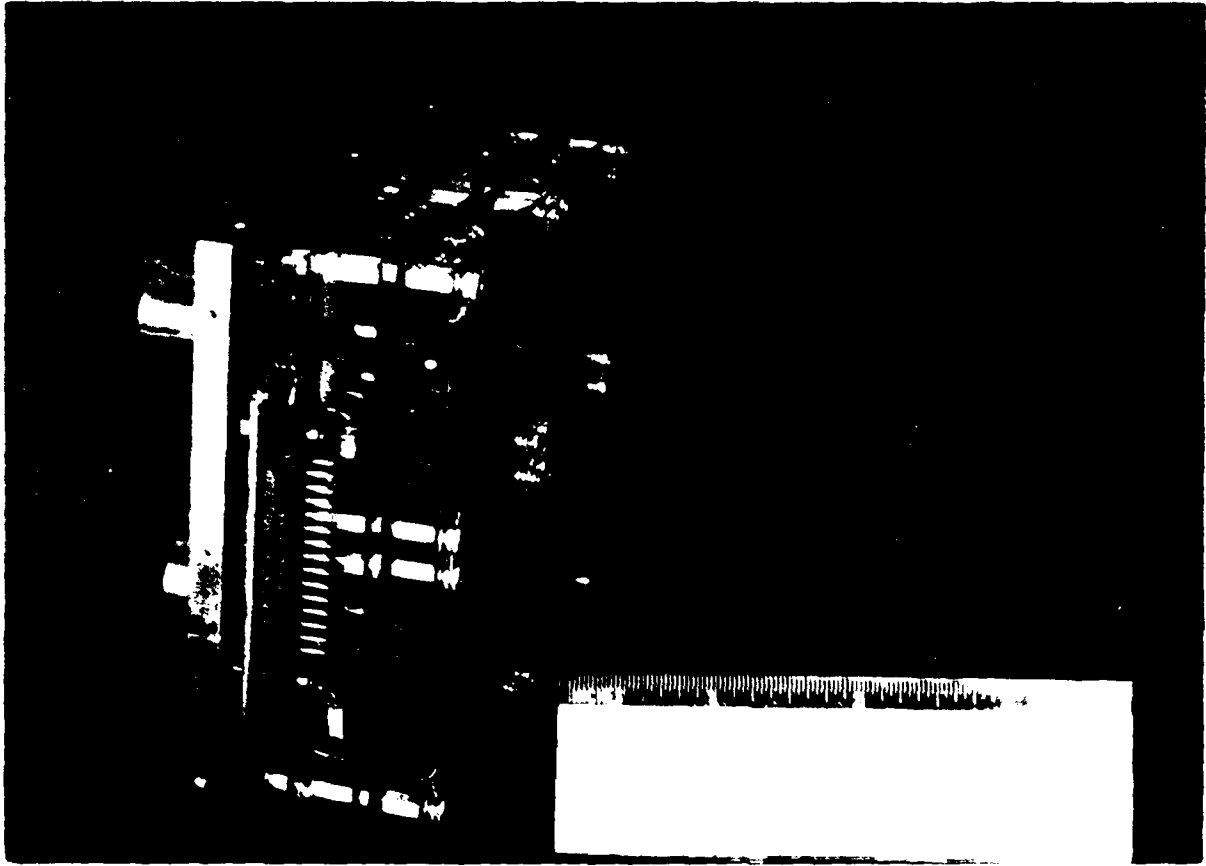


Figure 1.3. Detection Assembly Photo, Bottom.

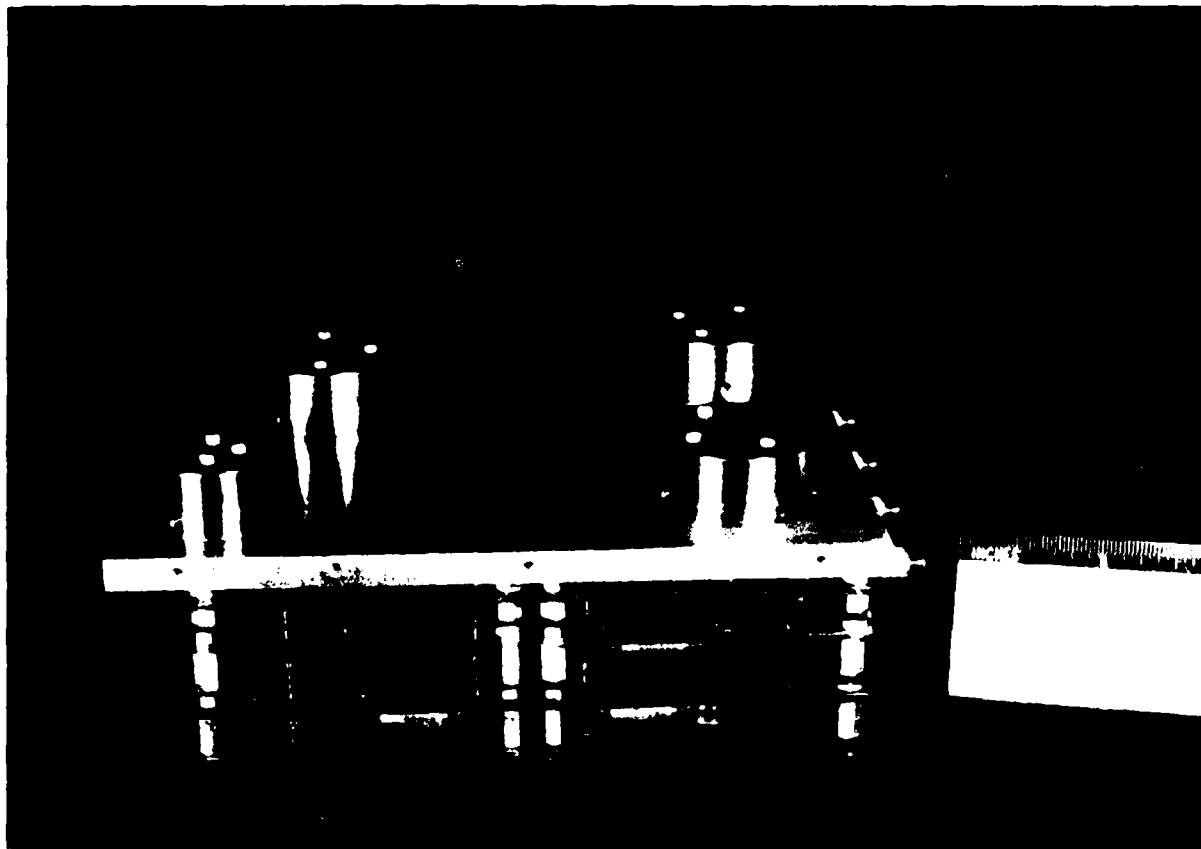


Figure 1.4. Detection Assembly Photo, Top.

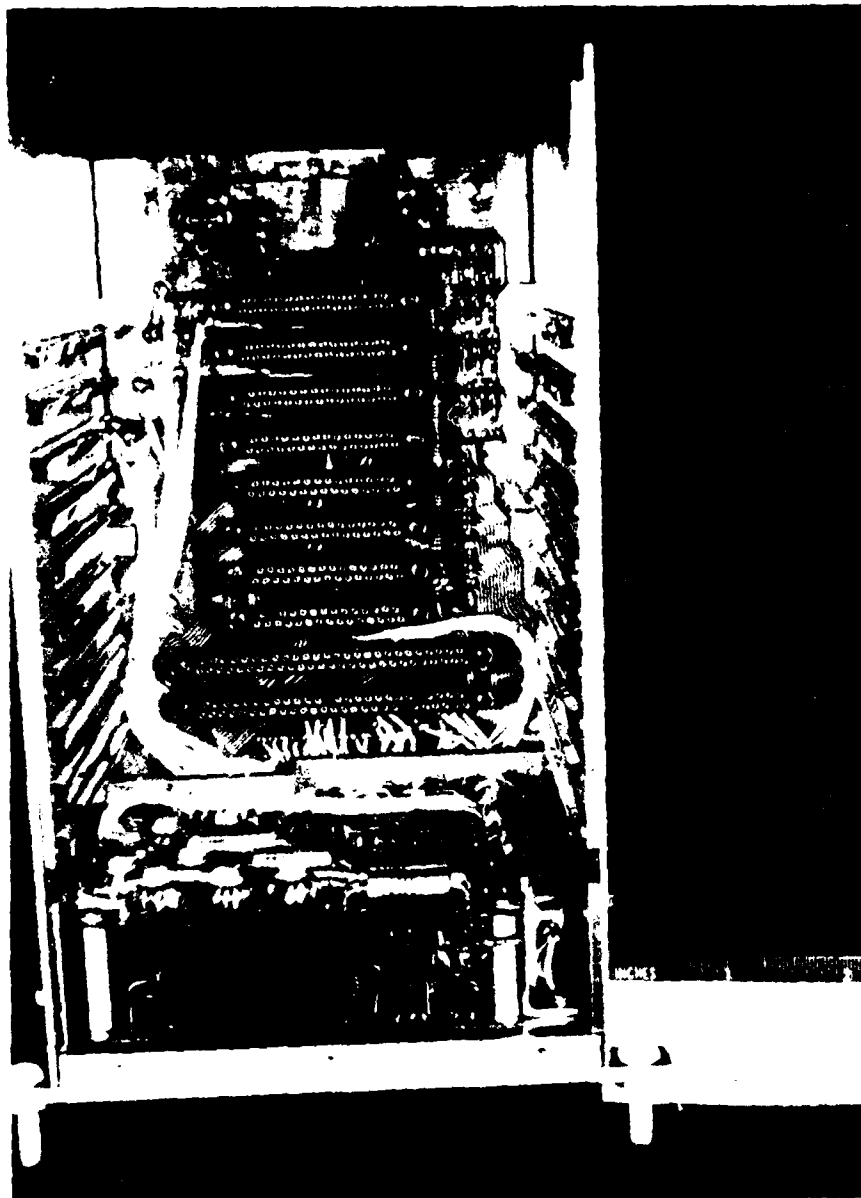


Figure 1.5. Backplane Photo, Inside.

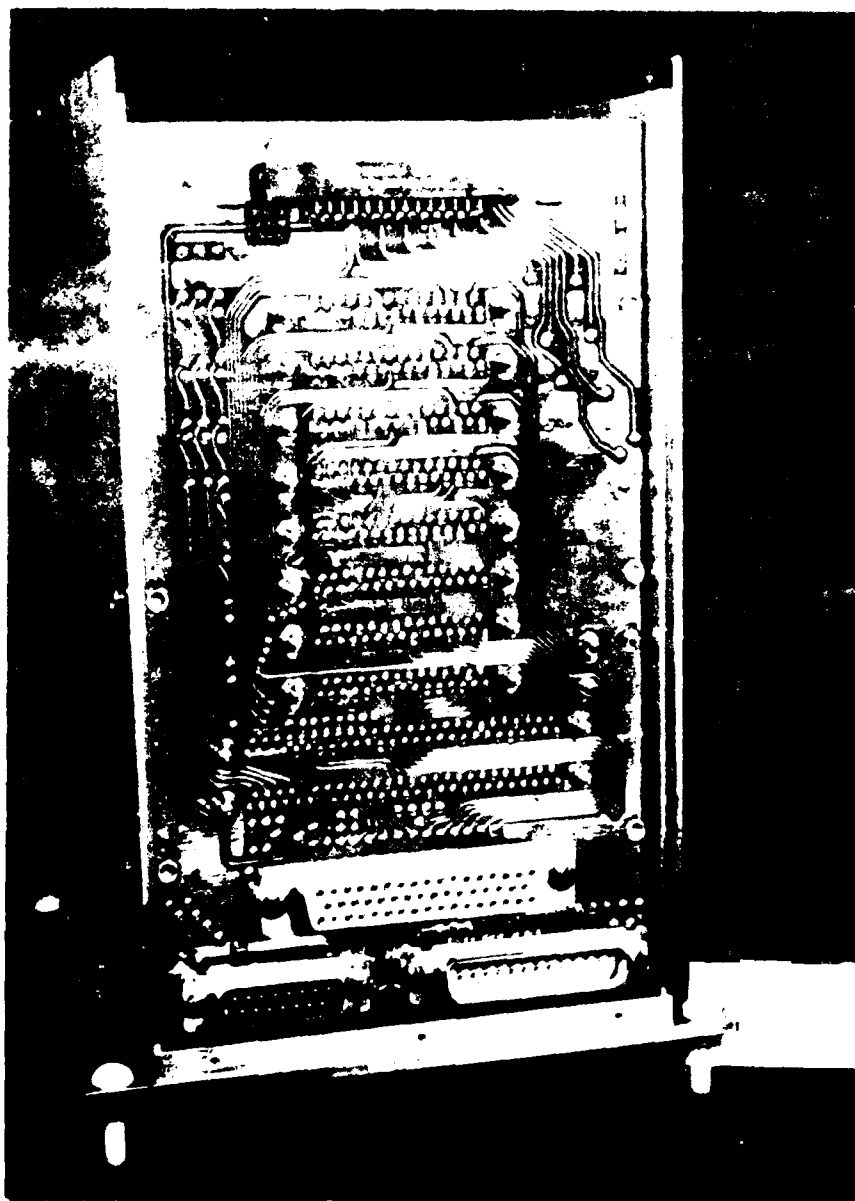


Figure 1.6. Backplane Photo, Outside.

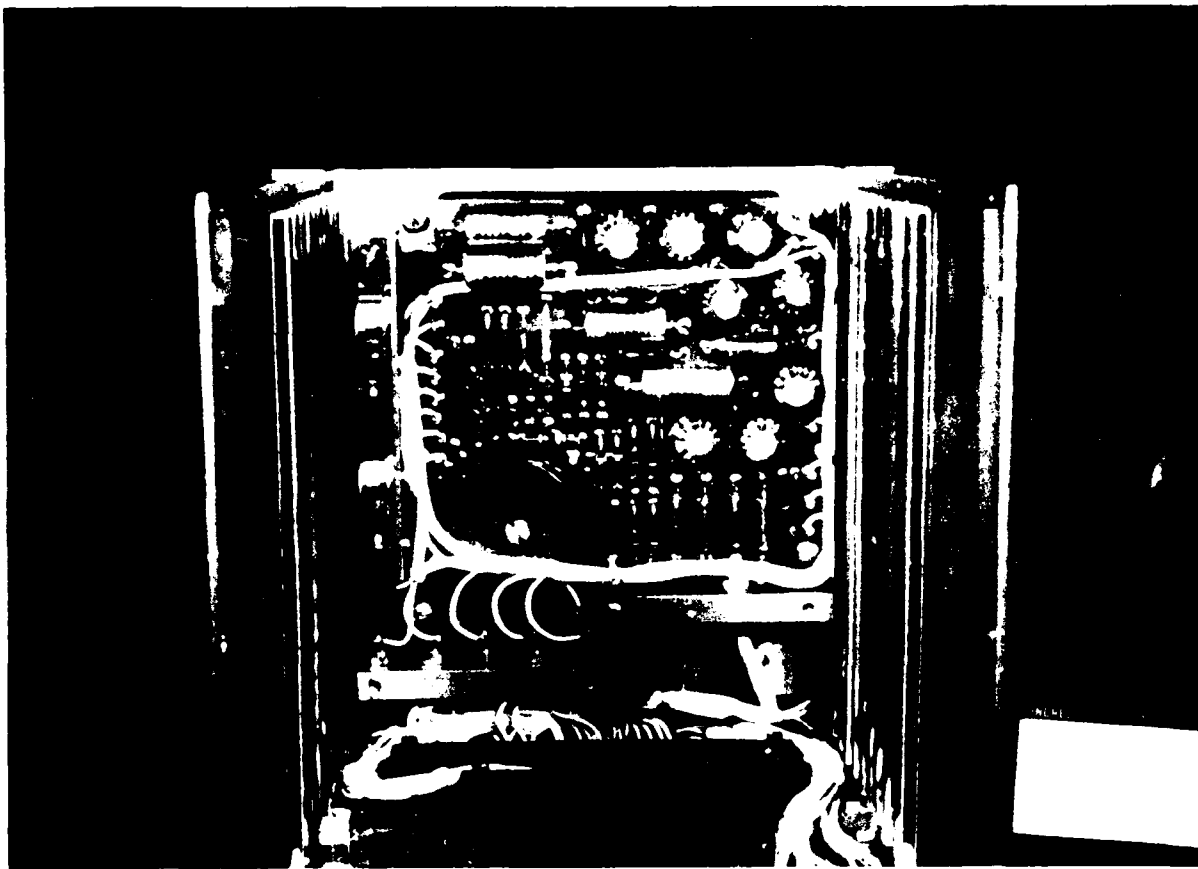


Figure 1.7. DC-DC Converter Photo, Top.

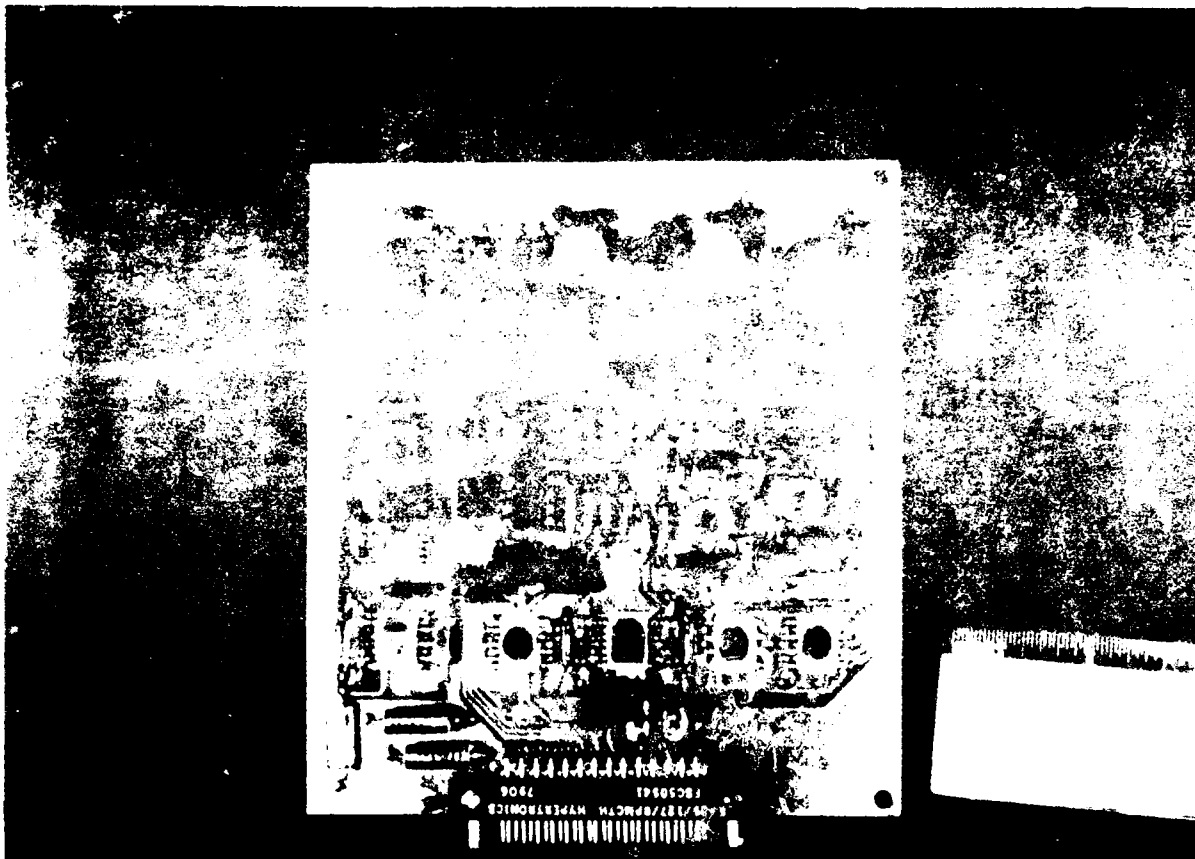


Figure 1.8. Digitizer Board Photo.

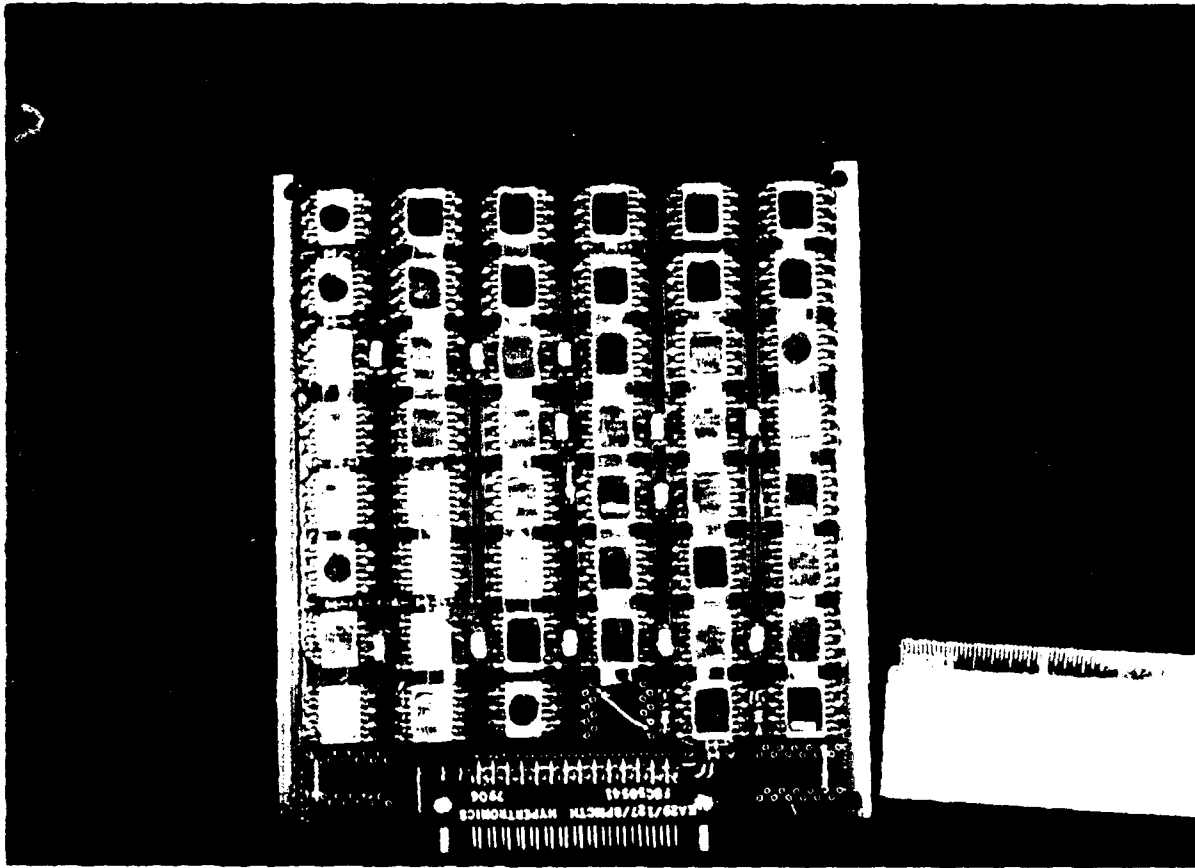


Figure 1.9. Digital Data Board Photo.



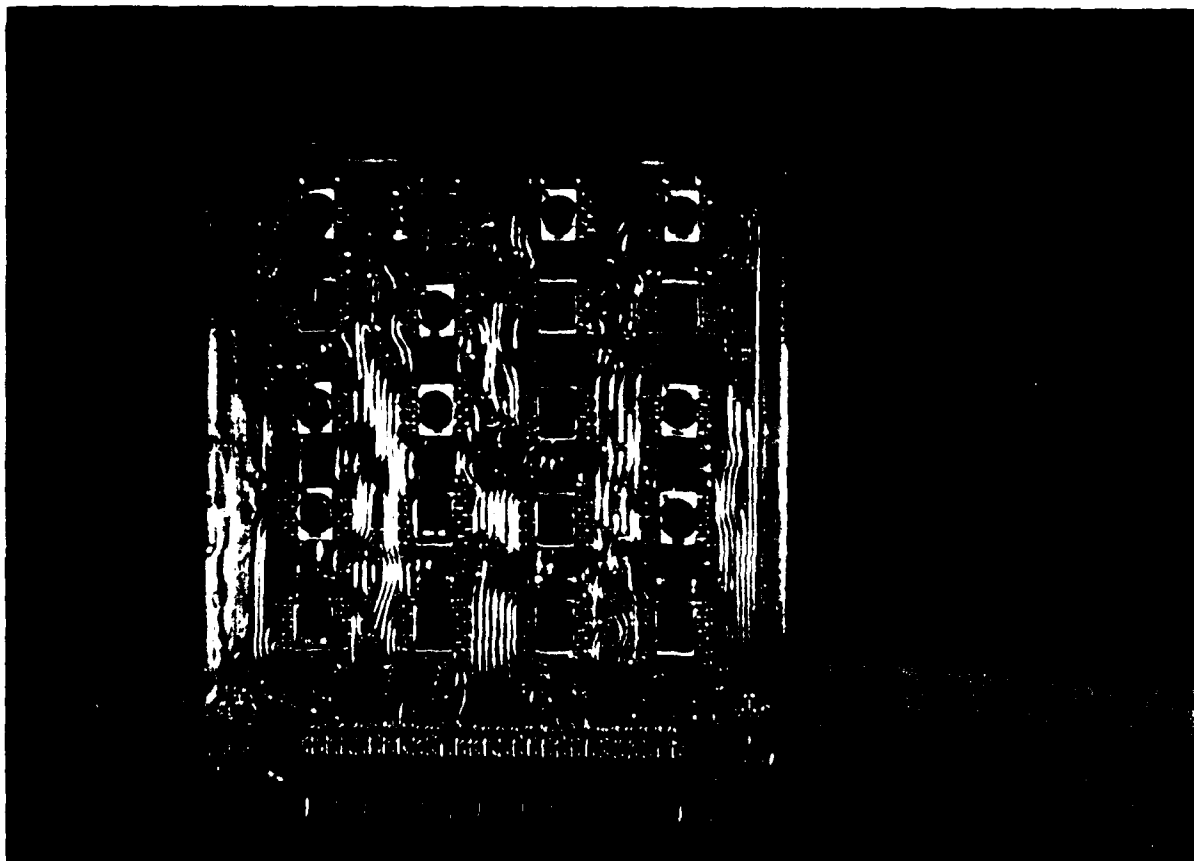


Figure 1.10. Digital Control Board Photo.

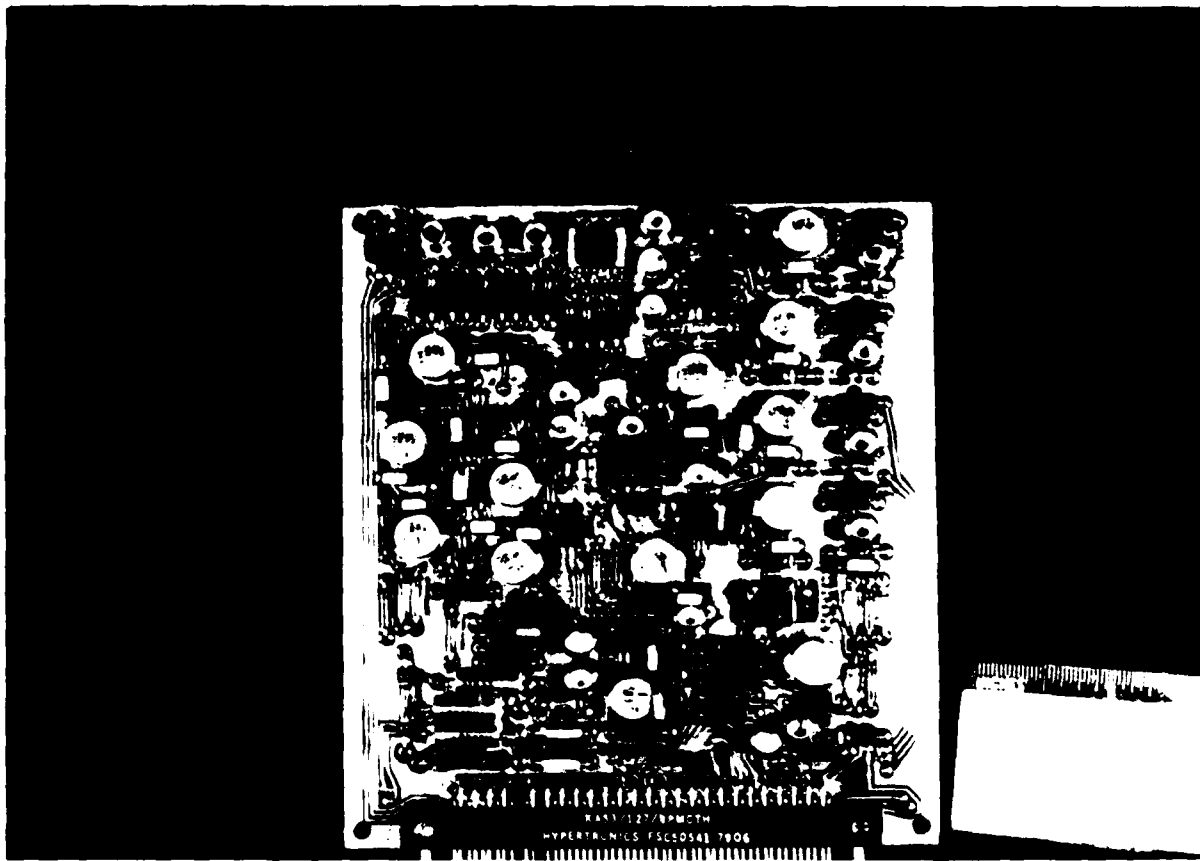


Figure 1.11. Interface/Monitor Board Photo.

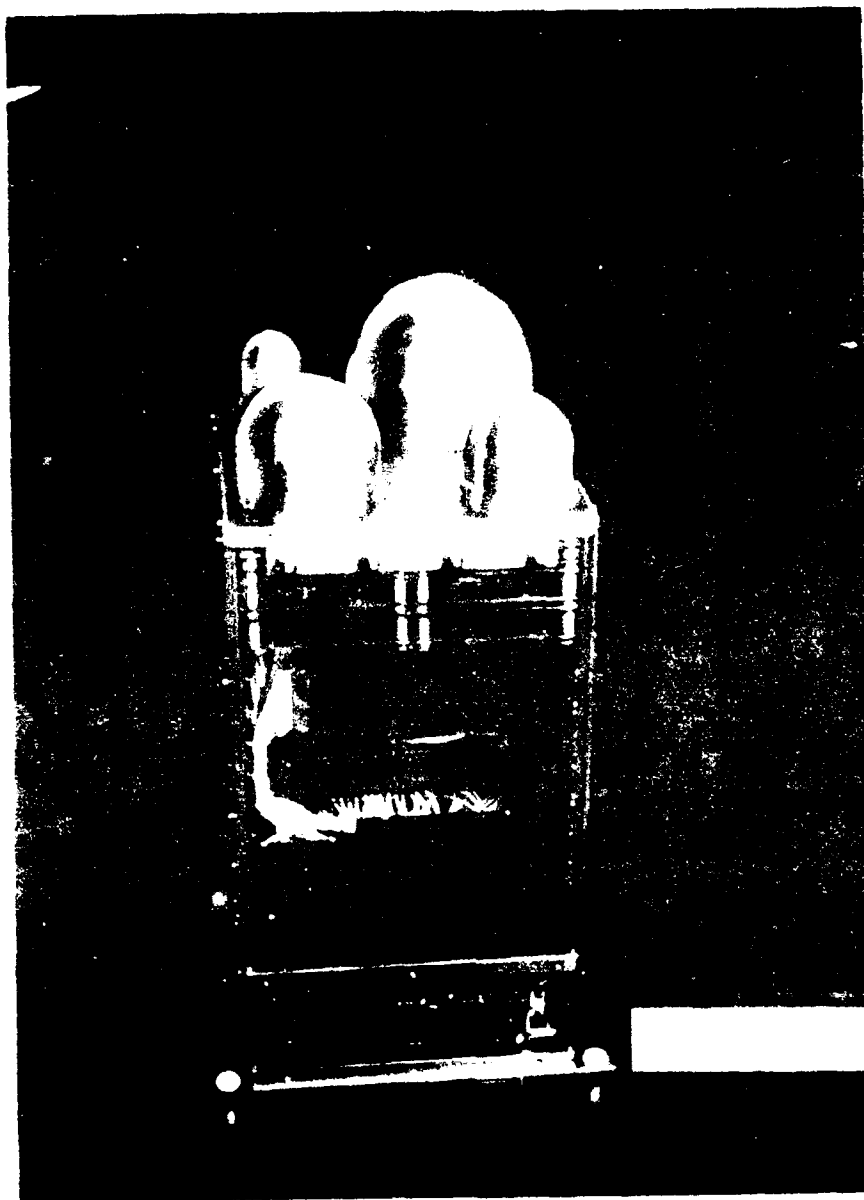


Figure 1.12. Instrument Partial Assembly Photo.

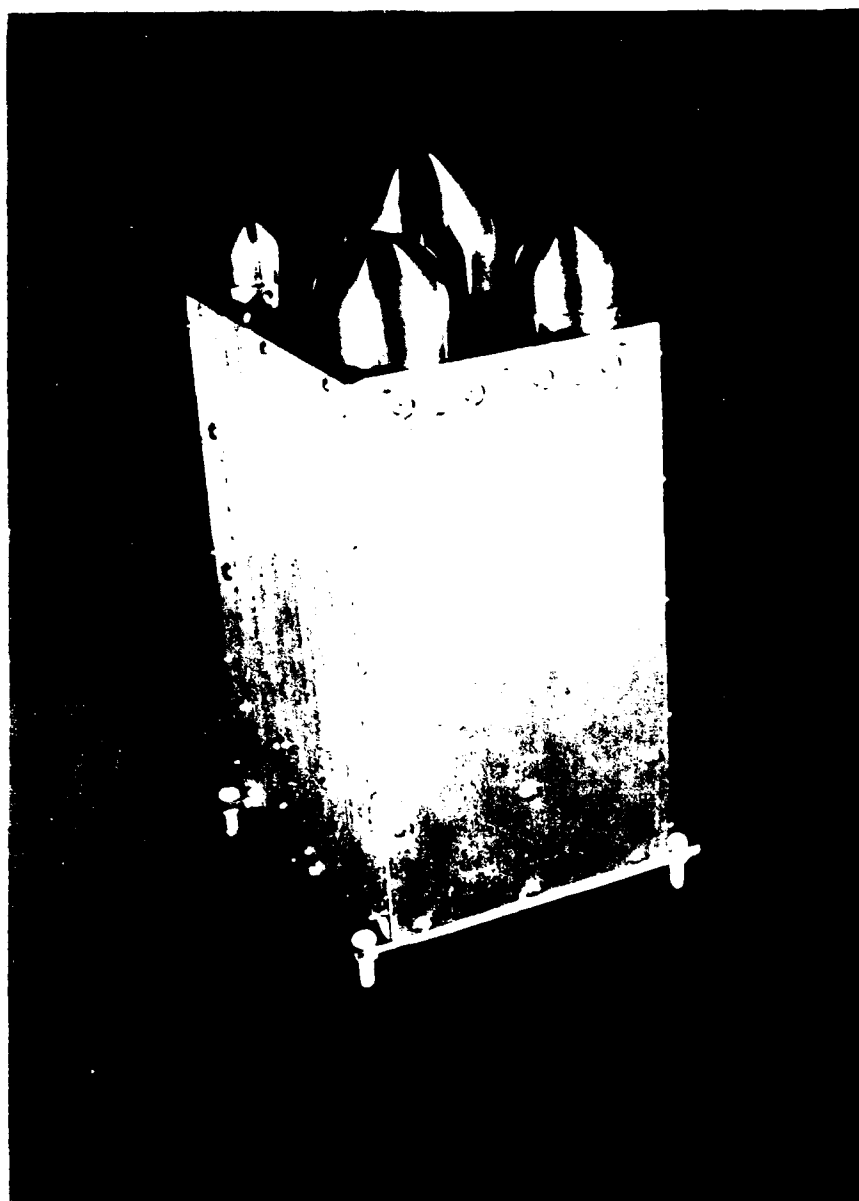


Figure 1.13. Final Unit Photo.

We have just recently completed the R & D Equipment Information Report (Ref 1. 9). The detailed description given here is structured to reflect the PC Board assignment. The test equipment is also described along with operating instructions and final calibration constants.

The present document, although it contains little new material, is a convenient summary for publication of the Dosimeter design, fabrication and test. Section 2 has been adapted from the Design Evaluation Report. A list of the calibration data obtained at the Harvard Cyclotron (energetic protons) and at the AFGL LINAC (energetic electrons) is given in Section 2. 6. Although these data have been reduced sufficiently to indicate proper response, the data reduction necessary to provide the response functions for analysis of orbital results must be carried out in subsequent work. Sections 3, 4 and 5 are identical to Sections 2, 3 and 4 of the Equipment Information Report, except that Section 2. 3 is deleted and a brief reference is substituted as Section 3. 3. Sections 4 and 5 contain the operational description and the summary and conclusions, respectively.

TABLE 1.1 SPECIFICATIONS

Sensors	4 Planar silicon S. S. D. with aluminum shields
Field of View	$2 \pi$ Steradians
Data Fields	3 deposited energy ranges and 2 dose energy ranges per sensor resulting in 5 data fields 1 Electron Dose 1 Electron Flux 1 Proton Dose 1 Proton Flux 1 Nuclear Star Flux
Output Format	36 Bits serial, read out once per second. Each readout is internally multiplexed and must be interpreted in the context of a 64 readout data frame.
Command Requirements	On/Off, Reset, and Calibrate
Size	8" H x 4.5" W x 5.5" D excluding Domes, Connectors, and Mounting Tabs.
Weight	10 lbs
Power	7 W @ 28 VDC
Temperature Range	-10°C to 40°C
Max Accumulated Dose before recycling	$\sim 10^4$ rads (Si) Electrons $\sim 10^3$ rads (Si) Protons
Max Flux before overflow	$\sim 10^6$ Electrons/(cm <sup>2</sup> -sec) above 1 MeV $\sim 10^4$ Protons/(cm <sup>2</sup> -sec) above 20 MeV
Effective Area (For omnidirectional flux)	0.013 cm <sup>2</sup> (Dome 1), 0.25 cm <sup>2</sup> (Dome 2, 3, and 4)

## 2. DESIGN CONSIDERATIONS

### 2.1 Basic

The basic concept of measuring the effects of particles above energy thresholds established by shields has been employed for many years. The environment in which the sensors must operate is fundamental to selection of a particular method of implementing this concept. Hence, in Section 2.2, a short summary of those aspects of the trapped radiation environment necessary for optimizing the design is presented. This includes a general discussion of the trapped radiation environment, as well as the approximately circular 800 km orbit appropriate to the DMSP spacecraft. This is the vehicle on which the first Dosimeter is to be flown. The trapped radiation summary is followed in Section 2.3 by a discussion of the history of these sensors, with a selection of the basic parameters (shield thicknesses and material, detector areas, and geometrical configuration) of the present sensor.

The contract specifies that electron thresholds of 1 and 10 MeV be used for two measurements, with two spaced in between. For purposes of discussing the radiation environment, we provide here a short table giving the hemispherical shield thicknesses (aluminum) and the associated energy thresholds (defined here by the particle energy necessary to have a range equivalent to that thickness; electron range data from Ref. 2.1, proton range data from Ref. 2.2). Also given is the area of the detectors to be used with each sensor which, for simplicity, are called "Domes". For use at different orbits in the trapped radiation environments, the principal possible changes in the Domes themselves would be the detector areas.

Table 2.1

Design Parameters of Dome Sensors

<u>Dome #</u>	<u>Alum. Shield g/cm<sup>2</sup></u>	<u>Detector Area cm<sup>2</sup></u>	<u>Elec. Thres. MeV</u>	<u>Proton Thres. MeV</u>
1	0.55	.051	1.0	~20
2	1.55	1.000	2.5	35
3	3.05	1.000	5.0	51
4	5.91	1.000	10.0	75

The present report is concerned with a method of determining the radiation dose in a semiconductor device due to electron and proton spectra having the energy thresholds given in the table. The basic method of accomplishing this is discussed in Section 2.4. As is seen from the table, we found it necessary to use four domes, and this is also discussed in that section. Section 2.4 also contains the method of calibrating the sensors, by use of the in-flight calibration mode.

Details of the technical approach implemented are discussed in Section 3.

## 2.2 Operational Environment

### 2.2.1 Inner and Outer Zones in General

The earth's trapped radiation is generally characterized as belonging either to the inner or outer zones. Other areas of interest are the polar regions, which are free of trapped radiation, and the geosynchronous orbit region, which is on the outer edge of the outer radiation belt and is very strongly influenced by magnetic storms, as well as by solar flare particles. Radiation damage in the outer zone is principally due to electrons (few tenths to several MeV) and solar protons (several MeV to a few hundred MeV). Trapped protons in this region are very low in energy (up to a few MeV) and are easily shielded. The inner zone is characterized by populations of energetic electrons similar to those in the outer zone (both energy and intensity), while the protons are extremely energetic (tens to hundreds of MeV); the radiation effect is generally greater than that of electrons of similar ranges (at least for ranges greater than roughly one g/cm<sup>2</sup> aluminum).

A recent summary of trapped radiation data is given in Ref. 2.3. Figure 2.1 shows the  $L = 6.6$  (geosynchronous orbit) electron environment measured by a recent satellite (ATS-6) compared to the data base used to derive the AE4 model. At 1 MeV the integral flux is of somewhat greater magnitude than that given in the specifications (Section 1). A detailed calculation of electron dose for the AE4 model has been made by Wilson and Denn (Ref. 2.4); it is reproduced here as Fig. 2.2. For the 0.5 g/cm<sup>2</sup> shield the yearly dose is about  $1.5 \times 10^5$  rad at  $L = 6.6$  - very similar to the  $10^5$  rad requirement here. Shown below are the ratios of the dose expected in the other domes at  $L = 6.6$  compared to that in the 1 MeV dome.

Table 2.2

Approx. Ratio of High Energy Dome Doses to that of Dome #1 for  $L = 6.6$

<u>Dome #</u>	<u>Ratio</u>
1	1
2	.01
3	.002
4	<.001

Clearly, the dose drops very rapidly with increasing threshold. This is also true for other regions of the radiation belts. This is an important consideration, because it indicates that emphasis should be placed on measurement of low doses for the thicker domes, while decreasing the maximum measured dose for the individual domes as necessary to achieve the accuracy at low dose.



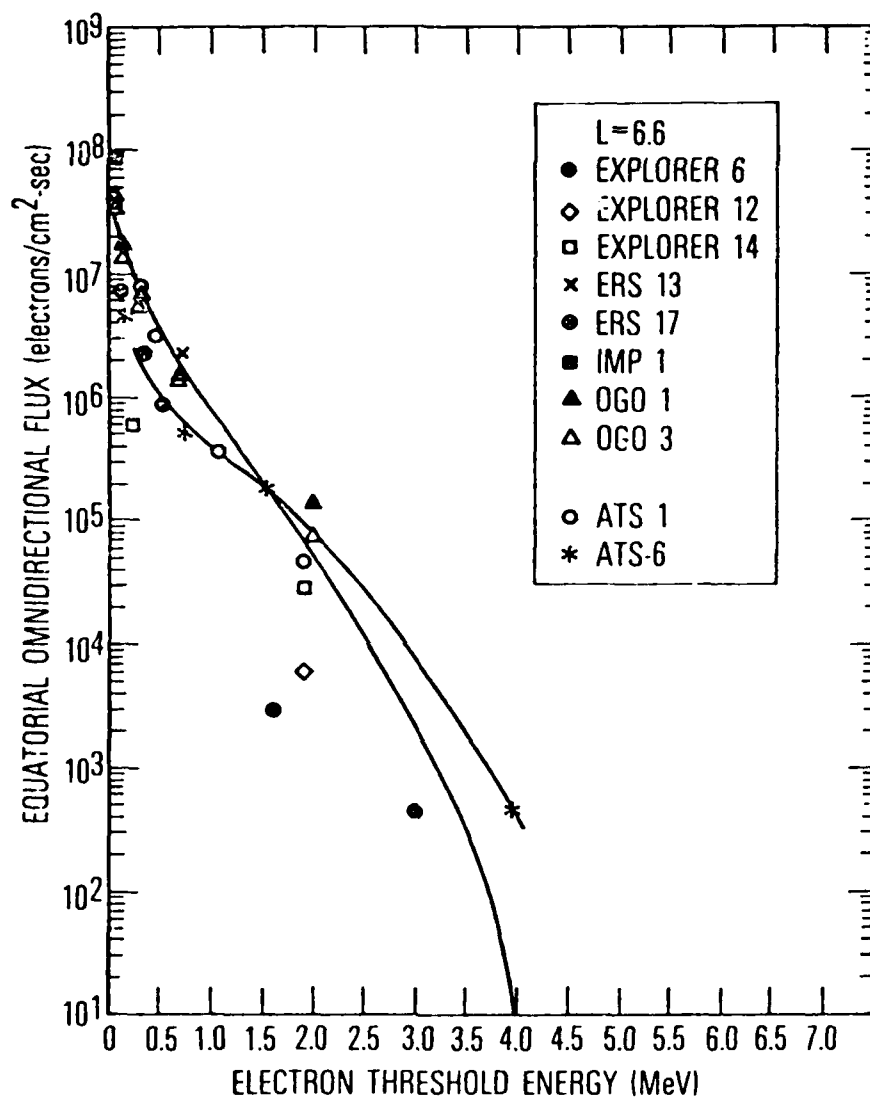


Figure 2.1 Comparison of ATS-6 with AE4 Data Base.  
(Taken directly from Ref. 2.3, Fig. 12)

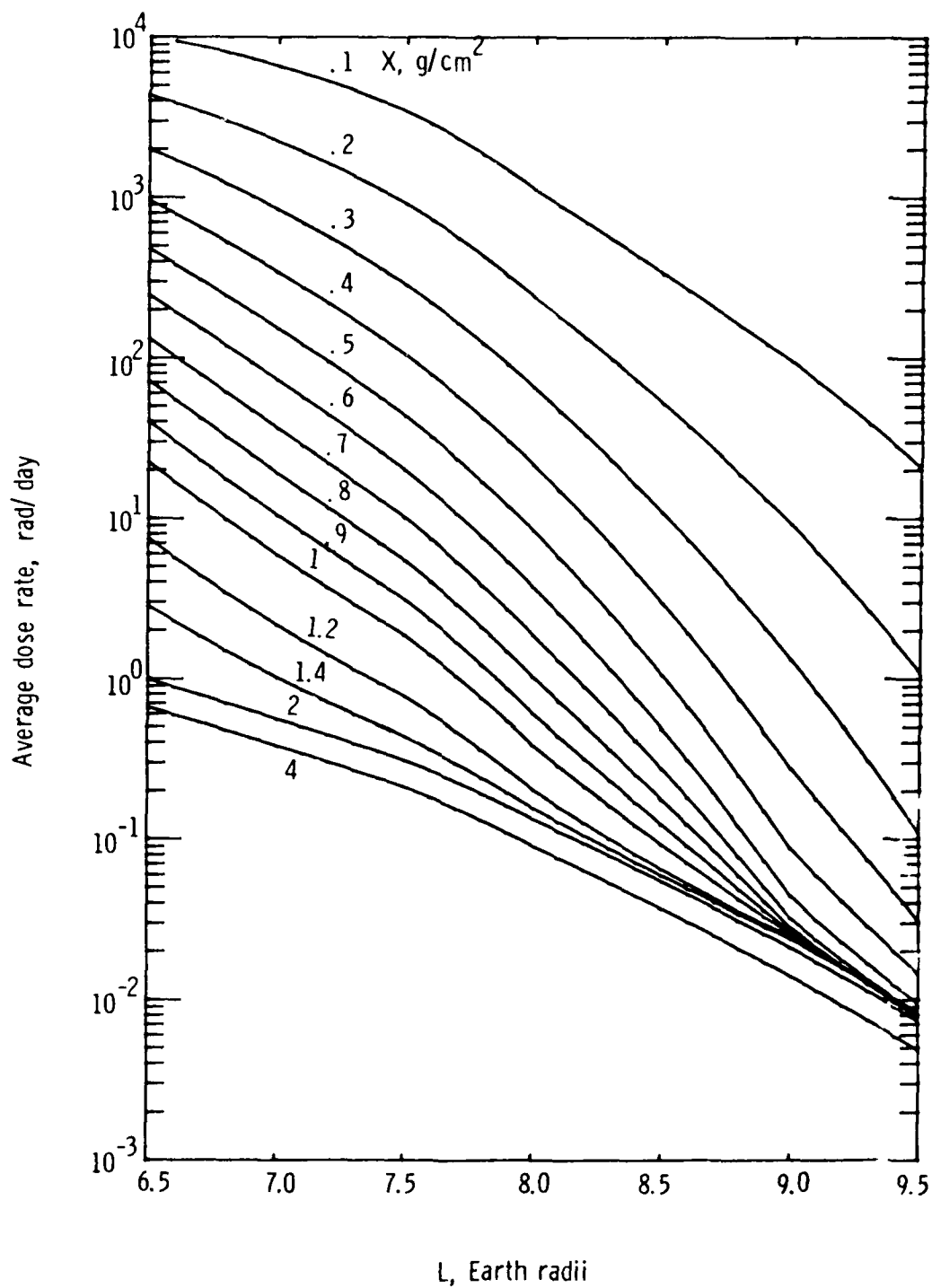


Figure 2.2 Equatorial average dose rate as a function of L-shell behind various aluminum-shield thicknesses.  
(Taken directly from Ref. 2.4, Fig. 8)

Ref. 2.1 also gives data for lower L values; however, the flux units used are not consistent throughout. As a consequence, it is convenient to use a very recent summary (1977) in the Trapped Radiation Handbook (Ref. 2.5) for comparison of inner and outer zone fluxes. Figure 2.3 shows the equatorial profile of  $> 0.5$  MeV electron fluxes for both solar maximum and solar minimum. The fluxes are similar in intensity in both inner and outer zones, with lower intensity in the "slot" ( $L \approx 3$ ). Outer zone fluxes are given in Figure 2.4, also taken from Ref. 2.5. The ratios of the integral fluxes for different thresholds in this figure show that the flux drops rapidly with energy and is generally consistent with the dose ratios in Table 2.2. The flux above 1 MeV is normally about 1/2 that above 0.5 MeV. Hence, it could be in the range  $1$  to  $5 \times 10^6$  e/(cm<sup>2</sup>-sec) maximum throughout the trapped radiation zones. Note, however, that near the

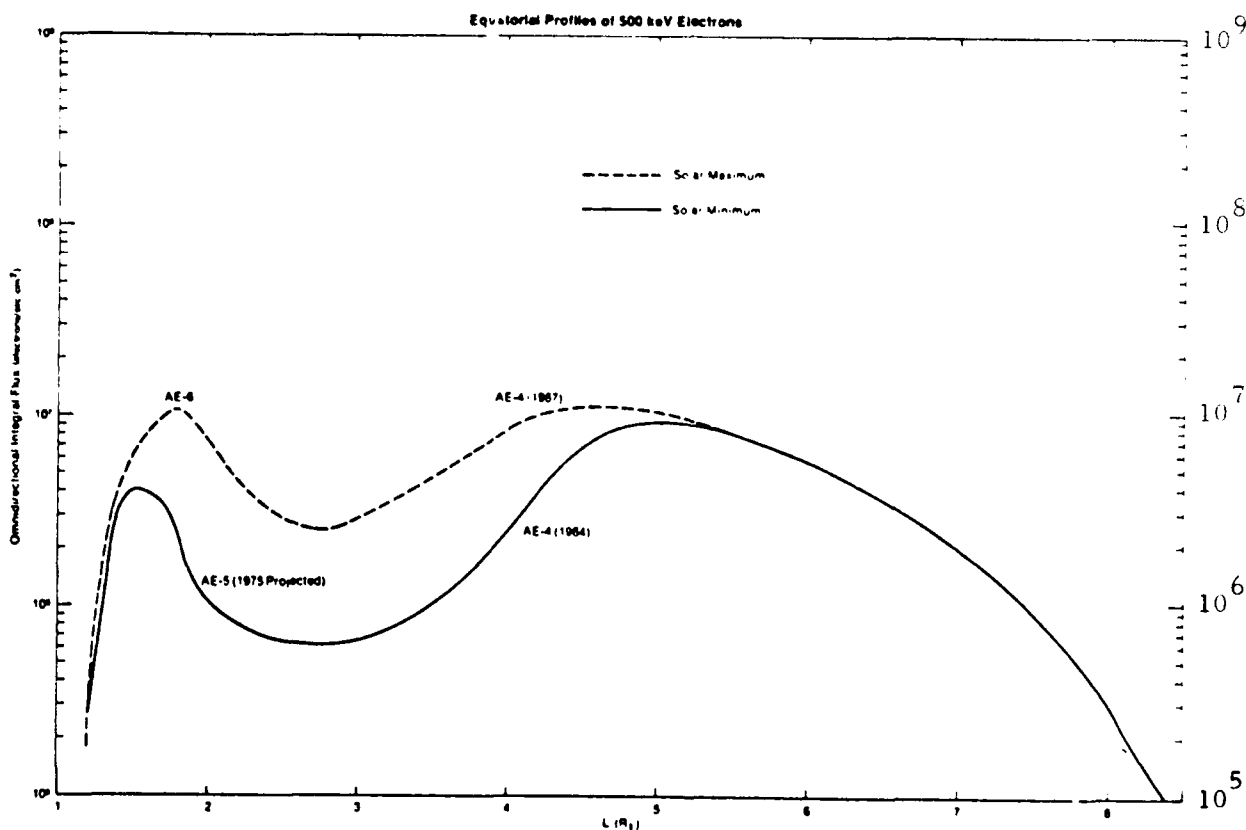


Figure 2.3 Composite equatorial radial profiles of the overall environment models for electrons with  $E > 500$  KeV.

(Taken directly from Ref. 2.5, Fig. 4-56)

inner edge of the inner zone, the gradient is very steep. The fluxes encountered near the 800 km DMSP orbit are much less than those in other parts of the zones. As shown below, the integral flux encountered above 1 MeV near 800 km is consis-

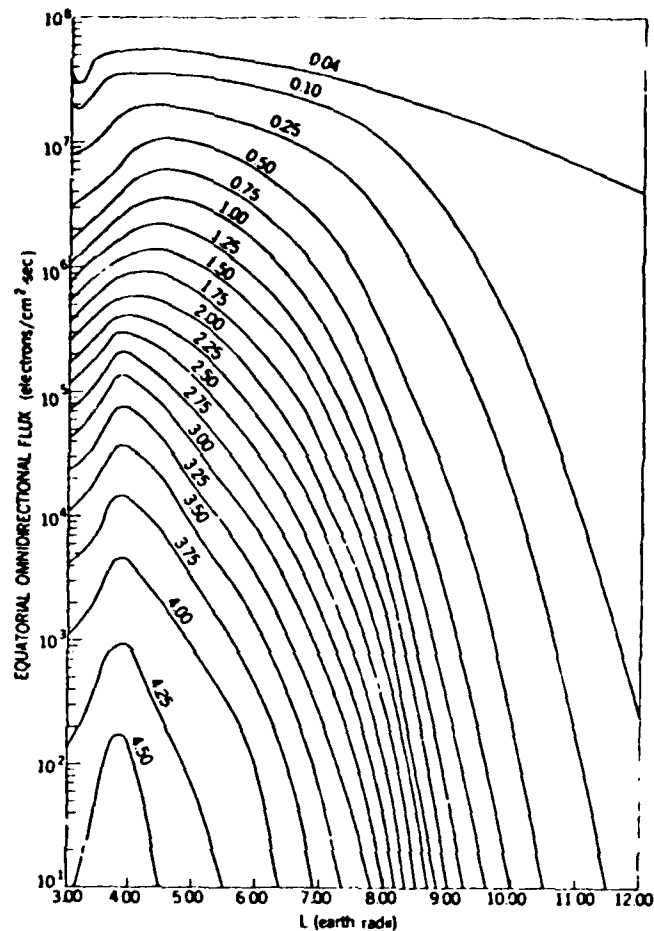


Figure 2.4 AE 4 radial profile of equatorial omnidirectional flux for various energy thresholds, epoch 1967 (taken directly from Ref. 2.5, Fig. 4-46)

tent with a nominal specification of  $10^6 \text{ e}/(\text{cm}^2 - \text{sec})$ .

Figure 2.5 shows the trapped proton fluxes, which makes it clear that these fluxes are only important in the inner zone for any except very thin shields. In estimating the effect of protons it is important to remember that the stopping power for protons in the 20-100 MeV region is from 10 to several times that of electrons; the dose is correspondingly higher for a similar intensity. It is then evident from comparison of Figures 2.4, 2.5 and Table 2.1 that in the inner zone the doses due to electrons and protons will be generally similar in the lowest energy dome, but that due to protons becomes a progressively larger fraction of the total dose as the shield thickness increases.

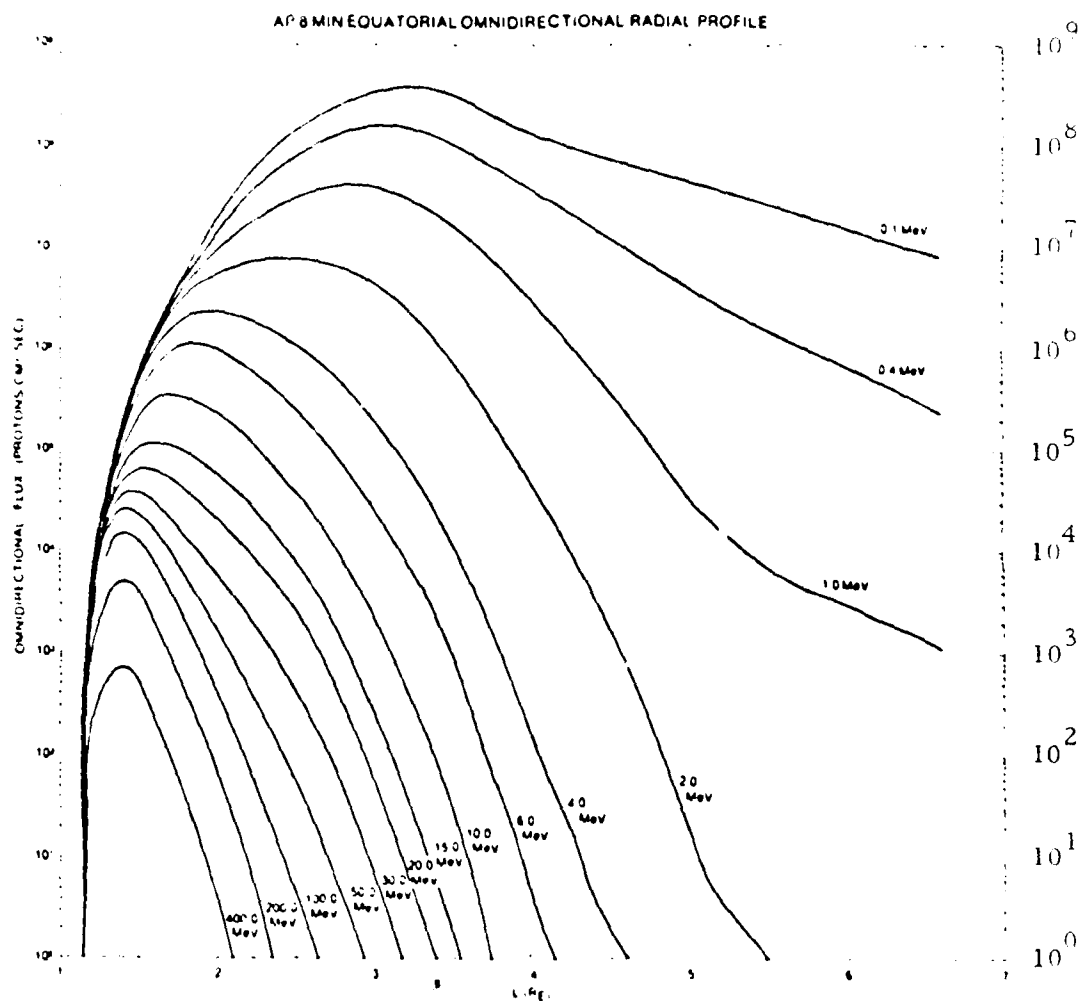


Figure 2.5 Radial distributions of AP8 MIN omnidirectional fluxes of protons in the equatorial plane with energies above threshold values between 0.1 and 400.0 MeV

(taken directly from Ref. 2.5, Fig. 4-8)

Clearly, for any orbit that penetrates the inner zone substantially, most of the dose in the higher energy domes (2-4) will be due to protons. Since the method of detecting the electrons in these sensors cannot discriminate completely against protons, the proton flux is measured simultaneously so that ground contamination in the electron dose measurement can be estimated.

The effect of solar flare protons in the outer zone and over the poles should also be considered. A determination of integral proton fluxes for the last solar cycle has been made by Stassinopoulos and King (Ref. 2.6). Figure 2.6 and Table 2.3 present their results. For a large event such as that of August 1972, the integral flux greater than 30 MeV averages about  $10^4/(\text{cm}^2\text{-sec})$  for several days. While not as large as the maximum  $> 30$  MeV proton flux in the inner zone (Figure 2.5), it would still produce a dose at least comparable to that due to electrons in the outer zone. Thus, similar remarks to those relevant to the inner zone proton effect apply. Inasmuch as we are now near the peak of solar cycle 21, we chose to make the proton measurements-both from the viewpoint of their own damage potential, as well as for correction of the electron channel radiation dose (due to imperfect discrimination against protons).

It is to be expected that the Domes will also respond to nuclear reaction "star" events. Although comparatively rare, their ability to deposit a large energy in a semiconductor commands attention. The instrument will, therefore, count the nuclear star flux as an additional measurement. This same channel will also respond to large energy depositions by very energetic high-Z cosmic rays.

## 2.2.2 DMSP Orbit

The average daily flux in the 835 km DMSP orbit is shown in Figure 2.7. Two-region power law fits have been made to both differential spectra in Figure 2.7 for purposes of obtaining design estimates of the doses and fluxes. For electrons, the breakpoint between the regions is 4.8 MeV; for protons, it is taken as 140 MeV. Results for the integral fluxes are shown in Figure 2.8. The results of Cliff et al. (Ref. 2.17) show the following: for a particular inner zone orbit the bremsstrahlung dose inside a shield greater than about 200-250 mils Al thick will exceed that due to electrons able to penetrate the shield. This is crudely estimated here by the dashed line in Figure 2.8.

The two-region fits were also used to calculate by numerical integration the doses behind spherical shields of various thicknesses, as shown in Table 2.4. These calculations were made by use of fits to stopping power data, which neglects scattering and bremsstrahlung effects. For protons, neither effect is important. For electrons, both are significant; although for design purposes, only the bremsstrahlung effect must be included.

Results for both the estimated integral fluxes and doses for the chosen hemispherical thicknesses are shown in Table 2.5. These were used for

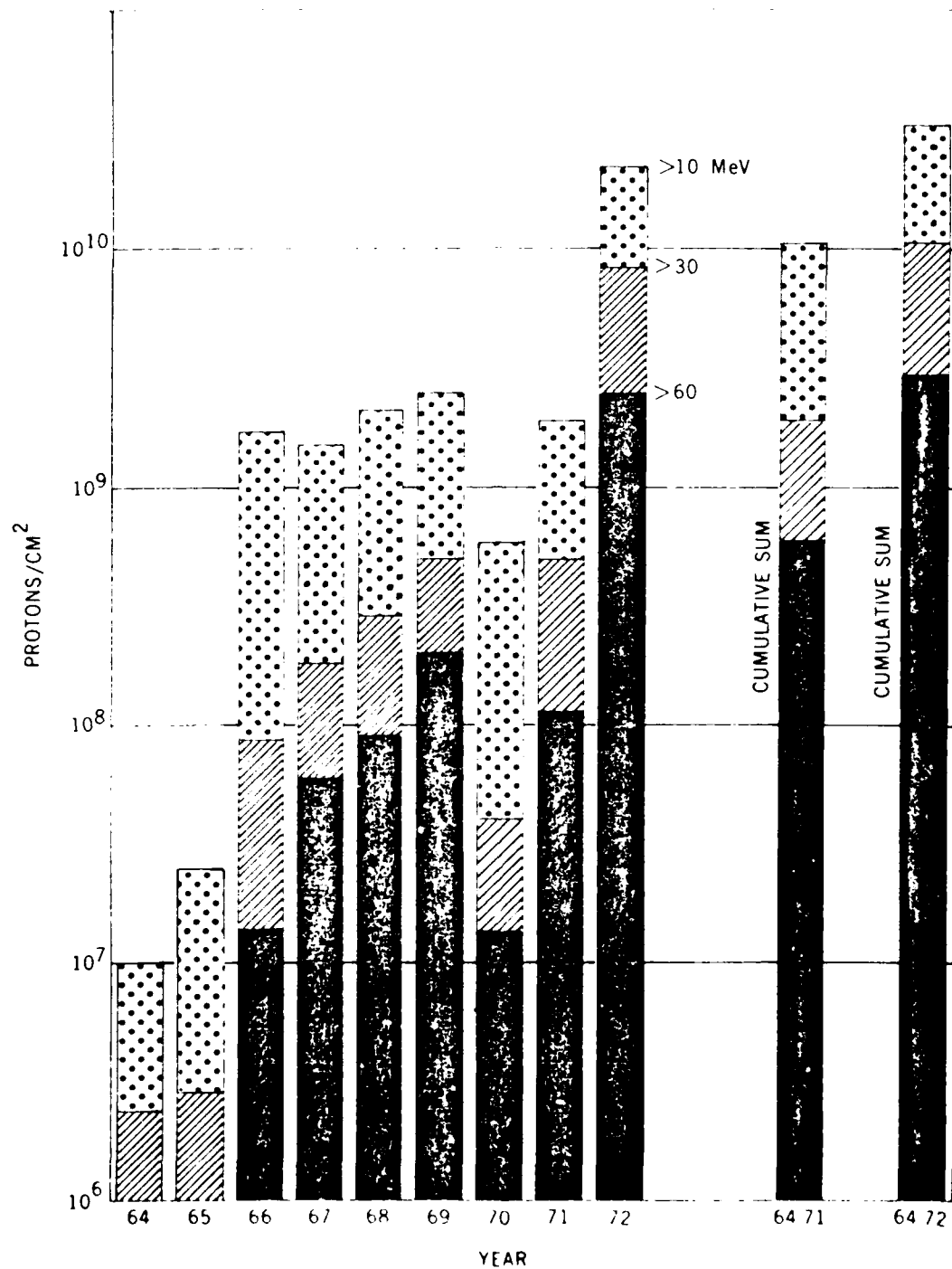


Figure 2.6 - Annual and Cumulative Solar Cycle 20 Proton Fluxes  
(taken directly from Ref. 2.6, Fig. 1)

Table 2.3 PEAK AND INTEGRATED PROTON FLUXES FOR LARGE SOLAR EVENTS MAY 1967 - AUGUST 1972

TIME PERIOD	$J_{pk}(>10 \text{ MeV})$ ( $\text{cm}^2\text{-ster-sec})^{-1}$	$J_i(>10 \text{ MeV})$ ( $\text{cm}^2\text{-ster})^{-1}$	$J_{pk}(>30 \text{ MeV})$ ( $\text{cm}^2\text{-ster-sec})^{-1}$	$J_i(>30 \text{ MeV})$ ( $\text{cm}^2\text{-ster})^{-1}$	$J_{pk}(>60 \text{ MeV})$ ( $\text{cm}^2\text{-ster-sec})^{-1}$	$J_i(>60 \text{ MeV})$ ( $\text{cm}^2\text{-ster})^{-1}$
May 25-26, 1967	1015	$4.6 \times 10^7$	32	$1.7 \times 10^6$	2.3	$2.5 \times 10^4$
May 28-30, 1967	115	$7.1 \times 10^6$	27	$1.3 \times 10^6$	9.4	$4.3 \times 10^5$
Dec. 3-6, 1967	31.5	$2.2 \times 10^6$	10.5	$4.6 \times 10^5$	3.8	$2.5 \times 10^5$
Jun. 9-11, 1968	354	$3.3 \times 10^7$	12.4	$8.9 \times 10^5$	5.4	$9.0 \times 10^4$
Sep. 28 (hr 12) -						
Oct. 2, 1968	32	$3.3 \times 10^6$	19	$6.9 \times 10^5$	10.3	$3.4 \times 10^5$
Oct. 4-6, 1968	36	$3.6 \times 10^6$	6.3	$2.6 \times 10^5$	1.1	$5.0 \times 10^4$
Oct. 31 - Nov. 3, 1968	133 (10/31)	$2.1 \times 10^7$	10.0 (10/31)	$1.2 \times 10^6$	1.4 (10/31)	$2.0 \times 10^5$
	152 (11/2)		11.7 (11/1)		1.1 (11/1)	
Nov. 18-21, 1968	849	$9.0 \times 10^7$	404	$1.7 \times 10^7$	96.0	$6.2 \times 10^6$
Dec. 4-9, 1968	152	$2.2 \times 10^7$	31	$3.2 \times 10^6$	5.2	$5.6 \times 10^5$
Feb. 25 - Mar. 1, 1969	88 (2/25)	$5.0 \times 10^6$	41.5 (2/25)	$2.1 \times 10^6$	24.3 (2/25)	$1.3 \times 10^6$
	28 (2/27)		9.3 (2/27)		3.7 (2/27)	
Mar. 30 - Apr. 10, 1969	26	$3.5 \times 10^6$	13	$1.3 \times 10^6$	8.7	$8.1 \times 10^5$
Apr. 12-17, 1969	1375	$1.2 \times 10^8$	123	$1.6 \times 10^7$	16.0	$4.6 \times 10^6$
Nov. 2-6, 1969	1317	$6.9 \times 10^7$	737	$2.1 \times 10^7$	201.0	$9.6 \times 10^6$
Jan. 31 - Feb. 2, 1970	24.2	$2.2 \times 10^6$	6.2	$2.7 \times 10^5$	1.8	$7.3 \times 10^4$
Mar. 6-9, 1970	93	$8.0 \times 10^6$	0.9	$1.0 \times 10^5$	(NO INCREASE)	$6.2 \times 10^3$
Mar. 29-31, 1970	66	$4.7 \times 10^6$	20.2	$1.7 \times 10^6$	6.5	$9.3 \times 10^5$
Jul. 23-25, 1970	206	$6.5 \times 10^6$	0.8	$5.8 \times 10^4$	(NO INCREASE)	$2.9 \times 10^3$
Aug. 14-17, 1970	183	$2.1 \times 10^7$	2.7	$3.9 \times 10^5$	0.3	$3.2 \times 10^4$
Nov. 5-8, 1970	42	$7.7 \times 10^6$	1.7	$2.8 \times 10^5$	0.4	$3.5 \times 10^4$
Jan. 24-29, 1971	1171	$1.2 \times 10^8$	408	$2.7 \times 10^7$	89.4	$4.7 \times 10^6$
Apr. 6-8, 1971	51	$2.3 \times 10^6$	5.0	$2.0 \times 10^5$	1.1	$2.7 \times 10^4$
Sep. 1-5, 1971	352	$3.0 \times 10^7$	162	$1.3 \times 10^7$	66.5	$4.4 \times 10^6$
May 28 - June 1, 1972	39	$5.5 \times 10^6$	2.7	$5.3 \times 10^5$	1.2	$1.2 \times 10^5$
Aug. 4-7 (hr 12), 1972	86000	$1.64 \times 10^9$	21000	$6.2 \times 10^8$	6400	$1.9 \times 10^8$
Aug. 7 (hr 12)-9, 1972	35000	$1.9 \times 10^8$	384	$3.0 \times 10^7$	70	$4.7 \times 10^6$

(taken directly from Ref. 2.6, Table B)



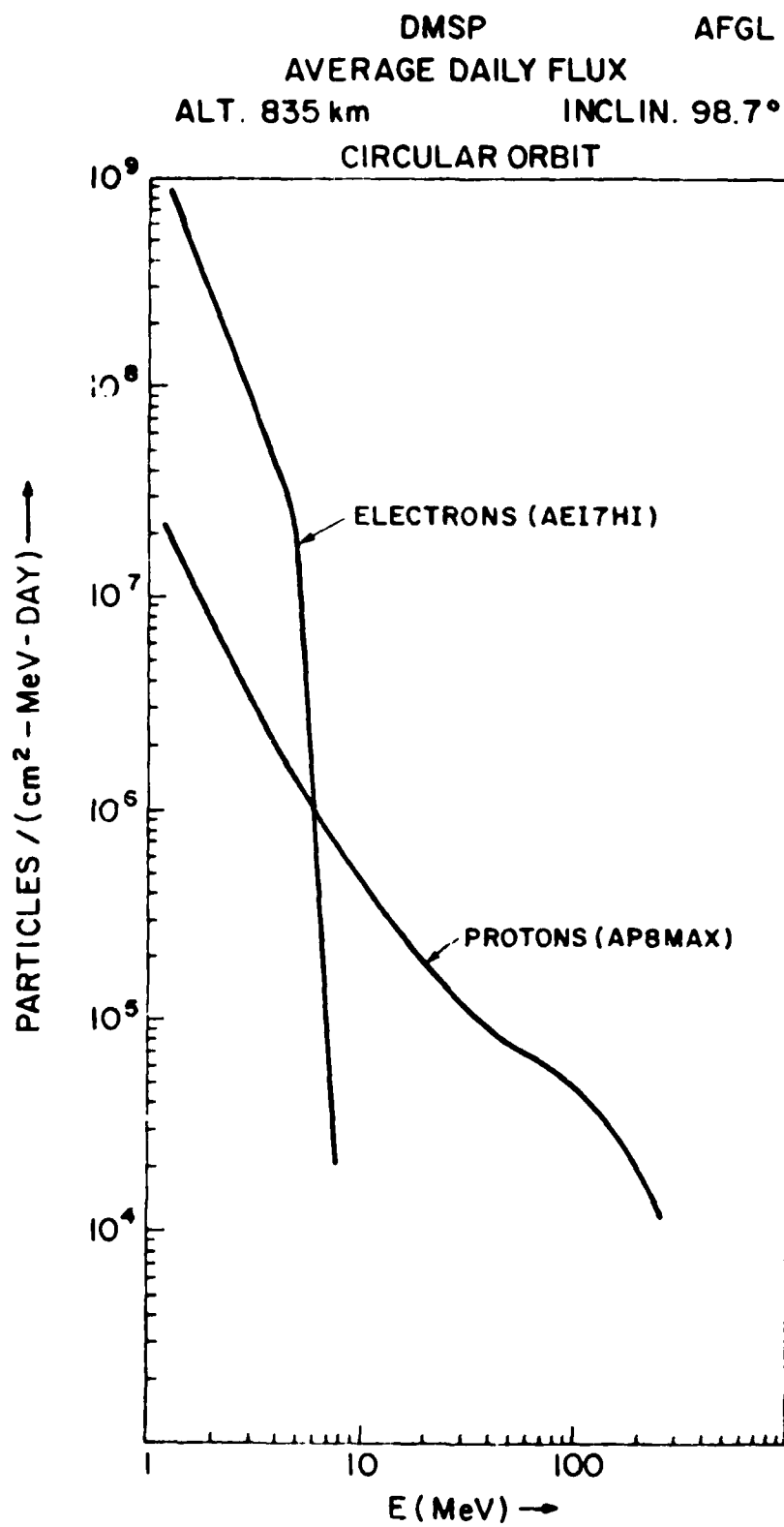


Figure 2.7 Dosimeter Nominal Design Spectra

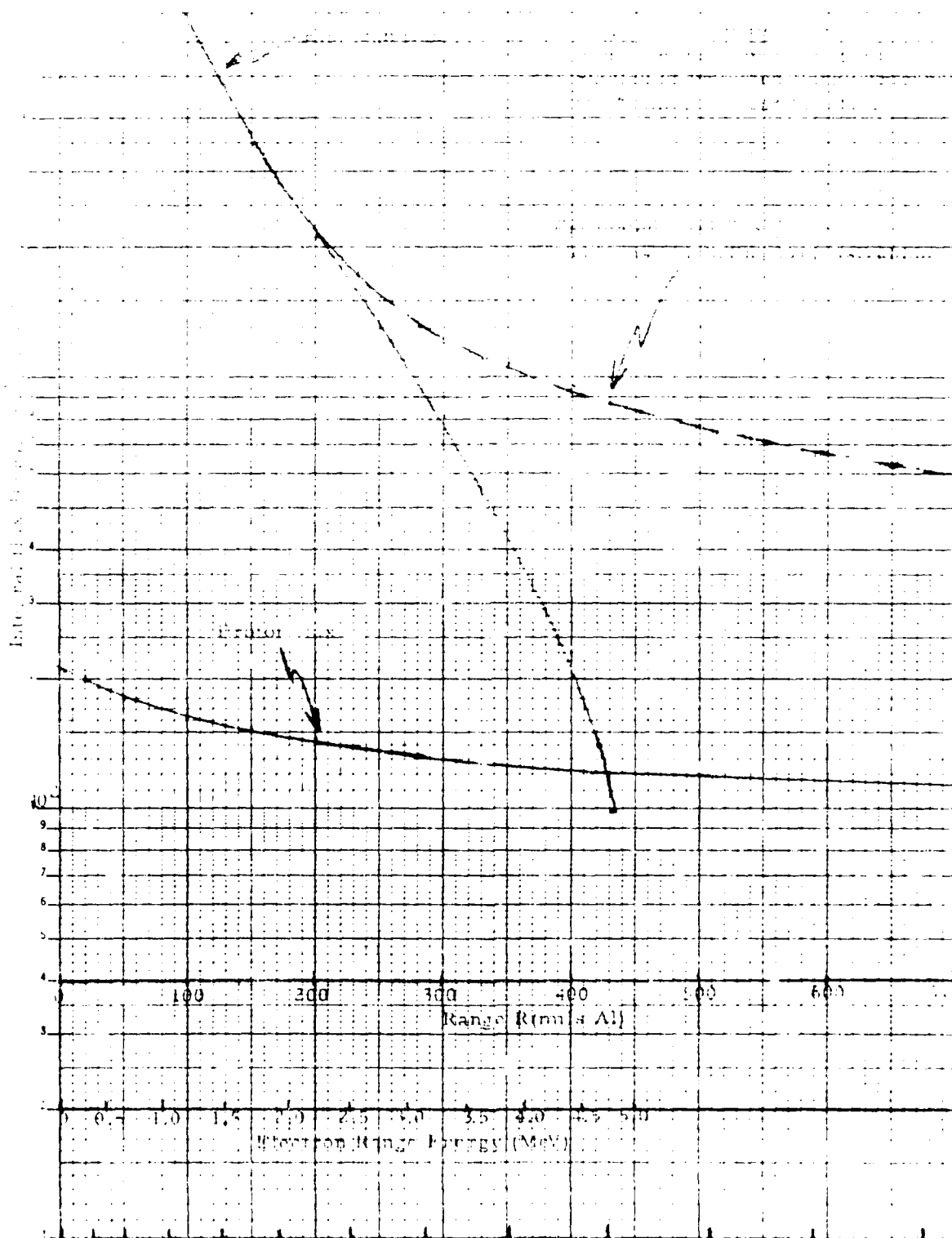


Table 2.4 Estimated Doses Behind Aluminum Spherical Shields is Indicated Thickness for Nominal Design Spectra.

DOSE (RAD/YR) VS SHIELD THICKNESS IN MILS				
T MILS	DL R/YR	DH R/YR	D R/YR	
50.	15953.7	57.6	16011.3	DL = low energy region dose, 1-4.8 MeV
100.	5411.8	58.9	5470.7	
150.	2700.8	60.4	2761.2	DH = high energy region dose, >4.8 MeV
200.	1553.1	62.2	1615.3	
250.	949.5	64.2	1013.7	D = DL + DH
300.	591.7	66.6	658.3	
350.	363.9	69.5	433.4	
400.	212.6	73.3	285.9	
450.	110.6	78.6	189.2	
500.	43.0	87.0	130.0	

#### ELECTRONS (not including Bremsstrahlung)

DOSE (RAD/YR) VS SHIELD THICKNESS IN MILS				
T MILS	DL R/YR	DH R/YR	D R/YR	
50.	820.8	84.4	905.2	DL = low energy region dose, 10-140 MeV
100.	564.6	84.8	649.4	
150.	443.8	85.1	528.9	DH = high energy region dose, >140 MeV
200.	368.9	85.5	454.3	
250.	316.3	85.8	402.1	D = DL + DH
300.	276.7	86.2	362.8	
350.	245.3	86.6	331.9	
400.	219.7	86.9	306.6	
450.	198.2	87.3	285.5	
500.	179.8	87.7	267.5	
550.	163.8	88.1	252.0	
600.	149.8	88.5	238.4	
650.	137.4	88.9	226.4	
700.	126.3	89.4	215.7	
750.	116.3	89.8	206.1	
800.	107.2	90.3	197.4	
850.	98.9	90.7	189.6	
900.	91.3	91.2	182.5	
950.	84.3	91.7	176.0	
1000.	77.8	92.2	170.0	

#### PROTONS

design purposes with a reasonable safety factor. The magnitude of safety factor required is shown by the peak fluxes expected in the DMSP orbit (from Ref. 1.4) due to the South Atlantic Anomaly (SAA), Table 2.6. If these are interpreted as integral fluxes above the energy E, then they generally exceed the nominal design fluxes, Figure 2.7, by a factor of 10-20. Thus, for short periods of time, such fluxes must be handled by the Dosimeter.

Table 2.5 Estimated Doses and Fluxes Behind Chosen Aluminum Hemispherical Shields for Nominal Design Spectra.

T MILS	Electrons			Protons		
	Range E MeV	Int. Flux (cm <sup>2</sup> -sec) <sup>-1</sup>	Dose Rad/Yr	Range E MeV	Int. Flux (cm <sup>2</sup> -sec) <sup>-1</sup>	Dose Rad/Yr
81	1.0	9000	5000	~20	170	375
227	2.5	1800	800	35	140	215
447	5.0	850	375	51	120	145
865	10.0	450	450	75	110	90

Notes for Table 2.5:

These values were used for design purposes only. Electron estimates do not take into account scattering, but do include estimates of bremsstrahlung effects. Fluxes are from Figure 2.7, with extrapolation for T = 865 mils. Doses are interpolated from Table 2.4, (hemispherical dose is taken as half of the spherical dose) with estimated additions due to electron bremsstrahlung dose found by assuming that dose to be proportional to the total flux due to electrons in Fig. 2.7, normalized at 2.5 MeV.

An instrument basically similar in concept to the present one was flown on DMSP (F-1), launched in June, 1977 - somewhat before the solar cycle peak (Pruett), Ref. 2.21). It did not separate electrons and protons and did not measure stars or fluxes. It employed four hemispherical aluminum shields: 35, 75, 125 and 200 mils in thickness. This compares with the present values given in Table 2.5, which cover a much larger thickness range. The 200 mil electronics did not operate properly on F-1, so dose data were provided only for 35, 75 and 125 mils (see their Fig. 5). Their measurements were roughly a factor of two below their calculations (their Fig. 2, made by use of TIGER code), which are also about a factor of two less than those made for the present design by more approximate methods (results in Table 2.8 below). Pruett concludes that it would be wise to design spacecraft utilizing the higher limits given by their calculations, particularly for measurements near solar maximum. We believe the upper dose limits (Table 2.8) to fill the various counters (after which they recycle) are consistent with that approach and represent prudent design choices.

### 2.2.3 Brief Summary

- 1) The electron induced dose for the lowest energy dome (1 MeV) should not exceed  $10^6$  rads in a year anywhere in the radiation belts. The maximum integral flux should be less than  $2 \times 10^7$  e/(cm<sup>2</sup> - sec).
- 2) For the nominal DMSP orbit, the induced dose in the lowest energy dome should be near  $10^4$  rad/year, with integral fluxes near  $10^4$  e/(cm<sup>2</sup>-sec). However, the effects of the SAA increase the flux by a factor of 10-20; therefore, fluxes near  $2 \times 10^5$  e/(cm<sup>2</sup> - sec) must be handled on short-term basis.

- 3) Doses for the higher energy domes will be significantly less than that of the lowest (Table 2.2), and this is taken into account in the design.
- 4) Effects of solar flare protons (outer zone and over poles) are significant, while those of inner zone protons are even larger. These will be measured for determination of their contribution (which cannot be totally eliminated) to the electron dose channel, and for special characterization of their inherent damage potential.

TABLE 2.6a PEAK FLUXES

ELECTRONS

<u>PARTICLE ENERGY (E) (MeV)</u>	<u>PEAK FLUX (E) PER CM<sup>2</sup>/SEC</u>
0.05	$1.1 \times 10^7$
0.50	$3.7 \times 10^5$
1.00	$1.8 \times 10^5$
2.00	$5.7 \times 10^4$
3.00	$2.3 \times 10^4$
4.00	$1.0 \times 10^4$
5.00	$3.0 \times 10^3$

TABLE 2.6b PEAK FLUXES

PROTONS

<u>PARTICLE ENERGY (E) (MeV)</u>	<u>PEAK FLUX (E) PER CM<sup>2</sup>/SEC</u>
$10^{-4}$	$1.1 \times 10^6$
0.10	$5.2 \times 10^5$
2.00	$1.8 \times 10^4$
5.00	$7.8 \times 10^3$
10	$7.2 \times 10^3$
20	$6.2 \times 10^3$
30	$5.5 \times 10^3$
50	$4.4 \times 10^3$
100	$2.5 \times 10^3$

Table 2.6 "Peak" Fluxes in DMSP Orbit, Due to South Atlantic Anomaly  
(Taken directly from Ref. 1.4, Tables 4.3.7.1 and 4.3.7.2)

- 5) Nuclear star events will not be ignored.
- 6) For versatility, the design allows use of the Dome sensors in different orbits simply by changing the detector areas used.

### 2.3 Dome Design

The concept of using a hemispherical metal shield to define an energy threshold for a satellite-borne electron and proton sensor goes back to at least 1963 (Ref. 2.7, Fig. 6). Since then various implementations of this concept have been carried out - principally with the objective of making integral flux measurements (Refs. 2.8-2.15). However, in at least two instances the objective was measurement of dose (Ref. 2.16, 2.21) due to all types of radiation, with no flux measurements.

The basic concept is shown below:

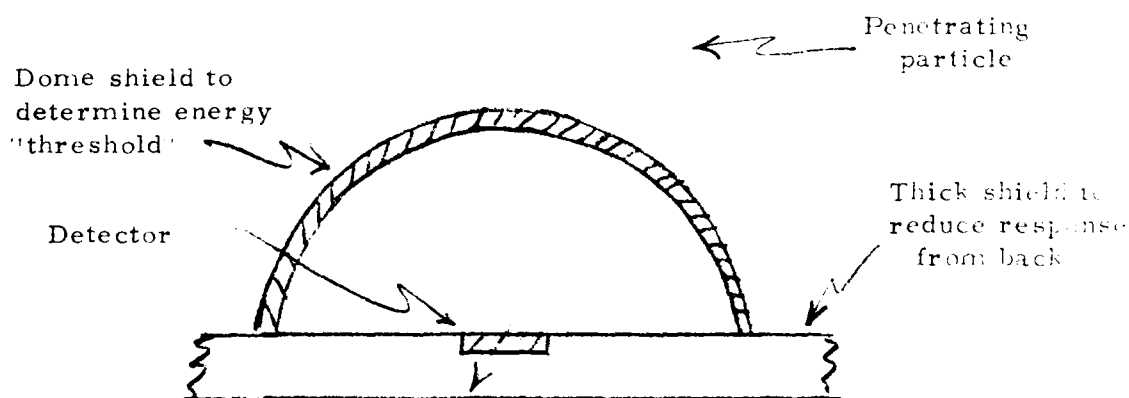


Figure 2.9 Dome Sensor Concept

Essentially, the thickness of the dome determines an energy spectrum threshold, which depends on the type particle and, to some extent, the spectrum shape. Methods of determining the energy threshold spectrum dependence are discussed in Refs. 2.7, 2.8, and 2.11. The spectrum threshold also depends, to some extent, on the energy deposition threshold set in the detector (the energy that must be deposited in the detector in order for a count to be recorded.) The detector may be either of the "planar" type (detection area dimensions large compared to thickness - for example, a thin cylindrical section), or of the "volume" type (detection area dimensions comparable to thickness - for example, a cube). The present contract requires measurement of the electron induced dose in a realistic configuration (one that simulates the effect of the satellite), with additional flux measurements. Thus, this instrument is, apparently, the first to combine these two concepts. As we show, however, it was necessary in the design to choose the primary objective.

since the two measurements could not simultaneously be optimized. We chose the design which optimizes the realistic dose measurement.

Partially due to this difficulty in instrument design, an experiment has been constructed and flown (Ref. 2.17) which directly measures the radiation dose effect on a series of CMOS (semiconductor) circuit devices, placed behind various shield thicknesses. It is called the CREM (CMOS Radiation Effects Measurement) experiment. In order to simulate the satellite effectively, the shields are constructed of aluminum (most satellite materials are in the atomic number range of aluminum: silicon, magnesium). These devices are essentially all of the planar type, so that a dome sensor designed to measure the radiation effects on such devices should also be planar. This CREM experiment was flown on the Explorer 55 spacecraft in 1975; the orbit was principally within the inner radiation zone. This emphasizes the fact that, although much is apparently known of the inner zone proton fluxes, it is still believed to be necessary to make this type of inner zone dose effect determination. For shields greater than about 100 mils Al, almost the entire dose is due to protons (see Figure 2.10 below) in this zone. Clearly, if the proton fluxes were known with sufficient precision, it would not be necessary to make such measurements. The device effects of proton dose can readily be measured in the laboratory, and the dose due to any proton spectrum is calculable in a straightforward manner. Hence, the present instrument has been designed such that it can measure and separate the dose and fluxes due to both electrons and protons.

The 1963 experiment that used dome sensors also attempted to make a very high energy electron integral flux measurement. It used four domes, the thickest designed for a threshold of 9.4 MeV. The shields apparently (Ref. 2.11, Table 1) were made of Al except for the highest, which was Cu. A planar detector was used with an energy deposition threshold of about 300 keV, which should minimize the contribution of bremsstrahlung counts. (It must be remembered that the objective was to measure electron flux, not the dose.) The instrument was launched into an inner radiation zone orbit just after the Starfish nuclear detonation in 1962, which produced a very large insertion of high energy electrons (fission betas). The effects lasted several years, but disappeared well before 1970. This type electron spectrum is much harder (has many high energy electrons) than that which normally exists in the inner zone. Interestingly, even for this hard spectrum the 9.4 MeV dome was useless, for purposes of determining the flux, due to bremsstrahlung produced in the shield. Calculated corrections for the other domes were said to indicate relatively small bremsstrahlung contributions. Flux data were, in fact, presented for spectrum thresholds in the 3-4.5 MeV region (Refs. 2.7, 2.11).

It is important to note that the "amount" of bremsstrahlung produced in a given material is roughly proportional to the atomic number ( $Z$ ) of the material. Hence, from the viewpoint of electron flux measurements it would be desirable to use the minimum  $Z$  possible for the shields. This approach was taken for

the ATS-6 instrument (Ref. 2.12), where the two highest energy domes used beryllium shields. The reason this is necessary for the high energy shields is that the spectra are generally decreasing functions of energy. Electrons which cannot penetrate a particular shield still can produce much bremsstrahlung that can penetrate it and then interact with the detector. Thus, for a "soft" spectrum, the amount of bremsstrahlung produced by the many low energy electrons can make it very difficult to separate the associated counts from those due to the few high energy electrons that actually penetrate the shield. (This is discussed in detail in Ref. 2.11, p. 2013). A hard spectrum flux is, therefore, much easier to measure with dome detectors than is a soft spectrum flux. This is what made it possible to measure the  $> 4.5$  MeV flux due to Starfish (Refs. 2.7, 2.11), although the  $> 9.4$  MeV flux was still not measurable, in spite of the hardness of the spectrum at that time.

For the present condition in the inner zone, Cliff et al. (Ref. 2.17) have made calculations, using recent models for the orbit encountered, of the radiation induced dose due to inner zone protons and electrons. The results are shown in Figure 2.10 below.

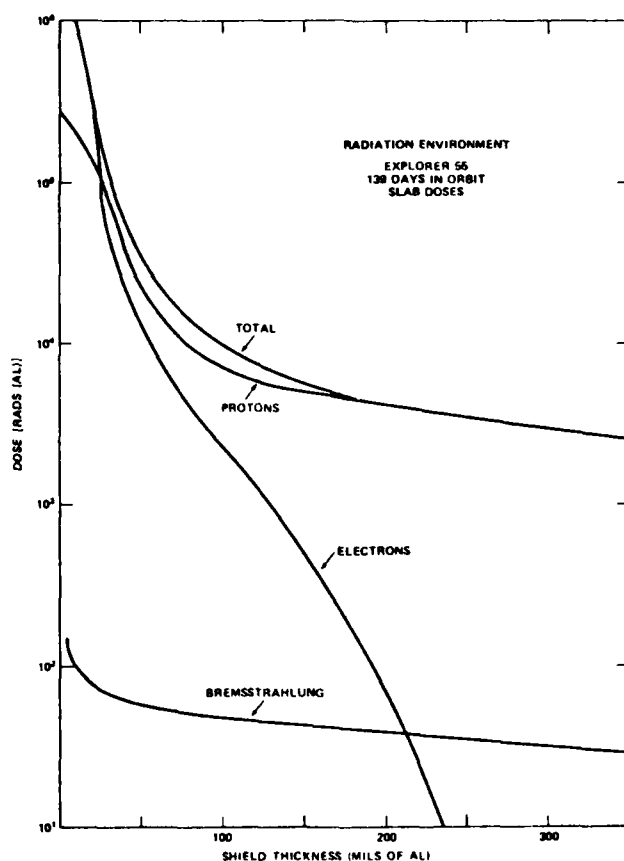


Figure 2.10 Contribution of Electrons, Protons, and Bremsstrahlung to the Total Dose-depth Curve (taken directly from Ref. 2.17, Fig. 7)



The point at which the bremsstrahlung and direct electron doses are equal is about 220 mils Al ( $\approx 1.5 \text{ g/cm}^2$ ). This is an electron range energy of about 2.5 MeV. Thus, for any aluminum dome having a larger thickness than  $1.5 \text{ g/cm}^2$ , the inner zone electron bremsstrahlung effect will dominate the direct flux effect - overwhelmingly for domes 3 and 4 in Table 2.1. Outer zone electron spectra are somewhat harder than inner zone (compare the ratios of  $>1$  to  $>4$  MeV flux in Figure 5, Ref. 2.17 - for the inner zone - with Figure 2.4 above for the outer zone). Hence, the effect of bremsstrahlung is not likely to be as important in that region. Perhaps, for the outer zone, the bremsstrahlung contribution in dome 2 would be less than that due to the direct penetrating flux, but it is still likely to be dominant in the two higher energy domes. Of course, for any orbit penetrating the inner zone, it is also clear from Figure 2.10 that almost all of the dose will, in fact, be produced by protons in domes 2-4 (this fact is, of course, independent of the dome material). For dome 1, however, the electron flux induced dose will be significant compared to that due to protons. It would certainly form a significant fraction of the total dose due to electrons for an orbit passing through both inner and outer zones - see Figure 2.3. Again, we note that it would not be possible to deduce this inner zone electron dose from the measurements unless the proton flux is also measured - thus, allowing subtraction of that unavoidable background in the electron dose counter. Such proton contamination is discussed in detail in Ref. 2.11, p. 2012, as well as in most of the other references cited on this subject.

Comparison of Fig. 2.10 with Fig. 4 of Ref. 2.21 suggests that the TIGER code apparently does not predict as large bremsstrahlung doses as does the procedure used in Ref. 2.17 (which was used here to estimate this effect). This accounts for a part of the difference in theoretical dose estimates discussed in Section 2.2.3 above.

In the early implementation of this type sensor (Refs. 2.7-2.9), the detectors were planar. However, in an effort to provide a better measure of the omnidirection flux, the detectors were changed to the volume type (specifically, Si(Li) cubes; Refs. 2.10-2.12). Such detectors were also used on the TIROS spacecraft for the lowest energy dome (Refs. 2.13, 2.14), as shown in Figure 2.11, and on DMSP F-1 for dose measurement (Ref. 2.21). On TIROS the higher energy domes used planar detectors mounted on a three-sided truncated pyramid. This would be an interesting configuration, if the primary objectives were making flux measurements. It makes use of standard planar detectors (more readily available than the cubes).

The SMS-1, -2 and GOES A spacecraft also used the cubical type detectors. However, anomalous behavior was observed in the calibration work (Ref. 2.15); and for GOES B and C, the detectors were changed to the planar type. Another contributing factor to that change may be that the original manufacturer (Solid State Radiations Inc., now known as Quantrad Corp.) no longer manufactures these devices. They are, apparently, only interested in setting up to produce these detectors at an extremely large cost. Hence, they were not considered for this program.

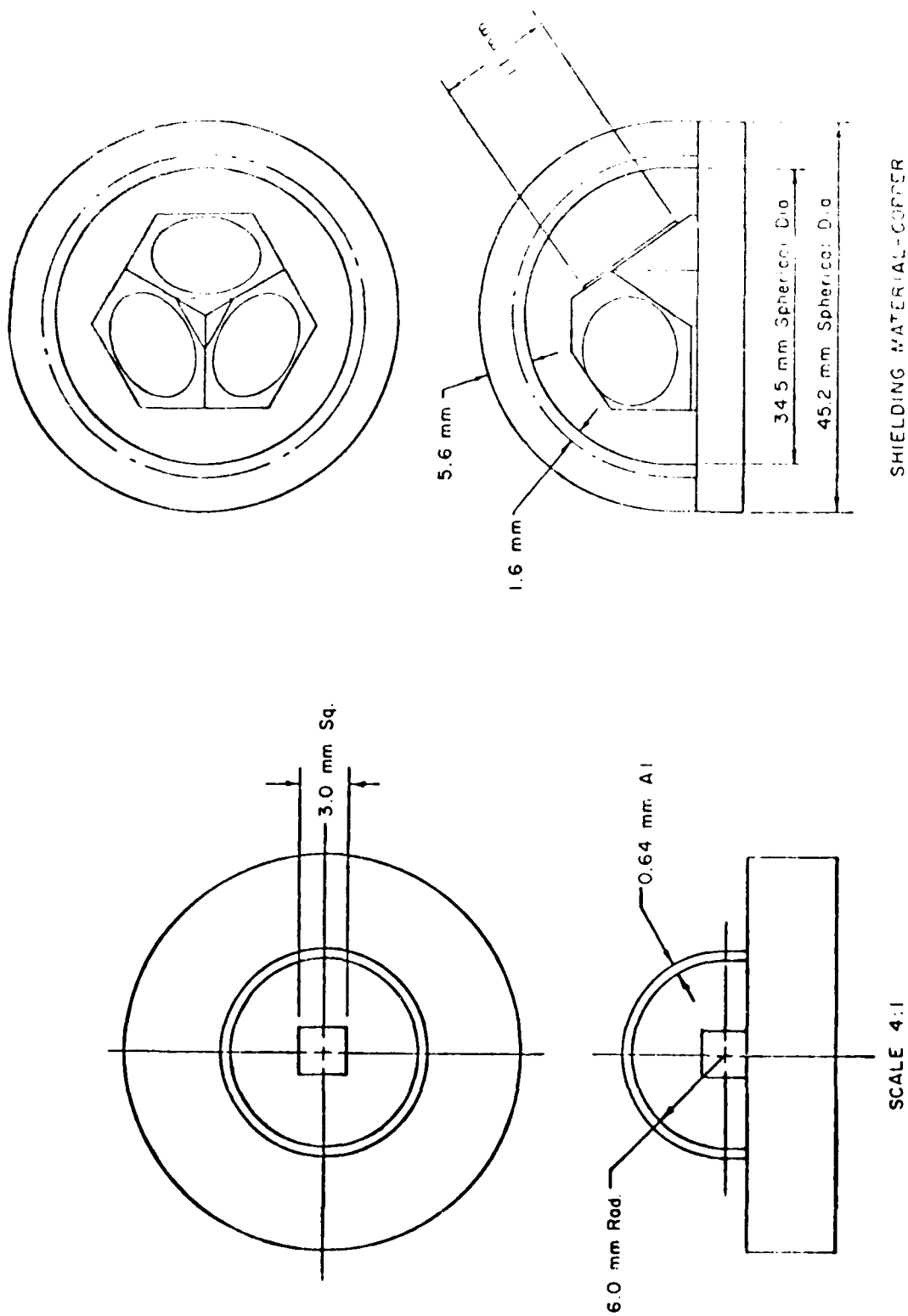


Figure 2.11 TIROS Dome Detectors (Taken directly from Ref. 2.14, p. 50)

We believe that it is desirable to use a planar type detector in the configuration of Fig. 2.9. The principal reason is that actual semiconductor circuit devices are planar, so that to measure dose effects in the most realistic geometry, the detector should also be planar. For a similar reason we believe that the shields should all be aluminum. Because they produce more bremsstrahlung than, say, beryllium, they simulate best the effect of actual spacecraft structures. Such spacecraft-induced bremsstrahlung can produce a large part of the dose (as discussed above), and it is definitely measured in experiments like CREM (Ref. 2.17). We believe that this may very well cause the two higher energy domes to produce marginal data from the view-point of the flux determination. But they will make an accurate measurement of the dose to be expected behind actual spacecraft construction materials. The data could probably be presented in a form similar to that below, i.e., the variation of dose with shielding thickness (obtained from Table 2.1).

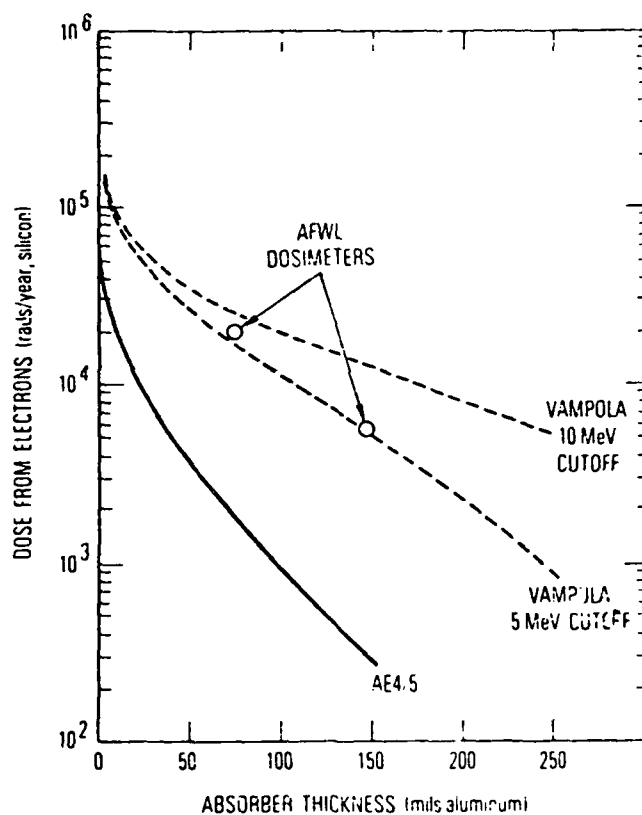


Figure 2.12 Results of Monte-Carlo Energy Transport Calculations for the AE4/5 and OV3-3 "Average" Spectra.

(Taken directly from Ref. 2.3, Fig. 4. See that reference for discussion of "Average" spectra.)

A series of such plots could be made for each particle type for the various regions of space, time encountered by the satellite. Another example is given in Fig. 5 of Ref. 2.21 (which gives total dose for several thin shields up to 125 mils) for the 1977 average DMSP orbit conditions, with no separation due to particle type.

The detector that we selected is a p-i-n diffused junction silicon semiconductor, with a guard ring. They are normally packaged as photodiodes (with light transparent window) but they can be obtained as unpackaged silicon chips and mounted as desired. The specific devices of interest are the YAG series manufactured by EG & G Inc. We first became aware of this type of device from work in which they were coupled directly to a scintillator to replace a photomultiplier (Ref. 2.18). For that application, the detector noise had to be very low. Similar silicon junction detectors have also been used to detect protons (which requires a very thin dead layer on the front) on rocket flights (Ref. 2.19). Consequently, we procured a Model YAG-100 having an area of  $5 \text{ mm}^2$  and tested it with an electron conversion source,  $\text{Sn}^{119}$ , which emits monoenergetic electrons with energies of 20, 36, and 41 keV. The results are shown in the multichannel analyzer picture in Figure 2.13 below - note that the scale is logarithmic. Even the 20 keV peak is almost resolved at its half width, so it was possible to set a threshold of 50 keV. It was necessary to set such a reasonably low energy deposition threshold in order to detect as much of the bremsstrahlung as possible, while not compromising on-orbit lifetime.

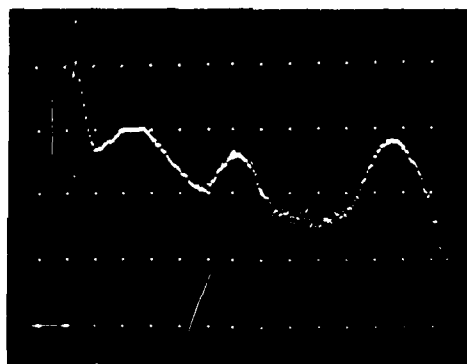


Figure 2.13 Spectrum of  $\text{Sn}^{119}$  with YAG-100 Diffused Junction Silicon Semiconductor Detector

These detectors are available with active areas of  $.051 \text{ cm}^2$  and  $1.0 \text{ cm}^2$ . As shown in Table 2.1, we used a larger area as the energy threshold increases in order to maintain good counting statistics. This is similar to the approach taken in Ref. 2.12 for AIS-6, but it will yield somewhat larger geometrical factors appropriate to the DMSP orbit. The detectors can be totally depleted at a voltage less than 200 volts. The depletion depth is nominally  $.0457 \text{ cm}$  for both of them, although the purchased detectors were measured to be about  $0.040 \text{ cm}$ . These detectors are readily available (they have been for several years), and similar area units are made by other photodiode manufacturers, (Centronic, for example). These are standard semiconductor type detectors, and we are confident they will easily exceed the required 10 rad dose.

Briefly, in summary:

- 1) For an instrument such as this in which the primary objective is dose measurement in a realistic configuration, the shields should all be constructed of aluminum (to simulate actual spacecraft structure material), and the detectors should have a planar configuration (to simulate the configuration of actual semiconductor circuit devices).
- 2) For the DMSP nominal orbit (inner edge - inner zone), the lowest energy dome and the detector area should be near  $.051 \text{ cm}^2$  in order to keep the counting rate low. Larger detection areas should be used for the higher energy domes in order to optimize the statistical accuracy of the count obtained.
- 3) Previous dome sensors that used aluminum, or high Z materials, for shields have had significant fractions of the response produced by bremsstrahlung, in one case rendering a flux determination attempt totally useless for  $>9.4 \text{ MeV}$  electrons. For an electron spectrum as soft as that which presently exists in the radiation belts (no recent high altitude nuclear detonations), it also is likely that the  $5 \text{ MeV}$  threshold detector will be strongly influenced by bremsstrahlung. Thus, it may not be possible to determine an effective threshold energy for penetrating electrons for the highest energy domes. But, as long as the dome material is similar to that of spacecraft, the total measured dose is a very meaningful parameter; more meaningful than if the domes were constructed of a low Z material in order to reduce bremsstrahlung, and hence, enhance the flux determination. In fact, this approach would totally eliminate any possibility of making a realistic dose determination in the highest energy domes (see electron and bremsstrahlung response in Figure 2.10). We believe, therefore, that (a) the two lowest energy domes should be calibrated for energy threshold determination and angular response for purposes of flux measurement, and (b) all four (4) detectors should be carefully calibrated for the dose determination in order to allow presentation of realistic dose data in the form dose vs. shield thickness. These calibration results are discussed in Section 2.6 and in Section 4.

## 2.4 Dose Measurement Concept

In this section, the approximate geometrical factor for a planar detector is derived first, which allows selection of the detection areas necessary for achieving optimum statistical accuracy. This is followed by a discussion of the method of separation of electrons and protons based on their energy deposition characteristics in the detectors; the general concept of the proposed in-flight calibration techniques is then presented.

### 2.4.1 Approximate Geometrical Factor

For a spinning satellite, the effective flux is nearly isotropic for a time-averaged distribution on a planar surface. Hence, in the geometry of Figure 2.7, we assume an isotropic flux  $F(E) \text{ (cm}^{-2} \text{ sec}^{-1} \text{ sr}^{-1})$  of electrons greater than some energy  $E_1$ . Then the counting rate  $C(E_1)$  for a plane detector

of area A is

$$\begin{aligned}
 c(E_t) &= F \int_{2\pi sr} A \cos\theta d\Omega \\
 &= FA \int_0^{2\pi} \int_0^{\pi/2} \cos\theta \sin\theta d\theta d\phi \\
 &= \pi FA \text{ sec}^{-1}
 \end{aligned} \tag{2.1}$$

Now, the omnidirectional flux  $F_o$  through a sphere is

$$F_o(E_t) = 4\pi F(E_t)(\text{cm}^2\text{-sec})^{-1} \tag{2.2}$$

so that

$$\begin{aligned}
 c(E_t) &= F_o(A/4) \\
 &= F_o A_o
 \end{aligned} \tag{2.3}$$

where  $A_o$  is the "effective area" of a plane of area A for detection of an isotropic omnidirectional distribution through only  $2\pi$  steradians (as in the dome detectors)

$$A_o = A/4 \text{ cm}^2 \tag{2.4}$$

Thus, by use of the detector areas in Table 2.1, and the fluxes in Table 2.5, the count rates can be calculated from (2.3). Results are given below.

#### 2.4.2 Separation of Electrons, Protons and Nuclear Stars

The technique for separation of protons and electrons in sensors of this type is well established. We show in Figures 2.14-2.17 the energy deposited in the detector for normal incidence and for the average path length in the detector; this path length can easily be shown to be twice the detector thickness for an isotropic incident spectrum. These calculations were made for a nominal 457 micron thickness; the actual thicknesses measured were nearer 400 microns, hence the actual energy losses are about 10% less than shown. Stopping power data were taken from Refs. 2.1, 2.2 and 2.20. In actual practice, the electron curves would be strongly modified due to scattering and bremsstrahlung production in the shields. Figure 2 of Ref. 2.8 shows that there is very little difference in the counting rate per unit of incident flux for angles between  $0^\circ$  and  $45^\circ$ ; at  $90^\circ$  incidence angle, the response is only down by about 25-50% from the maximum. This is due to the fact that even at  $90^\circ$  angle of incidence, where the detector

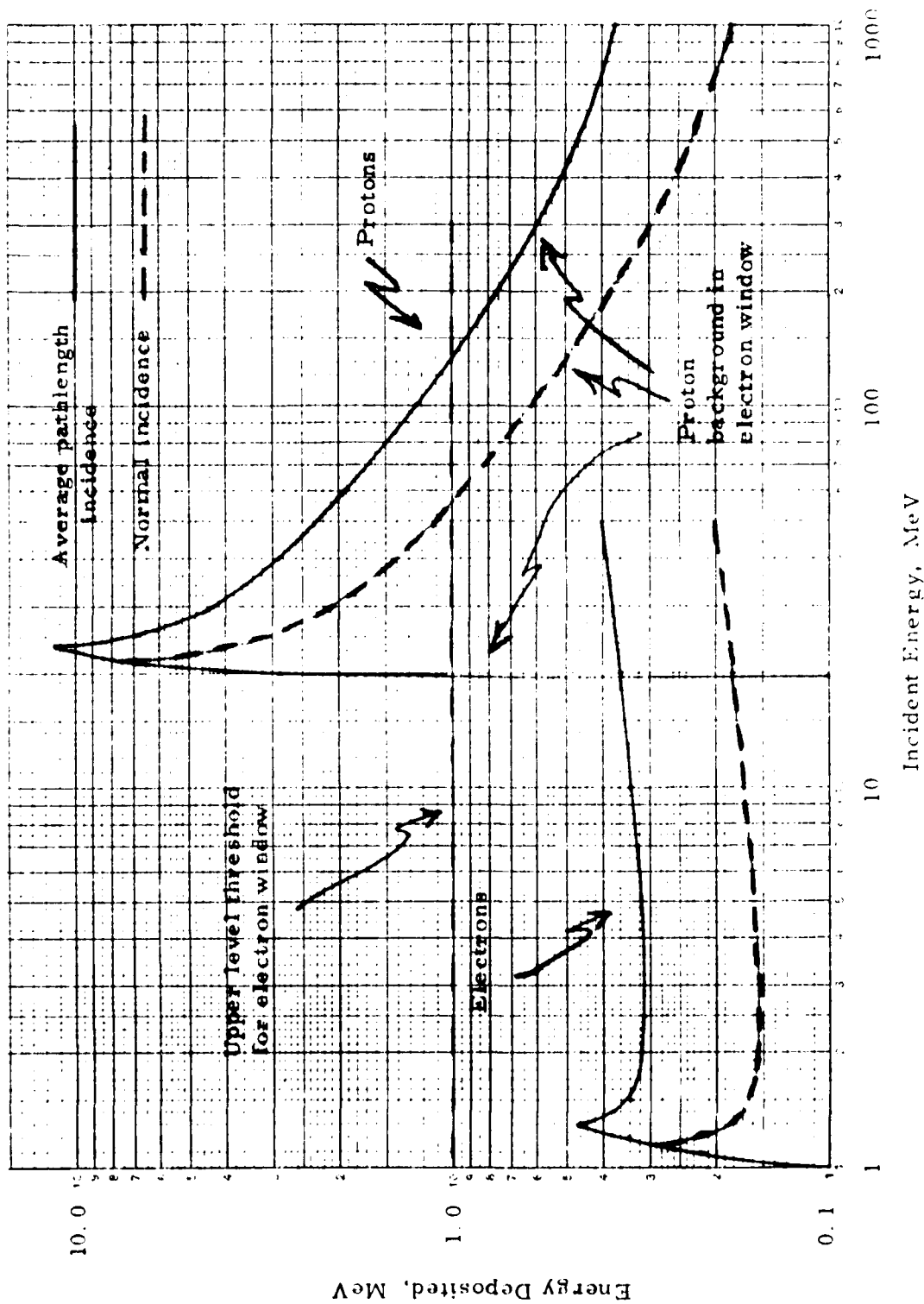


Figure 2.14 Energy Deposition Curves for Dome 1.

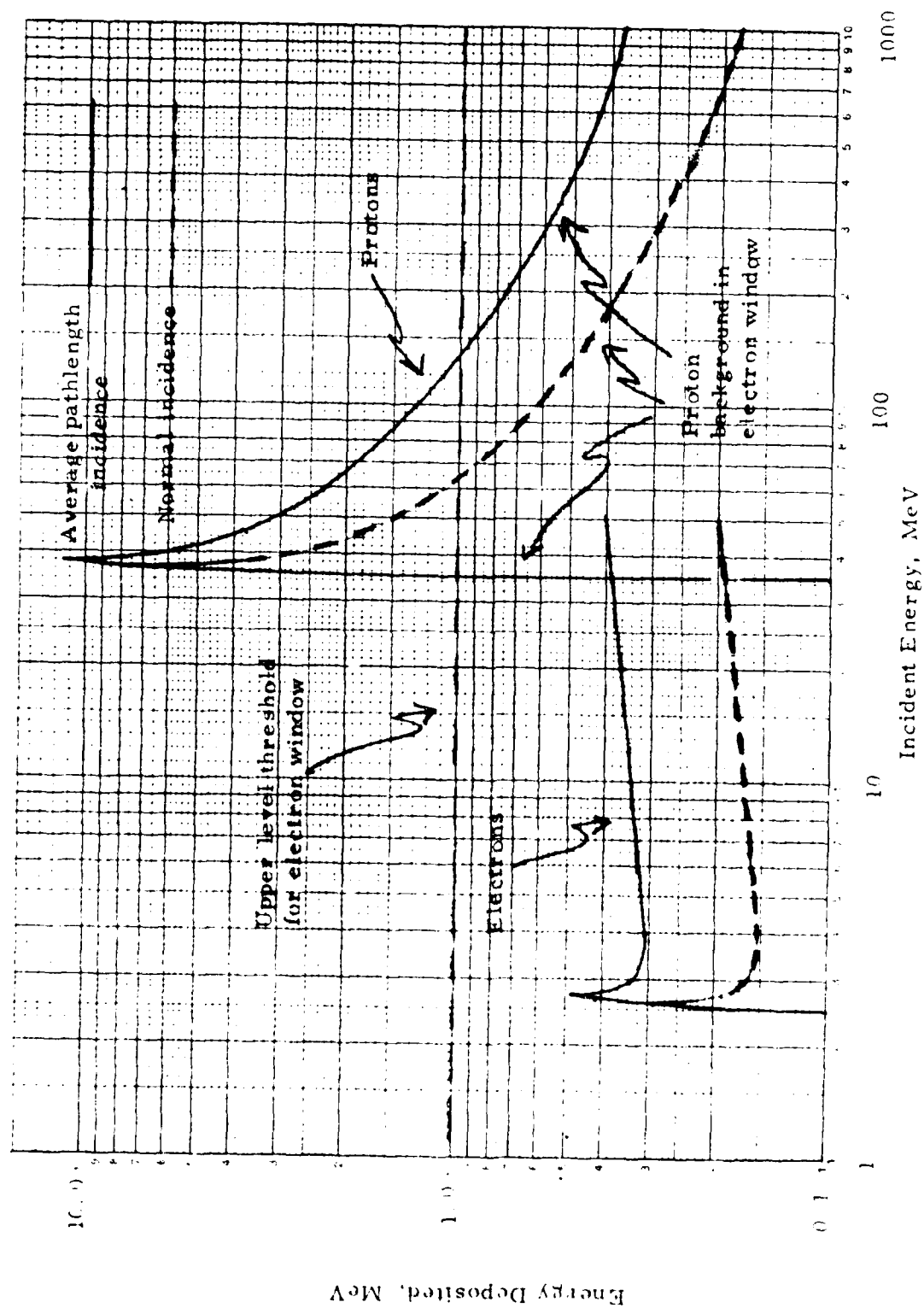


Figure 2.15 Energy Deposition Curves for Dome 2.



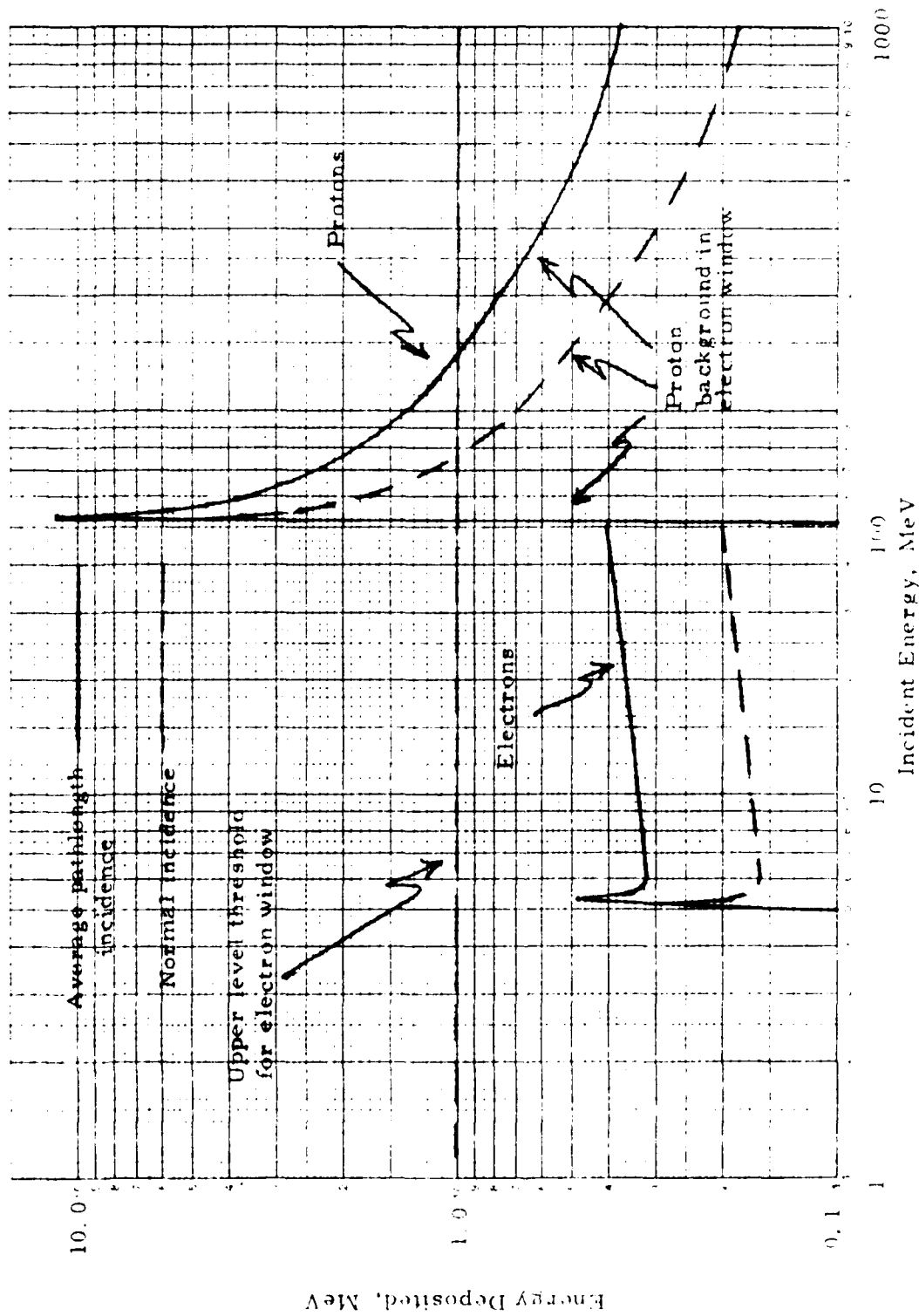


Figure 2.16 Energy Deposition Curves for Protons and Electrons

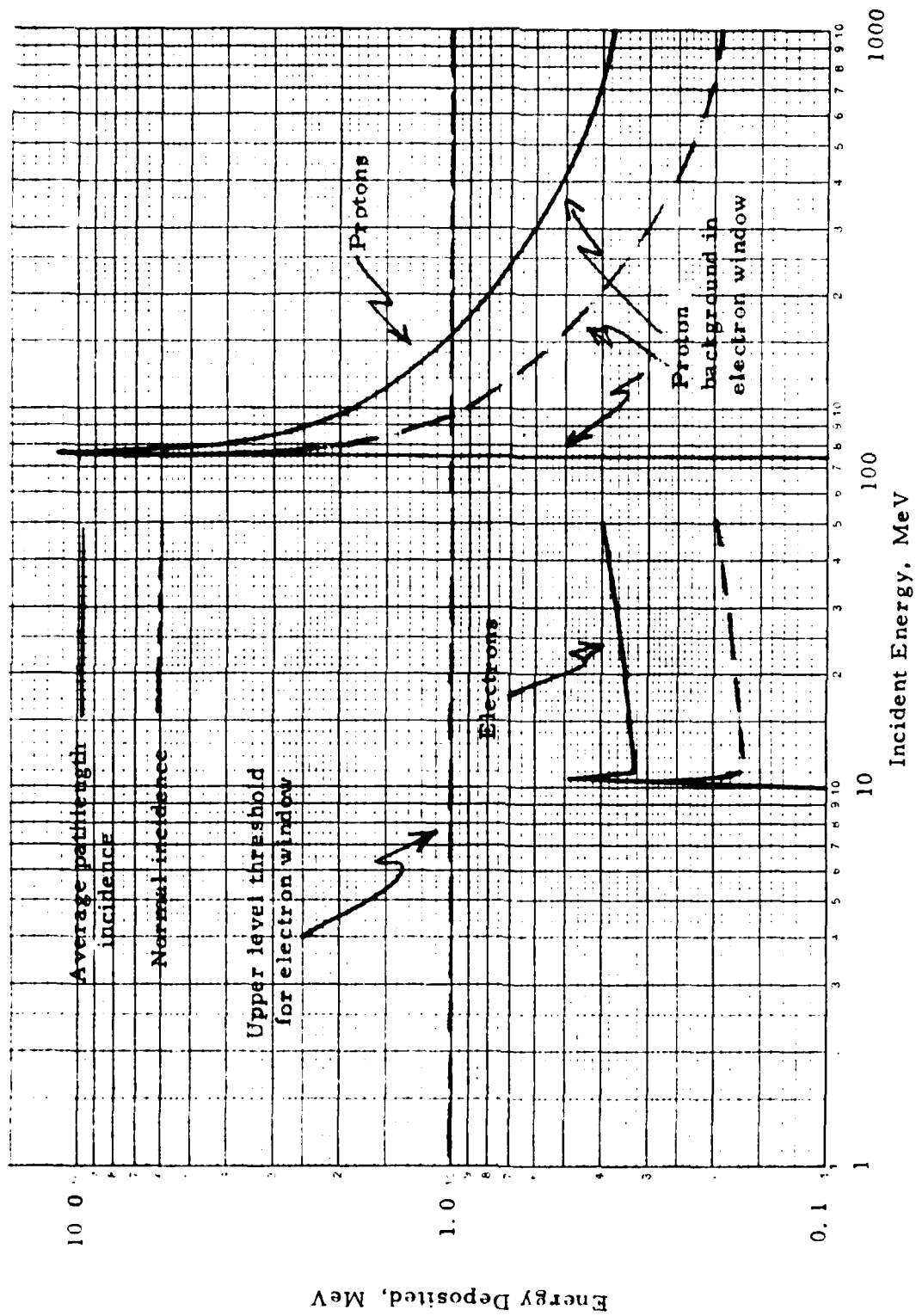


Figure 2.17 Energy Deposition Curves for Dome 4.

cannot be irradiated directly, a large amount of scattering occurs in the dome, causing electrons to strike the detector.

For protons, neither scattering nor bremsstrahlung is a problem, and the energy loss curves will be very nearly as shown.

These curves show quite clearly that, for any given dome, it is impossible to establish more than one energy threshold by using different energy deposition thresholds. For those particles with sufficient energy to penetrate the shield, the energy deposited depends much more strongly on angle of incidence than on the incident energy. Consequently, in order to detect (a) as many of the singly scattered electrons (which deposit smaller amounts of energy than indicated in the figures), and (b) the maximum amount of bremsstrahlung possible (which contributes significantly to the dose), the lower threshold was set to 50 keV (about 1/2 the minimum energy deposition shown on the graphs). To allow for multiple scattering effects, and large angles of incidence, the upper level for electron detection must be set at about 1 MeV. It can be seen from each graph that there will be an unavoidable range of proton energies that contributes to the electron window. It is also quite clear that, by making the proton flux measurements (counting all energy depositions exceeding ~ 1 MeV), it will be possible to make a spectral fit to determine the actual proton spectrum and calculate its background effect on the electron channel, both from the viewpoint of dose and flux. Additionally, the proton dose will be separated from that due to electrons.

A third, very high, energy threshold was also added to detect large energy losses from proton-caused nuclear star disintegrations and from high energy, high -Z cosmic ray particles. This star threshold was selected to be above most of the normal proton energy losses to avoid significant contamination of the rare nuclear star events.

In accord with the above, we concluded that in order to meet the intent of measuring the dose due to four different energy ranges, it is necessary to use four shields; and this concept is used in the sensor design presented in Section 3.

#### 2.4.3 In-Flight Calibration Concept

The method of in-flight calibration involves irradiation of each detector from the rear by a small ( $\approx 0.3$  nCi)  $\text{Am}^{241}$  source, which emits ~ 5.5 MeV alpha particles. Between source and detector is a thin foil that changes the shape of the spectrum such that it peaks near 3 MeV and has a half-width of 1-2 MeV. In the normal mode of operation, all pulses from this source will deposit enough energy that they will not appear in the electron window between 0.05 and 1.0 MeV. During the calibration mode, two changes are made: (1) the amplifier gain is reduced by a factor of about 3, which causes the alpha peak to straddle the p/c threshold, and (2) the lower threshold is moved upward to the equivalent of

1 MeV (at the new gain setting). This increase in lower threshold allows the calibration to be made in the presence of much larger electron fluxes, since they will deposit much less energy than that required to trigger this level. Since the  $\alpha$  peak is fairly narrow, it will require only a small gain shift to substantially change the upper/lower CAL flux ratio.

Thus, for this concept, the counts must be recorded for all particles in the two windows given in Table 2.7. Once these counts are recorded, the entire sensor gain shift can be determined by any changes in the counts that occur. This includes the detector, amplifiers, and threshold determining circuitry. Since the source will be located on the back of the detector, it will also allow a check that the detector is totally depleted - a decrease in depletion would show up as a decrease in gain. During lab testing data were recorded for use during in-flight diagnosis.

Since the source is mounted very close to the detector (on its rear), it is quite possible to carry out these checks on the ground (there is no significant air path to degrade the alpha energies). In-flight calibration must be initiated at a time when the energetic proton flux is low, since the protons will appear in the calibration window. Essentially, this means that the calibration cannot be carried out while in the inner radiation belt.

Use of the term "electron" or "proton" in the previous discussion is not meant to imply absolutely positive identification of the particle. The terms refer to deposited energy analysis ranges as in Table 2.7, based on Figures 2.14-2.17. Similarly, the term "star" refers to very high energy loss events, as shown in Table 2.7.

TABLE 2.7  
Energy Window Limits

Quantity	Lower Limit (MeV)	Upper Limit (MeV)
Electron	.05	1
Proton	1	10
L Cal	1	3
U Cal	3	10
Star	40 (CH 1, 2, 4) 75 (CH 3)	None

## 2.5 Design Features

This section contains the general features of the design that followed from the above considerations. First, we present the electronic dose measurement concept; this is followed by a discussion of the flux and dose capacity of the instrument. The compression counter characteristics are discussed next, followed by the resulting flux accuracies.

### 2.5.1 Electronic Dose Measurement Concept

For any material the dose  $D(\text{rad})$  is related to the energy deposited by

$$D = \epsilon / (k_o M) \quad (2.5)$$

$$\text{where } k_o = 6.24 \times 10^7 \text{ (MeV/g)/rad} \quad (2.6)$$

$M(\text{gram})$  is the device mass, and  $\epsilon(\text{MeV})$  is the energy deposited. For a detector of area  $A(\text{cm}^2)$ , thickness  $d(\text{cm})$ , and density  $\rho(\text{g/cm}^3)$  this can be written

$$\begin{aligned} D &= \epsilon / (k_o A d \rho) \\ &= K \epsilon \end{aligned} \quad (2.7)$$

$$\text{where } K = 1 / (k_o A d \rho) \text{ rad/MeV} \quad (2.8)$$

The actual detector thicknesses are listed in Table 4.1. If a thickness of 0.0457 cm is assumed, and the density of silicon ( $2.33 \text{ g/cm}^3$ ) substituted for  $\rho$  the following expression is obtained

$$K = 1.505 \times 10^{-7} / A(\text{cm}^2) \text{ rad/MeV} \quad (2.9)$$

Provided the actual area  $A$  is known precisely, (2.7) can be used with (2.9) directly. In practice it is necessary to deposit a known (measurable) energy in the detector and, for the assumed (closely correct) area  $A$ , calculate the resulting dose  $D$  from (2.7). The dose sensor dose scaler can then be carefully calibrated by finding the ratio of calculated dose to the counts in the dose counter. Fortunately, the detectors to be used have a guard-ring construction that allows a very accurate definition of the detection area.

The electronic system to be used for the dose measurement consists, basically, of the parts shown in Figure 2.18 below.

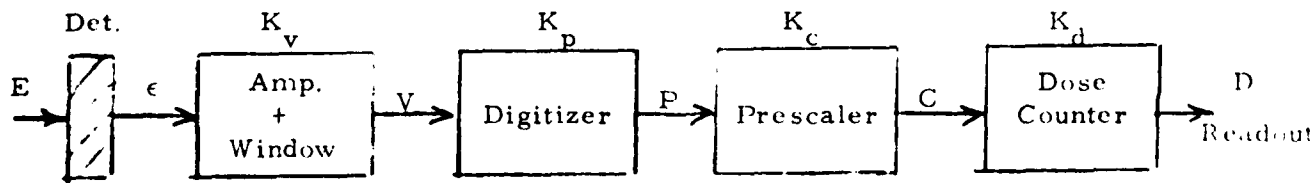


Figure 2.18 Basic Dose Measurement System

Figures 2.14-2.17 show the energy  $\epsilon$  deposited by different particles in the various Domes for 457 micron thickness. The star threshold was defined by use of results provided by AFGL. Particles of energy  $E$  enter the detector, depositing an energy  $\epsilon$  and producing a charge pulse. This charge pulse goes through shaping and amplification, and if the pulse is within the particle windows, it is digitized to determine its height precisely. The summation of the heights of all such pulses (not the number of counts passing through the window) is proportional to the dose deposited in the detector. Thus, the digitizer produces an output number of pulses, each of standard size, proportional to the height of each voltage pulse caused by detection of a single particle. These digitizer pulses are prescaled to provide a convenient, meaningful input to the dose counter.

The appropriate equations are as follows:

$$\begin{array}{ll} \epsilon = \text{energy deposited} & \epsilon = \text{MeV} \\ V = K_v \epsilon \text{ volts} & K_v = \text{volts/MeV} \\ P = K_p V \text{ pulses} & K_p = \text{energy pulses/volt} \\ C = P/K_c \text{ cts} & K_c = \text{energy pulses/dose ct} \\ D = K_d C \text{ rad} & K_d = \text{rad/dose ct} \end{array}$$

Thus, the dose is given by

$$D = K_d C = K \epsilon \quad (2.10)$$

$$\text{where } K = K_p K_v K_d / K_c \quad (2.11)$$

must be the same value given by Eq. (2.9). It is then convenient to solve this for  $K_d$ ,

$$K_d = K_c K / (K_p K_v) \quad (2.12)$$

We can choose convenient values for  $K_p$  and  $K_v$ , use the value of  $K$  from (2.9), and thus find the number of  $\text{rads}^v$  per dose count. Choosing the following for  $K_p K_v$ :

Norm Mode	{	$K_p K_v = 16 \text{ pulses/MeV}$	Electrons
		$= 1.6 \text{ pulses/MeV}$	Protons
Cal Mode	{	$K_p K_v = 5.333 \text{ pulses/MeV}$	Electrons
		$= .533 \text{ pulses/MeV}$	Protons

yields the results for  $K_p$  and  $K_d$  given in Table 2.8 at the bottom. These values of  $K_c$  and  $K_d$  are based on our approximate calculations using the

TABLE 2.8  
DOSE CAPACITY, FLUX CAPACITY & PROCESSING RATE LIMIT  
WITH ESTIMATES OF EXPECTED DOSES & FLUXES\*\*

PARAMETER	CH 1	CH 2	CH 3	CH 4	UNITS
Dose to fill Electron Counter	12700	1290	323	323	RADS
Dose to increment Electron Counter*	$1.51 \times 10^{-3}$	$1.54 \times 10^{-4}$	$3.85 \times 10^{-5}$	$3.85 \times 10^{-5}$	RADS
Dose to fill Proton Counter	990	808	202	202	RADS
Dose to increment Proton Counter*	$1.18 \times 10^{-4}$	$9.63 \times 10^{-5}$	$2.41 \times 10^{-5}$	$2.41 \times 10^{-5}$	RADS
Dose to fill Lower CAL Counter	$1.41 \times 10^{-4}$	$7.20 \times 10^{-6}$	$7.20 \times 10^{-6}$	$7.20 \times 10^{-6}$	RADS
Dose to fill Upper CAL Counter	$1.41 \times 10^{-3}$	$7.20 \times 10^{-5}$	$7.20 \times 10^{-5}$	$7.20 \times 10^{-5}$	RADS
Estimate of Dose due to Electrons	5000 $6.34 \times 10^{-4}$	800 $1.01 \times 10^{-4}$	375 $4.76 \times 10^{-5}$	225 $2.85 \times 10^{-5}$	RADS/YEAR RADS/Readout
Estimate of Dose due to Protons	375 $4.76 \times 10^{-5}$	215 $2.73 \times 10^{-5}$	145 $1.84 \times 10^{-5}$	90 $1.14 \times 10^{-5}$	RADS/YEAR RADS/Readout
Processing Rate Limit .1 MeV	0.094	0.0048	0.0048	0.0048	RADS/Readout
Processing Rate Limit .5 MeV	0.31	0.016	0.016	0.016	RADS/Readout
Processing Rate Limit .9 MeV	0.42	0.021	0.021	0.021	RADS/Readout
Processing Rate Limit 1 MeV	0.94	0.048	0.048	0.048	RADS/Readout
Processing Rate Limit 5 MeV	3.1	0.16	0.16	0.16	RADS/Readout
Processing Rate Limit 9 MeV	4.2	0.21	0.21	0.21	RADS/Readout
Flux to fill Electron Counter	2,409,412	122,880	Same	Same	$\text{cm}^{-2} \text{ sec}^{-1}$
Flux to fill Proton Counter	19,451	922	as	as	"
Flux to fill Lower CAL Counter	2,409,412	122,880	CH2	CH2	"
Flux to fill Upper CAL Counter	19,451	922			"
Estimated Flux due to Electrons	9000	1800	850	450	$\text{cm}^{-2} \text{ sec}^{-1}$
Estimated Flux due to Protons	170	140	120	110	"
Avg ct rate due to Electrons	114.8	450.0	212.5	112.5	cts/sec
Avg ct rate due to Protons	2.2	35.0	30.0	27.5	"
Yearly avg dose per Electron	$1.38 \times 10^{-6}$	$5.65 \times 10^{-8}$	$5.60 \times 10^{-8}$	$6.35 \times 10^{-8}$	Rad/flux ct
Yearly avg dose per Proton	$5.40 \times 10^{-6}$	$1.95 \times 10^{-7}$	$1.54 \times 10^{-7}$	$1.04 \times 10^{-7}$	Rad/flux ct
Avg dead time per Electron	18.5	17.1	17.1	17.7	Microsec
Avg dead time per Proton	13.9	13.1	20.0	22.0	Microsec
Avg dead time fraction	0.0022	0.0082	0.0042	0.0026	fraction
Avg deposited energy per Electron	0.47	0.38	0.38	0.42	MeV/elec
Avg deposited energy per Proton	1.83	1.30	1.02	0.69	MeV/prot
K <sub>c</sub> For Electrons	8192	16384	4096	4096	Pulses/Count
K <sub>c</sub> For Protons	64	1024	256	256	Pulses/Count
Detector Area	0.051	1	1	1	$\text{cm}^2$

\*The dose to increment the counters is the same as the quantity K<sub>d</sub> in Eq. (2.12).

\*\*All data in this table are based on the nominal 457 micron detector thickness; the measured detector thicknesses do not change the values by more than about 10%.

spectra shown in Figure 2.7. Flux plots are shown in Figure 2.8, with tabulations for the various Dome thicknesses in Table 2.7. Our estimated doses are shown in the second section from the top and are accurate to, perhaps, a factor of 2 or 3. It is desirable that AFGL use the computer programs available to it to calculate those doses more accurately, if the time for the counters to overflow must be known with greater precision than the present accuracy factor.

The other quantities in Table 2.8 are based on results discussed in the subsequent sections.

### 2.5.2 Flux and Dose Capacity

Completion of the design has been based on the dose and flux estimates available at the time of fabrication. As noted, Table 2.8 lists the design dose and flux capacities estimated. However, since the prescale counters must be different for each channel, some adjustability is built in. This will allow  $K_c$  to be changed quite simply by factors of 2. Hence, the dose capacity can be scaled to correspond to the expected dose. This allows the capacity to be changed later, if necessary.

The processing rate limit given in the Table is for periodic equal energy pulses and corresponds to 100% dead time. For random timing, the data should be dead-time corrected unless the dose rate is substantially below this limit. For real data, the pulse energy will also vary, further complicating the analysis. For each particle detected, the dead time will be:

$$T_{dx} = T_a + (P_x - P_o)/f_o \quad x = p, e \quad (2.13)$$

Here  $T_{dx}$  = dead time due to detecting particle  $x$  and finding associated dose, sec

$T_a$  = data acquisition time:  $11.5 \times 10^{-6}$  sec/flux ct

$P_o$  = a constant used to correct average number pulses to center of digitization bin: 0.5 energy pulses/flux ct

$f_o$  = digitizer operating frequency:  $10^6$  (energy) pulses/sec

$P_x$  =  $K_c C_x$  = no. energy pulses produced by detecting particle  $x$ , pulses/flux ct

$C_x$  = no. dose cts produced by detecting particle  $x$ , dose cts/flux ct



The actual dead time over one or more readout periods can be calculated from the flight data. Since both particles are analyzed by the same digitizer:

$$T'_d = \sum_{i=1}^{C'_{fe}} T_{dei} + \sum_{j=1}^{C'_{fp}} T_{dpj}$$

Where  $T'_d$  = Total dead time during a specific data period, sec

$C'_{fe}$  = Electron flux count over a specific data period

$C'_{fp}$  = proton flux count over a specific data period

Substituting Eq. (2.13) into one term

$$\sum_{i=1}^{C'_{fx}} T_{dxi} = C'_{fx} \left( T_a - \frac{P_o}{f_o} \right) + \frac{1}{f_o} \sum_{i=1}^{C'_{fx}} P_{xi}$$

Now, since  $P'_x = K_c C'_x$  we obtain

$$\sum_{i=1}^{C'_{fx}} T_{dxi} = C'_{fx} \left( T_a - \frac{P_o}{f_o} \right) + \frac{K_c}{f_o} \sum_{i=1}^{C'_{fx}} C_{xi}$$

But,  $\sum_{i=1}^{C'_{fx}} C_{xi} = C'_x(r_1) - C'_x(r_0)$ , the incremental dose count for particle x

$$\text{So, } T'_d = (C'_{fe} + C'_{fp}) \left( T_a - \frac{P_o}{f_o} \right) + \frac{K_c}{f_o} \left[ (C'_e(r_1) - C'_e(r_0)) + (C'_p(r_1) - C'_p(r_0)) \right]$$

Where  $C'_x(r_1)$  = accumulated dose count at end of data period  $r_1$  for particle x

$C'_x(r_0)$  = previous dose count for particle x

The fractional dead time, U, is found by dividing by the channel readout interval

$T_r = 4$  seconds. The result can be extended to N data periods as below.

$$U = \frac{\left| \sum_{i=1}^N C'_{fe}(r_i) + C'_{fp}(r_i) \right| \left( T_a - \frac{P_o}{f_o} \right) + \frac{K_c}{f_o} \left[ (C'_e(r_N) - C'_e(r_0)) + (C'_p(r_N) - C'_p(r_0)) \right]}{N T_r}$$

The corrected count for a given data interval can then be found by:

$$C_{\text{Corr}} = \frac{C}{1 - U}$$

It is also possible to estimate the yearly dead time from the yearly doses and fluxes given in Table 2.8.

From the definitions given in Section 2.5.1,

$$D = K_d C \quad \text{and} \quad C = P/K_c$$

$$\text{So, } P_x = \frac{K_c D_x}{K_d} \quad x = e, p$$

Where  $D_x$  = Dose due to particle  $x$ , Rads/flux ct

Substituting into Eq. (2.13)

$$T_{dx} = \left( T_a - \frac{P_o}{f_o} \right) + \frac{K_c D_x}{K_d f_o}$$

The average yearly dead time is found by multiplying by the yearly flux count.

$$\overline{T_{dyx}} = \overline{C_{fx}} \overline{T_{dx}} = \overline{C_{fx}} \left( T_a - \frac{P_o}{f_o} \right) + \frac{K_c}{K_d f_o} \overline{D_x} \overline{C_{fx}}$$

From Eq. (2.3) and (2.4), we obtain:

$$\overline{C_{fx}} = \left( \overline{F_o} A/4 \right) T_y$$

Substituting, we obtain

$$\overline{T_{dyx}} = \frac{\overline{F_o} T_y A}{4} \left( T_a - \frac{P_o}{f_o} \right) + \frac{AK_c}{4K_d f_o} \overline{F_o} \overline{D_x} T_y$$

Where  $\overline{T_{dyx}}$  = Total dead time per year due to particle  $x$ , sec

$\overline{F_o}$  = Average omnidirectional flux rate of particle  $x$ ,  $\text{cm}^{-2} \cdot \text{sec}^{-1}$

$T_y$  = 1 year or  $3.16 \times 10^7$  seconds

$A$  = Detector area,  $\text{cm}^2$

$\overline{D_x}$  = Yearly average dose due to particle  $x$ , Rad/flux ct

The fractional dead time due to a particle is found by dividing by  $T_y$ .

$$\overline{U_x} = \overline{F_o} \frac{A}{4} \left[ \left( T_a - \frac{P_o}{f_o} \right) + \frac{K_c}{K_d f_o} \overline{D_x} \right] \quad (2.14)$$

It is convenient to define the following variables:

$f_{fe} = \overline{F_o} A/4$ , The average count rate due to electrons, given in Table 2.8, flux cts/sec

$f_{fp} = \overline{F_o} A/4$ , The average count rate due to protons, given in Table 2.8, flux cts/sec

$$S_0 = T_a - \frac{P_o}{f_o} = 11.0 \times 10^{-6} \text{ sec/flux count}$$

$$S_1 = \frac{K_c}{K_d f_o} \text{ Seconds/Rad}$$

$\overline{D}_x$ , the yearly average dose per particle can be found from the estimated yearly dose and estimated flux in Table 2.8 by the following equation.

$$\overline{D}_x = \frac{\frac{D_{yx}}{C_{fx}/T_y}}{\frac{D_{yx}}{f_{fx}}} \quad x = e, p \quad \text{Rads/flux ct}$$

Where  $D_{yx}$  is the yearly dose rate given in Table 2.8 in Rads/year for the appropriate particle.

Substituting the newly defined variables into (2.14), the result below is obtained.

$$\left. \begin{aligned} \overline{U}_p &= f_{fp} \left[ S_0 + S_1 \overline{D}_p \right] \\ \text{and} \\ \overline{U}_e &= f_{fe} \left[ S_0 + S_1 \overline{D}_e \right] \end{aligned} \right\} \quad (2.15)$$

The bracketed quantities ( $\overline{U}_x/f_{fx}$ ) are the average dead times per particle given in Table 2.8. The average dead time fraction is also given and is calculated by

$$\overline{U} = \overline{U}_e + \overline{U}_p = S_0(f_{fe} + f_{fp}) + S_1(f_{fp} \overline{D}_p + f_{fe} \overline{D}_e) \quad (2.16)$$

Throughout both analyses, events which deposit greater than 10 MeV energy have been ignored. It is expected that each such particle will produce a dead time in the order of tens of microseconds. The expected flux is, however, small enough that they may be neglected without significant error. In fact, the entire average dead time listed in the table is negligible compared to the statistical and compression counter uncertainties.

Thus, it can be seen that the actual doses and fluxes must be substantially greater than expected before the primary mission of measuring the accumulated dose is compromised. The correction procedures given will, nonetheless, be useful if it is desired to know the true intensity distribution of a flux or dose rate peak.

Note that the value of  $\overline{U}$  is largest for Dome 2, which is caused by the fact that the count rates are highest for that dome. The Dome 1 count rates are lower, even though the flux is higher, because the detector size to be used is .05 cm<sup>2</sup>, a factor of 20 less than that for the other domes.

As a test on the reasonableness of our dose and flux estimates, we note from Eq. (2.10) that the yearly average of energy deposited per particle detected can

be estimated crudely from  $\overline{E_x} = \overline{D_x} / K$  MeV/particle, where K is given by (2.9).<sup>\*</sup> Use of this equation with the values of  $\overline{D_x}$  in the table yields the results shown near the bottom of the table. The results for electrons vary little with the dome and reflect the fact that the doses have a significant estimated effect added due to bremsstrahlung. It is likely that we have overestimated the bremsstrahlung effect somewhat. However, it is encouraging that these energy depositions lie near those estimated in Table 2.7 above. The calculated average energy depositions are for electrons, of course; however, the estimated doses include the bremsstrahlung effect-which is particularly important in Domes 3 and 4. It is likely, therefore, that the average energy deposited per count in these two domes will be significantly less than that given in Table 2.8 for electrons. The proton results in Table 2.8 show that the average deposited energy decreases as the dome number increases, which is caused by the fact that the response is increasingly due to higher energy protons (lower stopping power - see Figures 2.14 - 2.17).

### 2.5.3 Compression Counter Characteristics

The dose counts must be compressed in order to allow long accumulation periods without overflow. The type compression counter used is such that the minimum number of counts that has entered the counter at any time is given by

$$C = M \times 2^E \quad (2.17)$$

where the displayed mantissa M and exponent E are given by

$$M = (m_a \times 2^a) + (m_{a-1} \times 2^{a-1}) + \dots + 2m_1 + m_0 \quad (2.18)$$

$$E = (e_b \times 2^b) + (e_{b-1} \times 2^{b-1}) + \dots + 2e_1 + e_0 \quad (2.19)$$

Here a+1 is the number of binary bits in the mantissa, and b+1 is the number in the exponent. The maximum values that M and E may have occur when  $m_n = e_n = 1$ , where

$$M_m = 2^a + 2^{a-1} + \dots + 2 + 1 = 2^{a+1} - 1 = 2^A - 1 \quad (2.20)$$

$$E_m = 2^b + 2^{b-1} + \dots + 2 + 1 = 2^{b+1} - 1 = 2^B - 1 \quad (2.21)$$

and

$$\begin{aligned} A &= \text{no. mantissa bits} \\ B &= \text{no. exponent bits} \end{aligned} \quad (2.22)$$

Thus, the maximum indicated count is

$$C_m = M_m \times 2^{E_m} \quad (2.23)$$

<sup>\*</sup>For the results in Table 2.8 the value of K used is that for the nominal 457 micron thickness.

The counter is designed such that when all bits are unity, the counter overflows to state zero on the next increment of the mantissa. (Note that this requires  $2^{E_m}$  input counts.) Hence, the result is that for repeated overflows the number of counts indicated will differ from the actual count by  $NC_o$ , where  $N$  is the number of overflows and  $C_o$ , called the overflow constant, is

$$C_o = (M_m + 1) 2^{E_m} \quad (2.24)$$

#### 2.5.4 Accuracy Characteristics

In order to extend the count capacity, while maintaining accuracy at low input counts, a 16 count (4 bit) ripple counter is placed between the prescaler (which is not read out) and the compression counter to form the dose counters. A 4x4 (4 bits mantissa, 4 bits exponent) counter is to be used for the doses which can be shown as follows with its ripple counter:

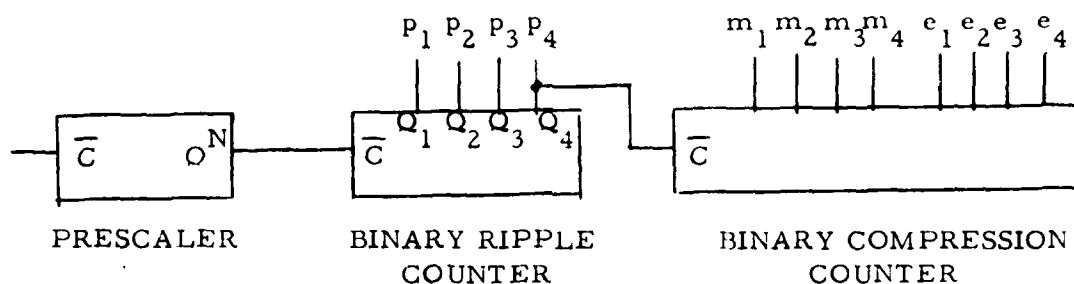


Figure 2.19 Dose Counter Bit Assignments

$N$  (as in  $Q^N$ ) is chosen such that  $p_1$  changes once per readout for the average doses expected. Each pulse from the prescale counter represents an increase in dose of  $K_d$  (dose calibration constant).

The ripple counter count  $P$  can be read exactly, of course, while there is uncertainty in the number of counts giving rise to an indicated compression counter reading. It can be seen that the most probable count causing an indicated count is

$$C = C_p + nC_o \quad (2.25)$$

where  $n$  is the number of overflows (each of which occurs only after many months of recording),  $C_o$  is given by (2.24), and  $C_p$  is the most probable count input to the counter since the last overflow:

$$C_p = 16M \times 2^E + 8(2^E - 1) + P \quad (2.26)$$

The value of  $P$  is

$$P = p_1 + 2p_2 + 4p_3 + 8p_4 \quad (2.27)$$

and for this counter, from (2.18) and (2.19),

$$E = e_1 + 2e_2 + 4e_3 + 8e_4 \quad (2.28)$$

$$M = m_1 + 2m_2 + 4m_3 + 8m_4 \quad (2.29)$$

The count (2.25) is that which is to be used in Eq.(2.10) to obtain the dose  $D$ . The dose counters, of course, are not reset at any time, so that the overflow problem discussed above is important for them. The flux counters are reset before each reading and are designed not to overflow.

The uncertainty in the indicated count is due to that in the compression counter. When  $E=0$  Eq.(2.26) is exact; there is no uncertainty. When  $E$  is large, however, we assign  $C_R=8$ , its most probable value, and obtain the most probable result for large counts as

$$C_{po} = 16 \times 2^E (M + 1/2) \quad (2.30)$$

Because of the nature of the compression counter, however, the uncertainty in this reading is

$$\Delta C = \pm 16(2^E/2) = 16(2^{E-1}) = 2^{E+3} \quad (2.31)$$

so that the fractional uncertainty is

$$f \equiv \frac{\Delta C}{C_{po}} = \frac{16(2^{E-1})}{16[2^E(M + 1/2)]} = \frac{1}{1 + 2M} \quad (2.32)$$

This gives the fractional uncertainty for any  $M$ . The maximum value of  $f$  occurs when  $E$  changes from one value to the next, at which point

$$M = 2^a \quad (2.33)$$

and

$$f_{max} = \frac{1}{2 + M_m} \quad (2.34)$$

with  $M_m$  given by (2.20). The minimum error occurs just before the change in  $E$ , where

$$M = M_m = 2^A - 1 \quad (2.35)$$

so that

$$f_{\min} = \frac{1}{1 + 2M_m} \quad (2.36)$$

Table 2.9 gives the characteristics of the compression counters. Since, as noted above, the ripple counter can be read exactly (the 16 cancels in the above for the fractional error), the fractional uncertainty is due only to that in the compression counters.

TABLE 2.9  
Compression Counter Characteristics

Counter Designation (M x E)	Maximum Indicated Count, $C_m$	Max Error $f_{\max}$	Min Error $f_{\min}$	Overflow Count, $C_o$
4x4	491520	$\pm 5.9\%$	$\pm 3.2\%$	524280
5x3	3968	$\pm 3.0\%$	$\pm 1.6\%$	4080

In summary, the max and min fractional errors apply to the counters using the indicated type compression, whether or not they are preceded by a ripple counter (that is read out). These errors apply to the most probable count  $C$  in (2.25). It is interesting to note, however, that once a dose counter overflows the fractional error in dose read actually decreases. This is because the overflow count is known exactly, and it is assumed that the number of overflows  $n$ , in Eq. (2.25), is also known. Hence, the count  $C$  in (2.25) does not indicate the total dose; and the error in  $C$  is less than that in  $C_p$ .

## 2.5 Calibration Data

The flight unit Dosimeter was extensively calibrated by use of protons from the Harvard Cyclotron, and electrons from the AFGL Linac. The 160 MeV proton beam at the Harvard cyclotron was passed through two beam-spreading absorbers to provide a maximum energy of 144 MeV at the Dosimeter. Additional absorbers were used to reduce the energy to as low as 17 MeV. Data were taken for incident directions (relative to the Dome plane normal) of from  $0^\circ$  to  $180^\circ$  (rear entry). A list of the data taken is given in Table 2.10.

The electron data taken at the AFGL Linac covered the range of 0.9 to 18.4 MeV. The nominal electron energies were calibrated against known gamma-ray energies with a 1 inch thick BGO crystal, so the corrected energies should be accurate to better than 5%. A list of the electron energy/angle combinations for which data were taken is given in Table 2.11.

The Dosimeter was also calibrated extensively using gamma-ray and beta sources, with this being the primary method of calibrating the dose channel responses (see Section 4). The electron and proton beam calibrations are primarily to verify proper unit operation, and to calibrate the flux channels in terms of the incident particle fluxes. A large amount of data were taken, but only a small portion has been partially reduced. During data acquisition the Dosimeter channel responses were checked to verify proper operation. The detailed analysis necessary to provide the final channel responses to electrons and protons was not done because of insufficient time.

Some preliminary analysis of the response of the D2 Dome to electrons has been made, with the results being given in Tables 2.12 and 2.13. The relative response at normal incidence is given in Table 2.12. The flux responses (protons and electrons) are calculated relative to one of the monitor detectors, and have been corrected for the Am-241 calibration source background. The relative response must still be corrected for the beam profile to obtain the effective detection area, but it is close to the  $1 \text{ cm}^2$  area of the solid state detector. The response is in agreement with the theoretical electron threshold of 2.5 MeV, with the proton channel having less than a few % sensitivity to electrons, even those above 10 MeV. The angular response of the D2 Dome for 8.5 MeV electrons is shown in Table 2.13. The response at  $90^\circ$  is still large, showing the effects of scattering by the aluminum dome. This is very similar to results in Ref 2.8, Fig. 2.

The relative response of the D3 Dome for protons at normal incidence is given in Table 2.14. The responses have been corrected only for the Am-241 source background, but the total effective area is near the  $1 \text{ cm}^2$  of the solid state detector. The response is in good agreement with the theoretical calculations, with the proton flux channel having maximum sensitivity for 52-70 MeV protons, and the electron flux channel having maximum sensitivity for  $> 70 \text{ MeV}$ . The proton energy losses for normal incidence in the D3 dome detector are given in Table 2.15. The measured and calculated energy losses are equal within a few percent. The general pattern of proton response calculated theoretically was verified for all Dome detectors. The detailed reduction of the data to actual geometric factors was not within the scope of work of the present contract.



Table 2.10

List of Calibration Data Taken for Protons  
at the Harvard Cyclotron

<u>Detector (Dome)</u>	<u>Angles (deg)</u>	<u>Proton energies (MeV)</u>
D1	0, 30, 60, 90	17, 25, 30, 38, 44, 51, 59, 66, 79, 111, 144
D1	60, 90	94
D1	120	111, 121, 133, 144
D1	150	133, 144
D1	180	121, 133, 144
D2	0, 30, 60, 90	32, 38, 44, 51, 59, 66, 79, 94, 121, 144
D2	0	28, 30
D2	120	84, 94, 111, 121, 133, 144
D2	150	121, 133, 144
D2	180	133, 144
D3	0, 30, 60, 90	44, 51, 59, 66, 79, 94, 121, 144
D3	120	111, 121, 133, 144
D3	150, 180	121, 144
D4	0, 30, 60, 90	79, 84, 94, 121, 144
D4	120	144
D4	150, 180	133, 144

Table 2.11

List of Calibration Data Taken for Electrons  
at the AFGL Linac

<u>Detector (Dome)</u>	<u>Angles (deg)</u>	<u>Electron energies - corrected (MeV)</u>
D1	0, 45, 90	0.9, 1.9, 2.9, 4.1, 6.1, 8.5
D1	0	10.5, 13.5, 18.4
D2	0, 30, 60, 90	8.5
D2	0, 45, 90	1.9, 2.9, 4.1, 5.1, 6.7, 8.5, 13.5
D3	0, 30, 60, 90	4.1, 5.1, 6.7, 8.5, 13.5
D3	120	8.5, 13.5
D4	0	6.7, 8.5, 10.5, 13.5, 18.4
D4	30, 60, 90, 120	10.5, 11.5, 13.5, 18.4

Table 2. 12

Relative Response of D2 Dome for Electrons  
at Normal Incidence

<u>Electron Energy (MeV)</u>	<u>Electron Flux Channel Relative Response</u>	<u>Proton Flux Channel Relative Response*</u>
2.9	0.32	0.003
4.1	0.50	-0.001
5.1	0.72	0.007
6.7	1.01	0.009
8.5	0.97	0.018
13.5	0.82	0.019

\*Background correction results in some negative responses due to statistical fluctuations.

Table 2. 13

Relative Angular Response of D2 Dome for 8.5 MeV Electrons

<u>Angle (deg)</u>	<u>Electron Flux Channel Relative Response</u>	<u>Proton Flux Channel Relative Response</u>
0	0.97	0.018
45	0.87	0.022
90	0.39	0.013

Table 2.14

Relative Response of D3 Dome for Protons  
at Normal Incidence

<u>Proton Energy (MeV)</u>	<u>Electron Flux Channel Relative Response*</u>	<u>Proton Flux Channel Relative Response*</u>
44	-0.004	-0.015
51	0.008	0.17
59	0.035	0.91
66	0.12	0.73
79	0.67	0.072
84	0.71	0.046
94	0.71	0.056
<u>144</u>	0.74	0.029

\*Background correction results in some negative response due to statistical fluctuations.

Table 2.15

Proton Energy Losses in the D3 Dome Detector  
at Normal Incidence

<u>Proton Energy (MeV)</u>	<u>Measured Energy Loss (MeV)</u>	<u>Calculated Energy Loss (MeV)*</u>	<u>Calculated Measured</u>
66	1.13	1.16	1.03
79	0.80	0.81	1.01
94	0.66	0.64	0.97
144	0.44	0.44	1.00

\*Taken from the appropriate curve for the 457 micron thick detector calculations and multiplied by 400/457 to get the approximate value for a 400 micron thick detector.

### 3. DOSIMETER GENERAL DESCRIPTION

#### 3.1 Physical Details

##### 3.1.1 Domes

The basic concept of measuring the effects of particles above energy thresholds established by shields has been employed for many years. The present instrument employs four such shield/detector assemblies, called domes for simplicity. The thickness of the hemispherical aluminum shields and the areas of the detectors are given in Table 3.1. The thicknesses are chosen to give the electron thresholds listed. The corresponding proton thresholds are also given. The detector areas are chosen to provide reasonable count rates for the anticipated radiation environment.

Table 3.1  
Dome Sensor Specifications

Dome #	Thickness inches	Detector model #	Detector Area cm <sup>2</sup>	Elec. Th. MeV	Proton Th. MeV
1	.0803	YAG-100	.051	1.0	20
2	.2263	YAG-444	1.000	2.5	35
3	.4453	YAG-444	1.000	5.0	51
4	.8628	YAG-444	1.000	10.0	75

Fig. 3.1 is a cross section view of Dome 1. It serves as a typical example, since the other domes vary only dimensionally. The dome shield can be removed by pulling it upwards after removing 3 allen head cap screws. This exposes the detector chip shown mounted to its carrier. The carrier (including the chip and Cal source) can now be carefully pulled upward. (The insertion force of the detector pins in the p.c. board mounted socket and any friction must be overcome without bending the assembly sideways.) This leaves only the tungsten back shield mounted to the instrument housing by three flat head screws.

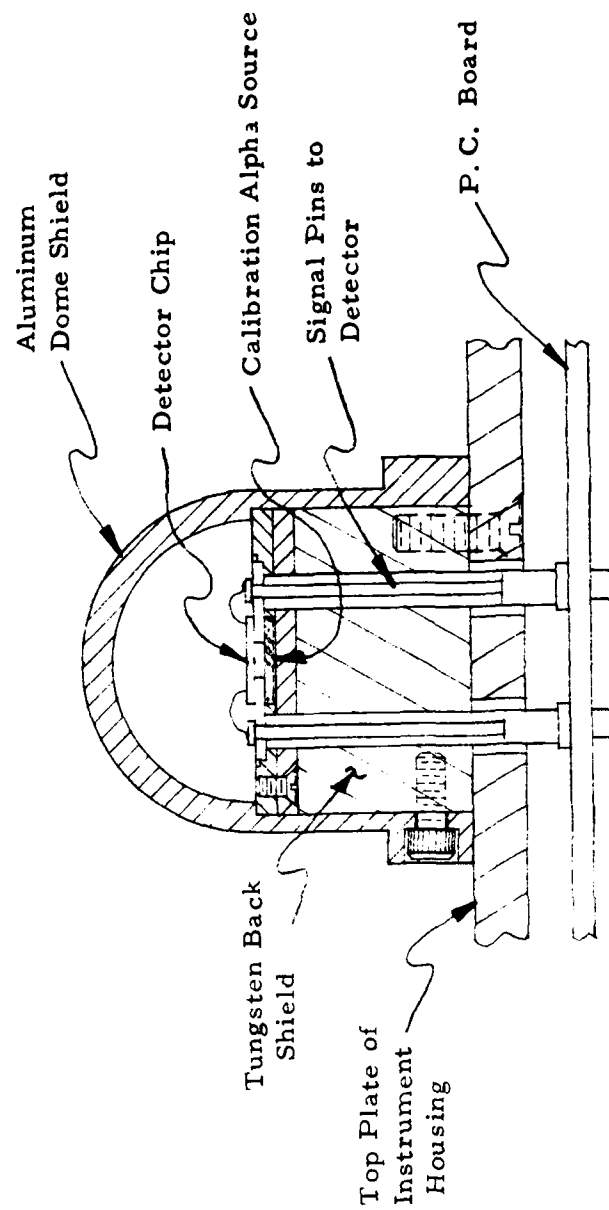


Figure 3.1 Cross Section View of Dome 1

In the upper left of Fig. 3.2 is EG & G's standard package. In the photo the front window has been removed and connections have been attached to the pins. This application does not require the type of heat sinking demanded by the device's usual application, a high power laser detector. Moreover, it is essential to have access to the back surface of the detector. This same device is shown mounted to Panametrics detector carrier in the upper right of the photo. At the lower right it is shown from the back with the Cal source and retaining plate removed. The metalized back of the detector and its ceramic substrate are visible in the center. The YAG-100 used in Dome 1 is mounted on a smaller carrier shown at lower left.

The Cal source ( $\approx 0.3$  nCi of  $\text{Am}^{241}$  with a thin aluminum moderator) irradiates the rear of the detector resulting in a known spectrum.  $\text{Am}^{241}$  emits alpha particles at several energies closely spaced around 5.5 MeV. The moderator spreads the spectrum and shifts the peak energy downward toward 3 MeV.

In use the instrument is placed in the Cal mode as the spacecraft passes through a "quiet" portion of its orbit, (see Section 4 for more detailed instructions). In this mode, the instrument sorts the energies into a 1-3 MeV lower range and a 3-10 MeV upper range, with the upper Cal flux approximately equal to the lower Cal flux. Any change in the depletion of the detector, in the amp or preamp gain or in the reference generator will shift the upper/lower flux ratio from its initial value. Note that if the external flux is comparable to or greater than the Cal flux, a valid calibration check cannot be performed.

### 3.1.2 Housing

The instrument housing functions as a radiation and electrical shield as well as being the primary structural member. The requirement to maintain the electronics radiation dose below  $10^5$  rads under conditions in which the total integrated dose is  $10^6$  rads results in a  $1 \text{ g/cm}^2$  surface density specification for the radiation shield. This spec defines the weight of the housing, but leaves one free to choose the material. Aluminum at .146" wall thickness is more rigid than the equivalent (thinner) plate of steel, since their moduli of elasticity are comparable.

The inherent structural integrity of the envelope eliminates any need for internal or external bracing. Likewise, the small size of the p.c. boards (4" x 4 1/2") ensures their rigidity. The large power supply components are epoxy-bonded to their p.c. boards or connected directly to the housing.

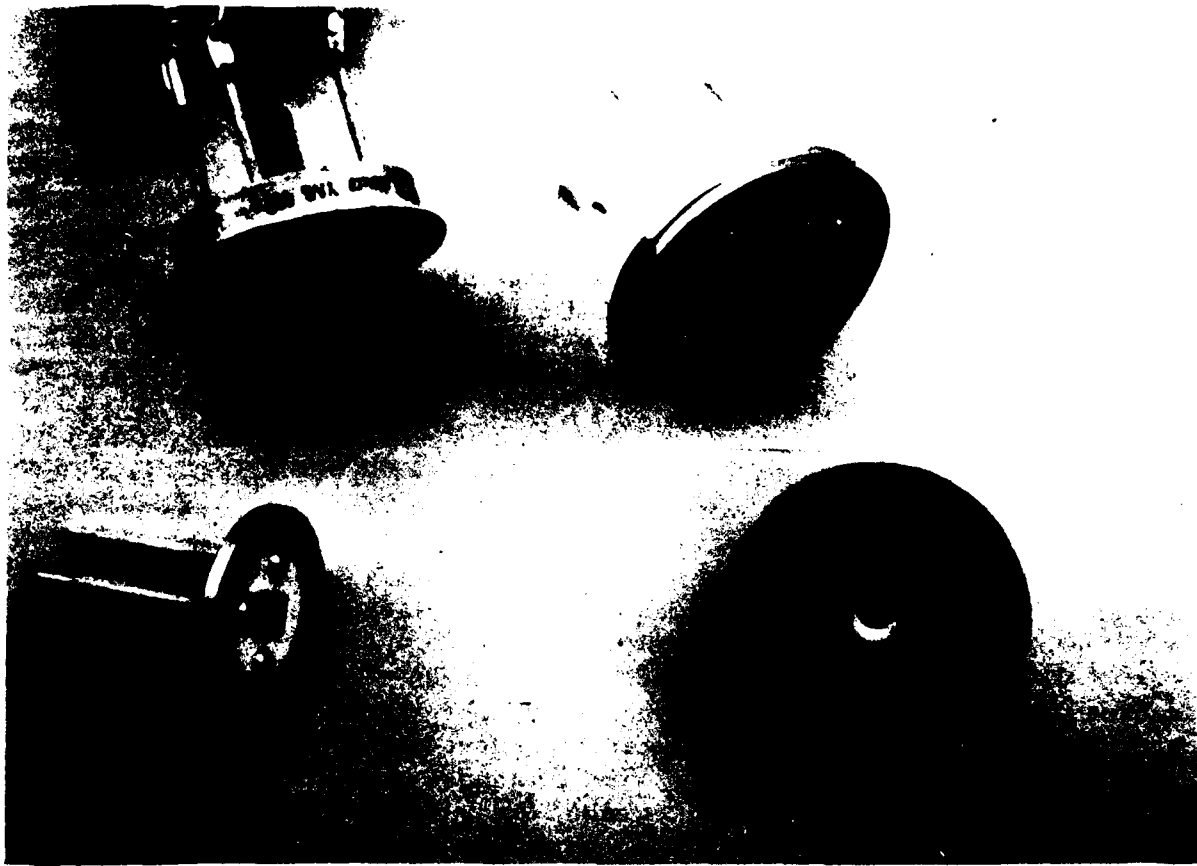


Figure 3.2. Detector Carrier Photo.



## 3.2 Electronics Design

### 3.2.1 Overall Instrument

Fig. 3.3 is the block diagram for the instrument. The four detectors, bias networks, and preamp subassemblies together constitute the detection assembly. With the exception of the DC-DC convertor, the remaining blocks are standard size p.c. board assemblies. The DC-DC convertor separates into 3 odd sized p.c. board assemblies, two power transistors with bracket, filter feedthrus, and EMI shields.

The assemblies shown are interconnected thru the backplane, as are the external connectors - with the exception of the preamp test inputs J13-J16. The diagram is cross referenced to the backplane node list Table 3.3 by node number and name. The table gives a signal description and specifies pin numbers. All interface lines are labeled in accordance with the interface control documents (Ref 2.3 and 2.4).

On the diagram data flows from top to bottom. The detected particle causes a charge proportional to the deposited energy to be injected into the preamps. The resultant outputs are analog pulses with the peak voltage proportional to the injected charge. The star pulse is much lower in amplitude so that saturation does not occur for particles which deposit less than 100 MeV energy. (The bipolar pulse saturates at about 10 MeV.)

The digitizer classifies the particle based on deposited energy and digitizer mode (Cal or normal). The energy windows and thresholds are listed in Table 3.2, with all energies in MeV.

Table 3.2

Digitizer Classification

	Norm				Cal			
	CH 1	CH 2	CH 3	CH 4	CH 1	CH 2	CH 3	CH 4
*n	$\geq 40$	$\geq 40$	$\geq 75$	$\geq 40$	$\geq 40$	$\geq 40$	$\geq 75$	$\geq 40$
Pn	1-10	1-10	1-10	1-10	3-10	3-10	3-10	3-10
En	.05-1	.05-1	.05-1	.05-1	1-3	1-3	1-3	1-3

If the classification is in the last two rows, the peak voltage is quantized to 16 levels. The  $\text{Dig}_n$  ( $n = 1, 2, 3, 4$ ) output is a 1 MHz pulse train. The number of pulses output corresponds alternately to the quantization level immediately above or below the pulse height. This alternation is necessary so that the averaged digitizer output match the average bin energy, which is taken to be the average of the quantization energies which bound the bin.

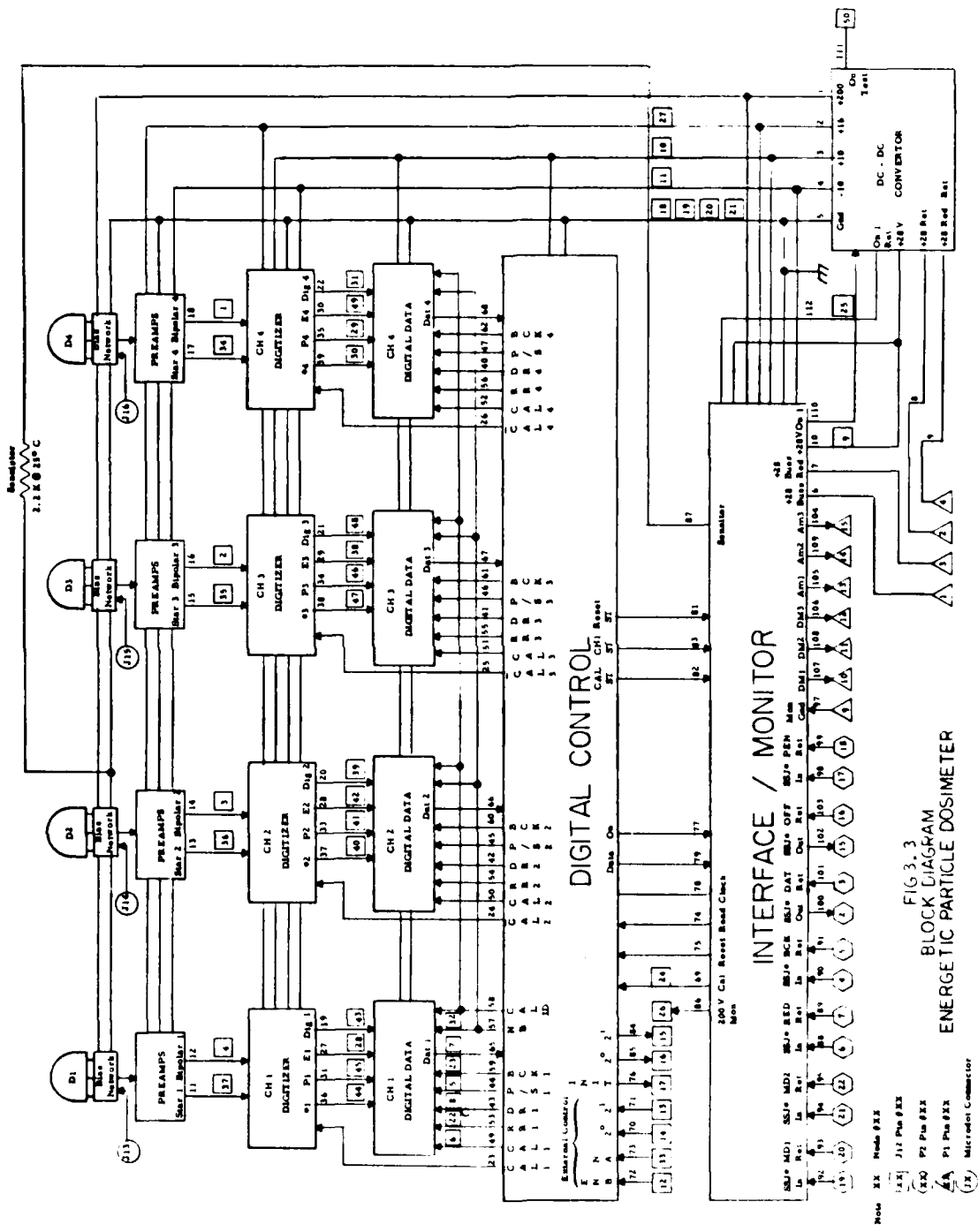


FIG 3.3  
BLOCK DIAGRAM  
ENERGY TIC PARTICLE DOSIMETER

Table 3.3

## SSJ\* DOSIMETER

## BACKPLANE NODE LIST

## CONNECTOR ASSIGNMENT

NAME	USE	KEY
J1	Detection Assembly	C3
J2	CH1 Digitizer Board	A1
J3	CH2 Digitizer Board	A2
J4	CH3 Digitizer Board	A3
J5	CH4 Digitizer Board	A4
J6	CH4 Digital Data Board	B4
J7	CH3 Digital Data Board	B3
J8	CH2 Digital Data Board	B2
J9	CH1 Digital Data Board	B1
J10	Digital Control Board	C1
J11	Interface/Monitor Board	D1
J12	Test Connector	None
P1	Power Connector	None
P2	OLS Interface Connector	None
PAD	Individual Connections; DC-DC Convertor	None
J13	CH1 Preamp Test Input	None
J14	CH2 Preamp Test Input	None
J15	CH3 Preamp Test Input	None
J16	CH4 Preamp Test Input	None

Table 3.3 (cont.)

NODE #	NAME	CONNECTIONS (Note: PAD NO. S ON DC-DC CONVERTOR)	DESCRIPTION
1	+200 V	J1-28, J11-11, Pad 5	Bias Supply
2	+16 V	J1-4, J2-4, J3-4, J4-4, J5-4, J11-4, J12-27, Pad 3	Pos. Analog Supply
3	+10	J2 thru J11, Pin 6, J12-10, Pad 1	Digital Supply
4	-10	J1-2, J2-2, J3-2, J4-2, J5-2, J11-2, J12-11, Pad 2	Neg. Analog Supply
5	GND	J1-3, 7, 11, 15, 19, 23, 27; J2-1, 3, 5, 7; J3-1, 3, 5, 7; J4-1, 3, 5, 7; J5-1, 3, 5, 7; J6-1 thru 7; J7-1 thru 7; J8-1 thru 7; J9-1 thru 7; J10-1, 3, 5, 7; J11-1, 3, 5, 7; J12-18, 19, 20, 21; P1-5, 6; Pad 4	Signal GND (Chassis)
6	+28 Buss	J11-14, P1-1	Primary Power
7	+28 Buss, Red	J11-15, P1-3	Redundant Power
8	+28 Ret	P1-2, Pad 10	Power Return
9	+28 Red Ret	P1-4, Pad 10	Redundant Return
10	+28 V	J11-16, J11-17, J12-9, Pad 6	+28 V (Fused)
11	Star 1	J1-21, J2-16, J12-37	CH1 Star Pulse
12	Bipolar 1	J1-1, J2-26, J12-4	CH1 Bipolar Pulse
13	Star 2	J1-25, J3-16, J12-36	CH2 Star Pulse
14	Bipolar 2	J1-13, J3-26, J12-3	CH2 Bipolar Pulse
15	Star 3	J1-17, J4-16, J12-35	CH3 Star Pulse
16	Bipolar 3	J1-5, J4-26, J12-2	CH3 Bipolar Pulse
17	Star 4	J1-29, J5-16, J12-34	CH4 Star Pulse
18	Bipolar 4	J1-9, J5-26, J12-1	CH4 Bipolar Pulse
19	Dig 1	J2-14, J9-26, J12-43	CH1 Dose Count
20	Dig 2	J3-14, J8-26, J12-39	CH2 Dose Count
21	Dig 3	J4-14, J7-26, J12-48	CH3 Dose Count
22	Dig 4	J5-14, J6-26, J12-31	CH4 Dose Count

Table 3.3 (cont.)

NODE #	NAME	CONNECTIONS	DESCRIPTION
23	Cal 1	J2-28, J10-53	CH1 Digitizer Mode
24	Cal 2	J3-28, J10-52	CH2 Digitizer Mode
25	Cal 3	J4-28, J10-51	CH3 Digitizer Mode
26	Cal 4	J5-28, J10-50	CH4 Digitizer Mode
27	E1	J2-24, J9-14, J12-28	CH1 Electron Count
28	E2	J3-24, J8-14, J12-42	CH2 Electron Count
29	E3	J4-24, J7-14, J12-38	CH3 Electron Count
30	E4	J5-24, J6-14, J12-49	CH4 Electron Count
31	P1	J2-22, J9-12, J12-45	CH1 Proton Count
32	Not Used		
33	P2	J3-22, J8-12, J12-41	CH2 Proton Count
34	P3	J4-22, J7-12, J12-46	CH3 Proton Count
35	P4	J5-22, J6-12, J12-29	CH4 Proton Count
36	*1	J2-12, J9-10, J12-44	CH1 Star Count
37	*2	J3-12, J8-10, J12-40	CH2 Star Count
38	*3	J4-12, J7-10, J12-47	CH3 Star Count
39	*4	J5-12, J6-10, J12-30	CH4 Star Count
40	DR4	J6-16, J10-43	CH4 Dose Reset
41	DR3	J7-16, J10-32	CH3 Dose Reset
42	DR2	J8-16, J10-44	CH2 Dose Reset
43	DR1	J9-16, J10-26, J12-8	CH1 Dose Reset
44	P/S1	J9-28, J10-31, J12-5	CH1 Data Load
45	P/S2	J8-28, J10-49	CH2 Data Load

Table 3.3 (cont.)

NODE #	NAME	CONNECTIONS	DESCRIPTION
46	P/S3	J7-28, J10-37	CH3 Data Load
47	P/S4	J6-28, J10-38	CH4 Data Load
48	Not Used		
49	Cal 1	J9-24, J10-29, J12-6	CH1 Data Select
50	Cal 2	J8-24, J10-47	CH2 Data Select
51	Cal 3	J7-24, J10-35	CH3 Data Select
52	Cal 4	J6-24, J10-40	CH4 Data Select
53	RR 1	J9-27, J10-30, J12-22	CH1 Read Reset
54	RR 2	J8-27, J10-48	CH2 Read Reset
55	RR 3	J7-27, J10-36	CH3 Read Reset
56	RR 4	J6-27, J10-39	CH4 Read Reset
57	NB	J6-20, 29; J7-20, 29; J8-20, 29; J9-20, 29; J10-22, J12-32	Normal Mode Control
58	Cal I.D.	J6-22, J7-22, J8-22, J9-22, J10-24	Cal Mode Marker
59	BCK 1	J9-23, J10-28, J12-23	CH1 Read Clock
60	BCK 2	J8-23, J10-46	CH2 Read Clock
61	BCK 3	J7-23, J10-34	CH3 Read Clock
62	BCK 4	J6-23, J10-41	CH4 Read Clock
63	Not Used		
64	Not Used		
65	DAT 1	J9-18, J10-27, J12-7	CH1 Serial Data
66	DAT 2	J8-18, J10-45	CH2 Serial Data
67	DAT 3	J7-18, J10-33	CH3 Serial Data
68	DAT 4	J6-18, J10-42	CH4 Serial Data
69	Cal	J10-19, J11-32, J12-24	Cal Mode Control

Table 3. 3 (cont.)

NODE #	NAME	CONNECTIONS	DESCRIPTION
70	2 <sup>0</sup> CCE	J10-14, J12-14	L. S. B. Ext. CH. Control
71	2 <sup>1</sup> CCE	J10-16, J12-13	M. S. B. Ext. CH. Control
72	Ext ENB	J10-18, J12-12	Ext. Control Enable
73	Ext NA	J10-20, J12-33	Ext. Normal Mode Control
74	Read	J10-13, J11-26	Read Gate (10 V CMOS)
75	Reset	J10-15, J11-28	Reset (10 V CMOS)
76	INIT	J10-8, J12-17	Initialize Pulse
77	ON	J10-11, J11-24	ON Indicator (10 V CMOS)
78	Clock	J10-17, J11-30	Read Clock (10 V CMOS)
79	DATA	J10-25, J11-38	Serial Data (10 V CMOS)
80	Not Used		
81	Reset ST	J10-9, J11-9	Reset Monitor
82	Cal ST	J10-21, J11-34	Cal Mode Monitor
83	CH1 ST	J10-23, J11-36	Channel Monitor
84	CH 21	J10-12, J12-15	M. S. B. Channel Code
85	CH 2 <sup>0</sup>	J10-10, J12-16	L. S. B. Channel Code
86	+200 V MON	J11-12, J12-26	Bias TEST Point
87	Sensistor	J1-22, J11-8	Temperature Sense
88	SSJ* RED	J11-44, P2-6	Read Gate
89	SSJ* RED Ret	J11-45, P2-7	5 V Differential
90	SSJ* BCK	J11-51, P2-4	Read Clock
91	SSJ* BGK Ret	J11-50, P2-5	5 V Differential
92	SSJ* MD1	J11-49, P2-19	Cal Mode Command
93	SSJ* MD1 Ret	J11-48, P2-20	5 V Differential

Table 3. 3 (cont.)

NODE #	NAME	CONNECTIONS (Note: PAD NO. 5 ON DC-DC CONVERTOR)	DESCRIPTION
94	SSJ* MD2	J11-46, P2-21	Reset Command
95	SSJ* MD2 Ret	J11-47, P2-22	5 V Differential
96	Not used		
97	MON GND	J11-25, P1-9	Monitor Datum
98	SSJ* PEN	J11-52, P2-17	Power Enable
99	SSJ* PEN Ret	J11-53, P2-18	5 V Differential
100	SSJ* DAT	J11-40, P2-2	Serial Data
101	SSJ* DAT Ret	J11-43, P2-3	5 V Differential
102	SSJ* OFF	J11-42, P2-15	ON Indicator
103	SSJ* OFF Ret	J11-41, P2-16	5 V Differential
104	AM 3	J11-29, P1-15	Temperature Monitor
105	AM 1	J11-27, P1-13	Bias Monitor
106	DM 3	J11-22, P1-12	5 V Reset Monitor
107	DM 1	J11-23, P1-10	5 V Cal Monitor
108	DM 2	J11-21, P1-11	5 V CH1 Monitor
109	AM 2	J11-20, P1-14	Power Monitor
110	ON 1	J11-37, Pad 8	Power Enable (Internal)
111	ON TEST	J12-50, Pad 9	ON Indicator (Internal)
112	ON 1 Ret	J11-18, 19; J12-25; Pad 7	+28 Ret (Filtered)



As a result, it is possible to define  $K_p$ , the number of digitizer pulses per peak voltage in the average. Although each particle is measured with a substantial quantization error, the average error approaches zero in the limit for any "reasonable" pulse height distribution. If one takes the product of  $K_p$  and  $K_v$  (the preamp conversion gain  $K_v = .97$  volts peak/MeV deposited) we get the digitizer pulse energy constant which specifies the number of digitizer pulses resulting from a given deposited energy. Table 3.4 lists  $K_p K_v$  for various particle and operating mode classifications.

Table 3.4  
Digitizer Pulse Energy Constant vs Mode

$K_p K_v$ (Pulses/MeV)		
	Norm	Cal
Pn	1.6	.533
En	16	5.333

The fluxes (\*n, Pn, En) are accumulated in 3 counters on the digital data board. The digitizer pulses are accumulated in one of four dose counters based on the particle classification (Pn or En) and current operating mode (Cal n). Table 3.5 lists the 7 registers, their type, usage and outputs.

Table 3.5  
Data Register Assignment

Name	Energy Range	Opp Mode	Counter Type	Size	Outputs
P Dose	P	Norm	Prescaled comp.	4 + 4 x 4	$p_1 p_2 p_3 p_4, m_1 m_2 m_3 m_4, e_1 e_2 e_3 e_4$
E Dose	E	Norm	Prescaled comp.	4 + 4 x 4	$p_1 p_2 p_3 p_4, m_1 m_2 m_3 m_4, e_1 e_2 e_3 e_4$
U Cal Dose	P	Cal	Binary	8	$p_1 p_2 p_3 p_4 p_5 p_6 p_7 p_8$
L Cal Dose	E	Cal	Binary	8	$p_1 p_2 p_3 p_4 p_5 p_6 p_7 p_8$
Star Flux	*	Any	Binary	5	$p_1 p_2 p_3 p_4 p_5$ (Norm), $p_1$ (Cal)
Upper Flux	P	Any	Compression	5 x 3	$m_1 m_2 m_3 m_4 m_5, e_1 e_2 e_3$
Lower Flux	E	Any	Compression	4 x 4	$m_1 m_2 m_3 m_4, e_1 e_2 e_3 e_4$

Line  $RR_n$  resets the flux and Cal Dose counters and  $DR_n$  resets the P and E Dose counters.

The Dose and Star Flux outputs are multiplexed into Normal A, Normal B, or Cal data based on the status of Caln and NB (See Table 3.6).

Table 3.6  
Data Address

NB	Cal n	Data Read
0	0	Normal A
1	0	Normal B
0	1	Cal
1	1	Cal

The data addressed together with the upper and lower fluxes and 3 identification bits (NB, CAL ID and CH 1 ID) are parallel loaded into a shift register in response to a pulse on P/S n. Table 3.7 lists the bit assignments for the three readout modes. In each case 36 bits are parallel loaded, then clocked out as NRZ serial data on each + transition of BCK n. The first identification bit is the status of NB. CAL ID is the second bit (the identifier is delayed one readout cycle, since the data read was accumulated during the previous cycle). The channel 1 identifier is implemented as a p. c. board option.

The digital control board generates the control signals described above for each of the four dosimeter channels from the spacecraft inputs or by external control from the test connector (J12). When power is first applied to the board INIT (Initialization pulse) is asserted and On goes high. This starts the channel and mode counter at CH 1 and NB. DR 1 is asserted immediately thus resetting the CH 1 dose counters and DR 2-4 follow on the succeeding readouts. A typical readout is as follows: The Clock (36 bits at  $\approx 10$  kHz) and its window (Read) are asserted. BCK n ( $n = 1, 2, 3, 4$  from Table 3.8) follows the clock. The channel number (n) changes state on the leading edge of Read, as do Cal n and Cal n if Cal ST has changed since the last CH n readout. After about 1 microsecond P/S n is pulsed, loading the data shift register. After another microsecond the LSB of the serial data appears on DAT n and Data. Simultaneously, RRn is pulsed (and DRn if Reset ST is asserted), and data begin to accumulate for the next readout. The second and succeeding data bits follow at  $\approx 100$  microsecond intervals. After 3.6 milliseconds the readout is complete and the channel number dwells at its current state until the next readout, about 1 second later.

TABLE 3.7

FIELD DESIGNATION  
IDENTIFICATION DATA

FIELD	# BITS	DESIGNATION	USE
1	1	Normal Mode Identification	1 for NORM B MODE 0 for NORM A MODE
2	1	Calibrate Mode Identification	1 for CAL MODE 0 otherwise
3	1	Channel (Dome) Identification	1 for CH 1 0 otherwise

NORM A DATA

FIELD	# BITS	DESIGNATION
4 A	4	Proton Dose Exponent
5 A	2	Proton Dose, $m_4$ , $m_3$
6 A	4	Electron Dose Exponent
7 A	2	Electron Dose, $m_4$ , $m_3$
8 A	5	Star Flux

NORM B DATA

4 B	2	Proton Dose, $m_2$ , $m_1$
5 B	4	Proton Dose Ripple Ctr.
6 B	2	Electron Dose, $m_2$ , $m_1$
7 B	4	Electron Dose Ripple Ctr.
8 B	5	Star Flux

CAL DATA

4 C	8	Upper CAL Dose
5 C	8	Lower CAL Dose
6 C	1	Star Flux

BASIC FLUX DATA

9	8	Upper Flux(CAL), pflux(NORM)
10	8	Lower Flux(CAL), cflux(NORM)

Table 3.8

Channel Code vs Channel Number

$2^0$	$2^1$	n
0	0	1
1	0	2
0	1	3
1	1	4

In the normal mode (Cal is zero) the operating mode follows a 64 readout cycle in which 60 NB readouts are followed by 4 NA readouts, resulting in 15 NB and 1 NA readout for each channel. Table 3.9 shows this cycle starting from power enable at T1. Note that external control allows choice of data mode on an arbitrary basis; and that internal control continues to index on each readout so that return is to the current channel and operating mode. The Cal and Reset commands are also exercised to show the synchronous operation and to document the operation of the digital monitors. CAL ID (not listed) lags CAL ST by four readouts.

The spacecraft commands originate in the Operational Linescan System (OLS) and enter the Dosimeter via P2. The Interface/Monitor Board converts these 5 V isolated differential bilevel signals to 10 V chassis referenced CMOS signals. SSJ\* MD1, SSJ\* MD2, SSJ\* RED, SSJ\* BCK and SSJ\* DAT correspond to Cal, Reset, Read, Clock, and Data, respectively.

SSJ\* PEN is the power enable command. On 1 follows the + transition of SSJ\* PEN as should On Test. If the input voltage (+28 V with respect to On 1 Ret) is not in excess of  $31 \pm .5$  V the convertor will be enabled. When On goes high (as a result of +10 V being applied to the digital control board) SSJ\* OFF follows it, confirming power up. On power down SSJ\* OFF follows SSJ\* PEN without delay. However, On 1 is delayed to ensure that the OLS will have adequate time to respond before the power supply decays.

The primary power is applied to PIN 1 and/or 3 of P1 and is routed to the Interface/Monitor board. Here the power lines are combined and fused (two 1.5A in parallel). The power (+28 V) is then routed to the DC-DC convertor and returned via PINS 2 and/or 4. +28 V is used directly for the SSJ\* PEN receiver, the power enable logic, and to maintain the standby states of SSJ\* OFF and SSJ\* DAT. This power is returned through On 1 Ret to a filter choke and thence to +28 Ret.

The Interface/Monitor board also contains the housekeeping monitors for the instrument. Mon Gnd is a high impedance input intended to sense the monitor reference voltage ( $V_{mon}$ ) at the receiver (presumably at or near

Table 3.7

Command, Monitor and Data Sequence

T	External Control				Commands		Digital Monitors			Data Mode	
	ENB	NA	2 <sup>1</sup>	2 <sup>0</sup>	Cal	Reset	CAL ST	Reset ST	CH 1 ST	CH-	Trig
1	1	x	x	x	0	0	0	1	1	1	NB
2	1	x	x	x	0	0	0	1	0	2	NB
3	1	x	x	x	0	0	0	1	0	3	NB
4	1	x	x	x	0	0	0	1	0	4	NB
5	1	x	x	x	0	0	0	0	1	1	NB
6	1	x	x	x	0	0	0	0	0	2	NB
7	1	x	x	x	0	0	0	0	0	3	NB
8	1	x	x	x	0	0	0	0	0	4	NB
9	1	x	x	x	0	0	0	0	1	1	NB
10	1	x	x	x	0	0	0	0	0	2	NB
11	0	0	0	0	0	0	0	0	1	1	NB
12	0	0	0	1	0	0	0	0	0	2	NB
13	0	1	1	0	0	0	0	0	0		NA
14	0	1	1	1	0	0	0	0	0	4	NA
15	1	x	x	x	0	0	0	0	0	3	NB
16	1	x	x	x	0	0	0	0	0	4	NB
17	1	x	x	x	0	0	0	0	1	1	NB
18	1	x	x	x	1	0	0	0	0	2	NB
19	1	x	x	x	1	0	0	0	0	3	NB
20	1	x	x	x	1	0	0	0	0	4	NB

Table 3.9 (continued)

T	External Control				Commands		Digital Monitors			Data Mode	
	ENB	NA	2 <sup>1</sup>	2 <sup>0</sup>	Cal	Reset	CAL ST	Reset ST	CH 1 ST	CH#	Type
21	1	x	x	x	1	0	1	0	1	1	Cal
22	1	x	x	x	1	0	1	0	0	2	Cal
23	1	x	x	x	1	0	1	0	0	3	Cal
24	1	x	x	x	1	0	1	0	0	4	Cal
25	1	x	x	x	1	0	1	0	1	1	Cal
26	1	x	x	x	1	0	1	0	0	2	Cal
27	1	x	x	x	1	0	1	0	0	3	Cal
28	0	0	1	0	1	0	1	0	0	3	Cal
29	0	1	0	0	1	0	1	0	1	1	Cal
30	0	0	0	0	1	0	1	0	1	1	Cal
31	1	x	x	x	0	0	1	0	0	3	Cal
32	1	x	x	x	0	0	1	0	0	4	Cal
33	1	x	x	x	0	0	0	0	1	1	NB
34	1	x	x	x	0	0	0	0	0	2	NB
35	1	x	x	x	0	1	0	0	0	3	NB
36	1	x	x	x	0	0	0	0	0	4	NB
37	1	x	x	x	0	0	0	1	1	1	NB
38	1	x	x	x	0	0	0	1	0	2	NB
39	1	x	x	x	0	0	0	1	0	3	NB
40	1	x	x	x	0	0	0	1	0	4	NB
41	1	x	x	x	0	0	0	0	1	1	NB
42	1	x	x	x	0	0	0	0	0	2	NB
43	1	x	x	x	0	0	0	0	0	3	NB
44	1	x	x	x	0	0	0	0	0	4	NB
45	1	x	x	x	0	0	0	0	1	1	NB

Table 3.9 (continued)

T	External Control				Commands		Digital Monitors			Data Mode	
	ENB	NA	2 <sup>1</sup>	2 <sup>0</sup>	Cal	Reset	CAL ST	Reset ST	CH 1 ST	CH#	Type
46	1	x	x	x	0	0	0	0	0	2	NB
47	1	x	x	x	0	0	0	0	0	3	NB
48	1	x	x	x	0	0	0	0	0	4	NB
49	1	x	x	x	0	0	0	0	1	1	NB
50	1	x	x	x	0	0	0	0	0	2	NB
51	1	x	x	x	0	0	0	0	0	3	NB
52	1	x	x	x	0	0	0	0	0	4	NB
53	1	x	x	x	0	0	0	0	1	1	NB
54	1	x	x	x	0	0	0	0	0	2	NB
55	1	x	x	x	0	0	0	0	0	3	NB
56	1	x	x	x	0	0	0	0	0	4	NB
57	1	x	x	x	0	0	0	0	1	1	NB
58	1	x	x	x	0	0	0	0	0	2	NB
59	1	x	x	x	0	0	0	0	0	3	NB
60	1	x	x	x	0	0	0	0	0	4	NB
61	1	x	x	x	0	0	0	0	1	1	NA
62	1	x	x	x	0	0	0	0	0	2	NA
63	1	x	x	x	0	0	0	0	0	3	NA
64	1	x	x	x	0	0	0	0	0	4	NA
65	1	x	x	x	0	0	0	0	1	1	NB
66	1	x	x	x	0	0	0	0	0	2	NB
67	1	x	x	x	0	0	0	0	0	3	NB

spacecraft ground). DM 1, 2 and 3 are bilevel outputs corresponding to CAL ST, CH 1 ST and Reset ST, respectively. Output levels are as follows:

Logic 0	"False"	$V_{mon} + 5 V$
Logic 1	"True"	$V_{mon}$

Am 1 and Am 3 are analog signals also referenced to Mon Gnd. Am 1 is 1/100 the 200 V bias supply and is nominally 2 volts. Am 3 is twice the voltage across the sensistor mounted on the detection assembly. The test current is 0.5 mA. Fig. 4.1 shows typical output voltages as a function of temperature. Am 2, the power monitor is nominally about 2.4 V with respect to the chasis. The 200 V Mon output is a test point isolated from +200 V by a 10 Megohm resistor.

### 3.2.2 Detection Assembly

Fig. 3.4 shows one of four identical detection channels. (Differences in detector type and dome thickness are treated in Section 3.1.1.) The solid state detector is of the guard ring type, a planar P-N junction with two concentric electrodes on one face and a common electrode on the other. In the EG & G YAG series devices used, the common electrode (terminal C) is on the P side. As a result it is convenient to model the device as two diodes. Terminal G, the outer ring forms the cathode of the guard diode and terminal A, the inner ring, forms the cathode of the active diode. With the common anodes (terminal C) grounded and a positive bias applied to terminal G as shown both diodes are reverse biased. The bulk of the leakage current flows through the guard diode or around it as surface leakage. The active diode is biased through the channel resistance  $R_{ch}$ , (the real part of the impedance of the channel formed between the inner and outer rings, typically 1 megohm). Since the dark current of the inner (active) diode is due only to bulk effects, the detector exhibits much lower current noise than would be obtainable with a conventional detector.

Terminal G is decoupled from the bias supply by a .01 MFD capacitor to ground and 100 K in series with the supply. This shunts guard diode noise currents to ground and prevents any individual detector from shorting out the bias supply. As a result, three data channels will give valid data, even with a completely shorted detector, without substantially increasing input power.

Amplifier A1 together with its feedback impedance (1 PF in parallel with 1000 Meg) constitutes the charge preamp. At the frequency of interest ( $f = 318 \text{ KHz}$ ,  $T = .5 \text{ microsecond}$ ) the capacitor is dominant ( $|Z_f| = .5 \text{ megohm}$  compared to  $R_f = 1000 \text{ megohm}$ ). So the circuit topology is that of a current integrator i.e.,  $V_o = K \int i_{in} \text{ or } V_o = K Q_{in}$ . In response to a short ( $< 10 \text{ nanosecond}$ ) current pulse out of the input node, it outputs a voltage





step proportional to the injected charge. Between events the output decays exponentially back toward the amplifier's quiescent bias point. The amplifier is constructed of discrete components and employs a J FET input stage to minimize noise.

The input charge pulses can originate in the detector, (each particle couples a charge of about .05 pico Coulombs for each MeV of energy deposited in the detector, through the .001 MFD DC blocking capacitor to the input) or from the test input. The test signal is typically a negative-going step followed by an exponential return to zero. The injected charge can be calculated from the step voltage ( $V_s$ ) and the value of the test capacitor ( $C_T = 1.5$  PF) by  $Q_{inj} = C_T V_s$ . So a step of .033 volts is required to simulate a particle which deposits 1 MeV of energy. The test input is terminated in 50  $\Omega$  to match the cable impedance.

The other three stages are tuned amplifiers with a center frequency of 318 KHz and 6 dB/octave slopes. A2 is fabricated from discrete components whereas A3 and A4 are integrated opamps. The T attenuator on the input to A3 is used to set the conversion gain of the Bipolar output. The resistors are selected to obtain a 5 K input impedance (which together with the 100 PF input capacitor determines the Hi pass frequency), and the proper attenuation.

The Bipolar output is a positive-going pulse which rises to its maximum after about .6 microsecond, crosses zero at 1.5 microsecond, reaches its negative peak (about half the positive peak) at about 2.5 microsecond and then returns to zero. The 500 K resistor shunting A2's input capacitor is called the pole-zero cancellation adjustment. It is set to assure that the Bipolar output does not overshoot on its return to zero. The Star Pulse goes negative, overshoots zero on its return and then settles. Since Star events are comparatively rare, pulse shape is not critical.

### 3.2.3 Digitizer Board

Figure 3.5 illustrates the digitizer elements. It receives two analog pulses from the detection assembly. Cal n is a digital control input;  $\phi_n$ , Pn En and Dig n are digital outputs; and Vs, Vr and Vp are DC reference voltages derived internally from the power supplies. Vr is the output of a silicon band-gap regulator, and Vp is divided down from it.

The Star Pulse is compared to Vs (adjusted to give the proper energy threshold). If Star n exceeds Vs, a digital level is output at  $\phi_n$ . In order to ensure adequate pulse width at  $\phi_n$  in the case where the peak Star n barely exceeds Vs, hysteresis is designed into the comparator.

AD-A113 085

PANAMETRICS INC WALTHAM MASS

F/8 9/3

DESIGN, FABRICATION, CALIBRATION, TESTING AND SATELLITE INTEGRA--ETC(U)

DEC 81 B SELLERS, R KELLIHER, F A HANSER

F19628-78-C-0247

UNCLASSIFIED

AFGL-TR-81-0354

NL

2 of 2

AD-A  
115580

END

DATE

FILED

04-82

DTIC

1.0

2.8

2.5

3.2

2.2

3.6

2.0

4.0

1.8

1.1

1.25

1.4

1.6

NIH Publication No. 80-1-100-10000  
U.S. GOVERNMENT PRINTING OFFICE

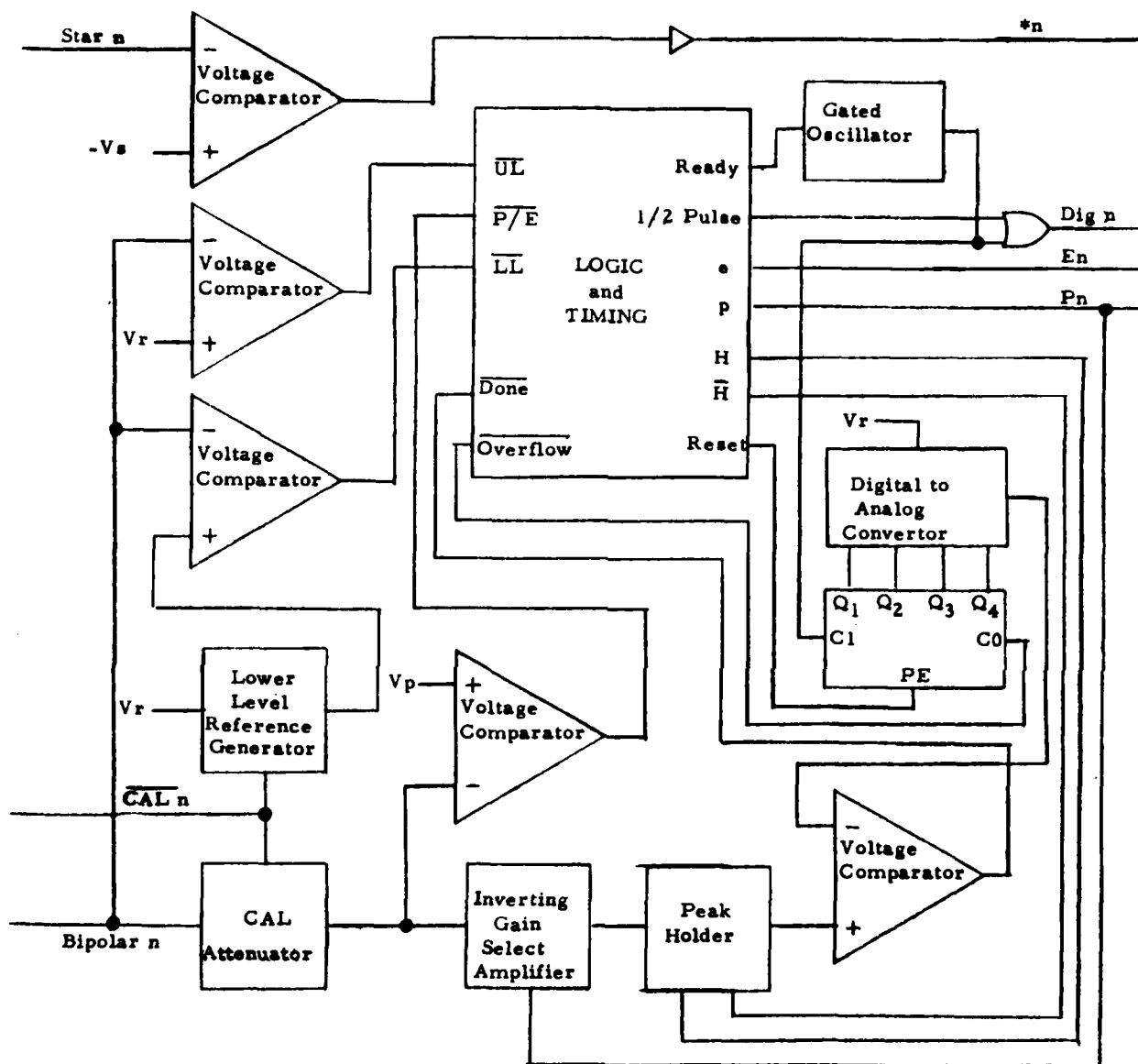


FIG. 3. 5 DIGITIZER BOARD BLOCK DIAGRAM

The remaining circuitry is driven by Bipolar  $n$  with control input Cal  $n$  modifying the gain and noise threshold. Operation is as follows: as the Bipolar pulse rises to its positive peak, the Lower Level (LL), the Proton/Electron Level (P/E) or the Upper Level (UL) may be exceeded based on the pulse amplitude. (These three comparators also employ hysteresis to assure minimum pulse width.) Bipolar pulses which do not exceed the Lower Level are ignored. If the Upper Level is exceeded, the logic will reset itself and no output results.

If, however, the amplitude is greater than the Lower threshold and less than the Upper threshold; the event will be analyzed. About 1 microsecond after the Lower threshold crossing H (Hold) goes high simultaneously with either e or p. (At this time the positive peak has passed and the negative peak is still at least a microsecond away.) The result will be p if the pulse exceeded the P/E Level otherwise e. These results are output as flux counts (P $n$  or E $n$ ). p is also used to shift the inverting amplifier gain down by a factor of 10. Since H is high (and  $\bar{H}$  low) the peak holder is now set to follow the negative-going slope of Bipolar  $n$  and then hold the peak negative value.

Note that the output of the peak holder is positive, since an inverting amplifier is used. The Cal attenuator together with the gain select amplifier provide four different gain combinations resulting in the digitizer pulse energy constants listed in Table 3.4. Note also that since the P/E discriminator is downstream of the Cal attenuator, the P/E energy threshold shifts with Cal  $n$ .

Every other time H goes high a pulse is output from 1/2 Pulse after 1/2 microsecond delay. This pulse, if present, is also the first pulse of the Dig  $n$  pulse train. At 8 microseconds past the +LL transition digitization begins. If Done is low (this is the case whenever the output of the peak holder ( $V_H$ ) is less than 1/16  $V_r$ , since the counter is preset to state 1 at this time), the logic resets itself to await the next event. Otherwise ready goes high and the gated oscillator outputs a 1 MHz square wave. Each positive transition of the oscillator increments the counter, resulting in a staircase waveform from the digital to analog convertor. When the staircase voltage exceeds  $V_H$ , Done goes low, ready follows it and the oscillator is disabled. In the unique case that  $V_p$  exceeds 15/16  $V_r$ , the oscillator is disabled by overflow after 15 counts. The oscillator pulse train with the addition of the half pulse described above forms the Dig  $n$  output. Within 500 nanoseconds after the last pulse of Dig  $n$  the logic is reset and e or p goes low.

Fig. 3.6 shows the digitizer timing for four events with the instrument in normal mode. The first event is processed and classified as a proton which deposited  $5.5/1.6 = 3.44$  MeV energy. The next event exceeds the Upper Level and is rejected. Note that the Bipolar Pulse saturates and therefore cannot distinguish events above 10 MeV. The third event is

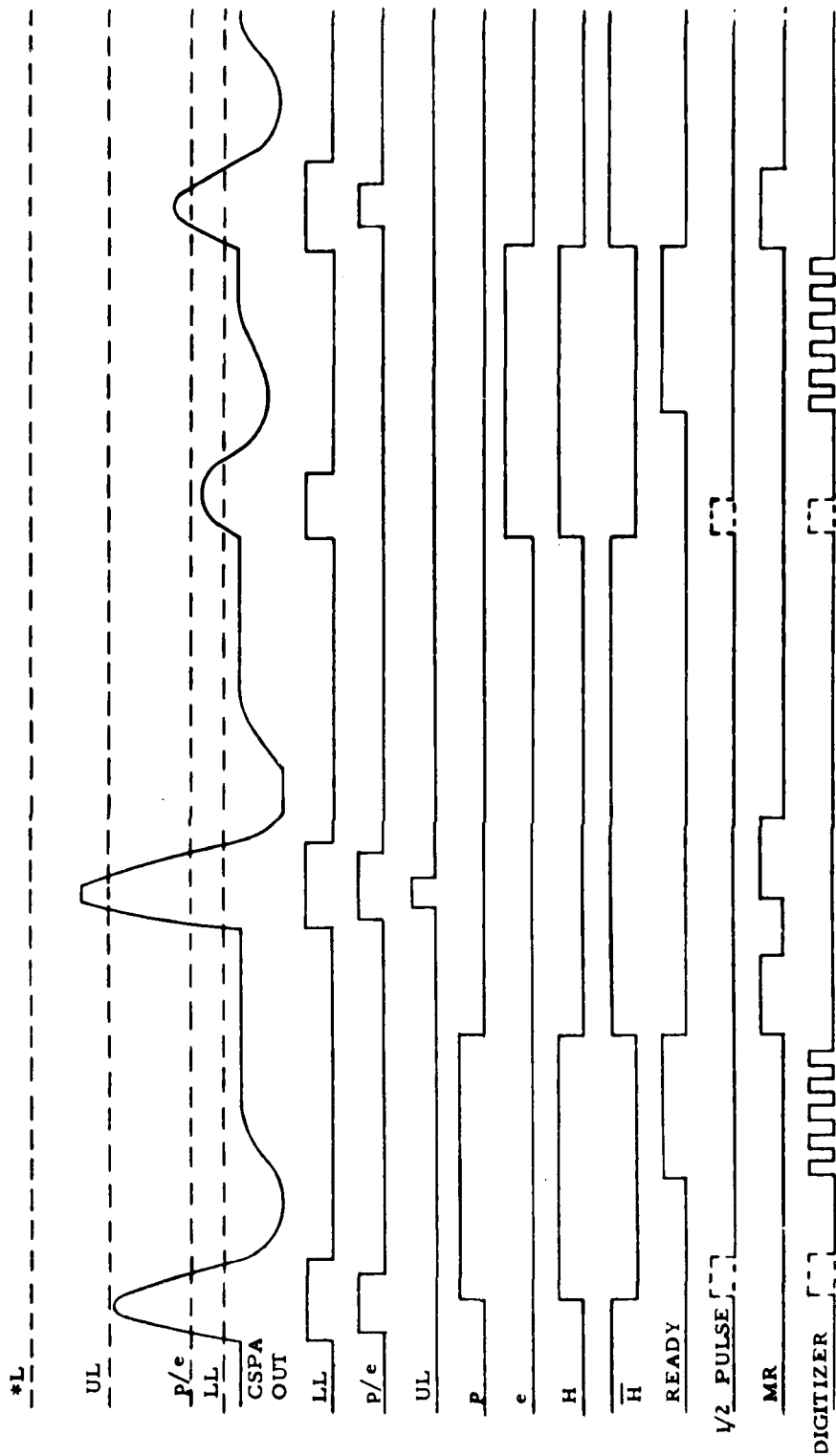


Figure 3.6 Digitizer Timing Diagram

classified as an electron with  $6.5/16 = .406$  MeV deposited energy. The last event occurs during the dead time while event 3 is being processed; consequently, it is ignored.

### 3.2.4 Digital Data Board

Fig. 3.7 is the block diagram for the Digital Data Board. Dign, En, Pn and \*n are data inputs from the Digitizer. CAL ID and NB are mode identification inputs. NB is also used as a control input. The other controls are Cal n, P/S n, BCK n, RRn, and DRn. Data is output serially from Dat n.

When P/S n is low the flux data (En, Pn and \*n) are accumulated in their respective counters. Dign is multiplexed into one of four counters based on the status of Pn and CAL n. Note that these are the same parameters (except for the polarity of CAL) which control the Digitizer mode. All data inputs are disabled when P/S n is high so that the counter outputs do not change state. RRn resets the flux counters and the CAL dose counters while DRn resets the Normal dose counters.

Note that different counter types are used in order to accommodate the different event rates for electrons, protons, stars and CAL source events and also the reset frequency. (RRn is exercised every four seconds whereas DRn is in response to a ground command which may not be issued for many months.) The convention  $N_m \times N_e$  compression means the count is encoded as a binary mantissa of  $N_m$  bits, and a binary exponent of  $N_e$  bits. For instance a  $5 \times 3$  compression counter has eight output bits as below:

$$e_3 \ e_2 \ e_1 \ m_5 \ m_4 \ m_3 \ m_2 \ m_1$$

The mantissa and exponent are interpreted conventionally:

$$M = m_1 + 2m_2 + 4m_3 + 8m_4 + 16m_5$$

$$\text{and } E = e_1 + 2e_2 + 4e_3$$

The minimum number of input counts required to cause a given output is:

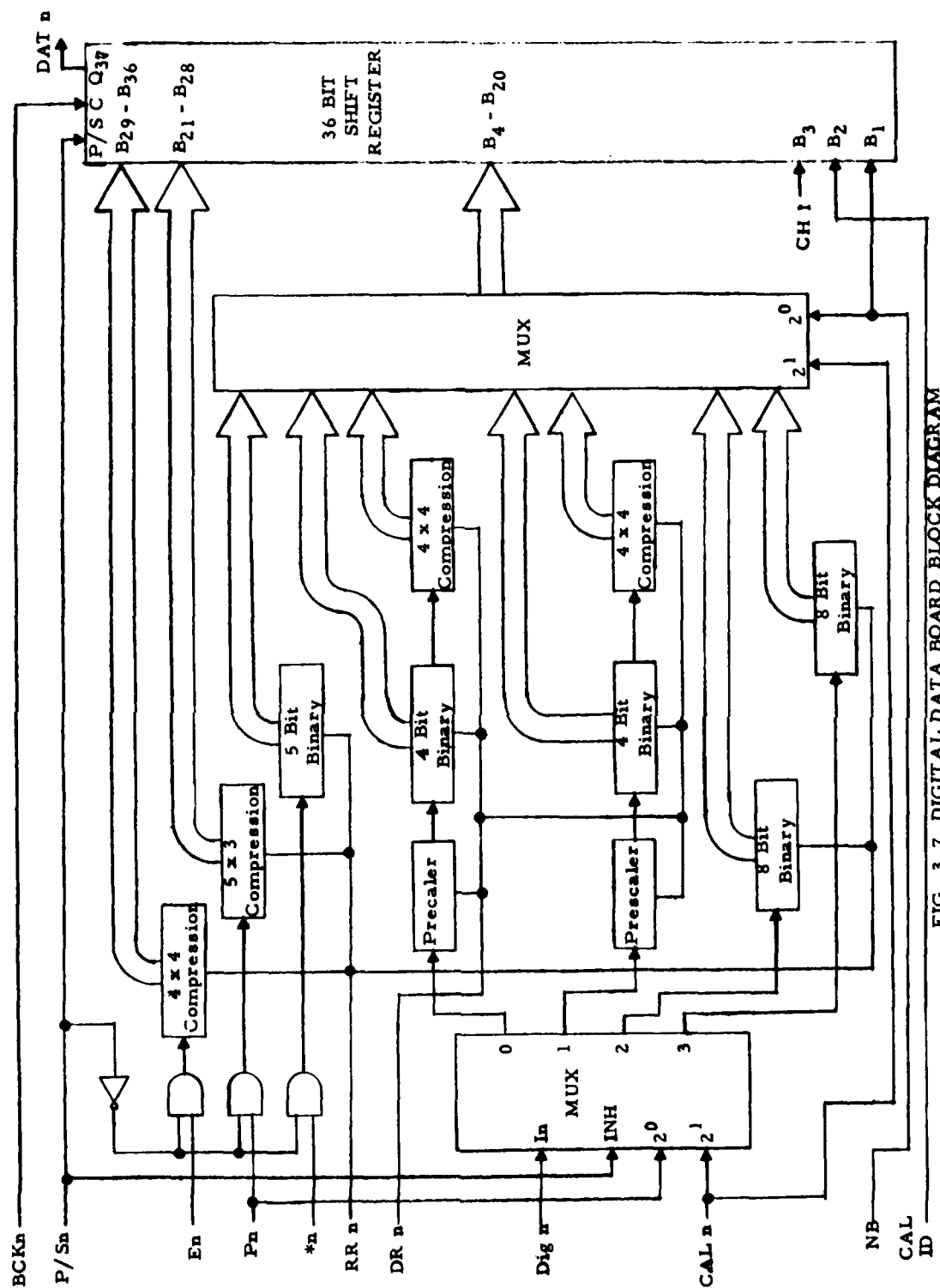
$$C_{\min} = M \times 2^E$$

and the maximum is:

$$C_{\max} = [(M + 1) \times 2^E] - 1$$

Iff  $E = 0$  then  $C_{\min} = C_{\max}$  and there is no uncertainty. As the counts approach infinity in the limit  $C = [M \times 2^E] + 2^E$  or  $C = [(M + 1/2) \times 2^E] + 2^{(E-1)}$





This same result is obtained for  $\frac{C_p}{K_c}$  when the compression counter is preceded by a binary prescaler of infinite stages, and where  $C_p$  is the number of counts at the prescaler input, and where  $K_c = 2^s$ ,  $s$  being the number of stages in the prescaler. (Each stage divides by two.)

In comparison to a conventional binary counter with the same number of output bits, a compression counter covers greater range at the expense of some decrease in accuracy. Fig. 3.8 shows how the compression algorithm is implemented. The first 8 counts are steered through  $Q_1$  of the Input Counter and Channel 0 of the Multiplexer to the Output Counter. On the eighth count  $m_4$  is latched, and the Output Counter is reset to zero. After another 8 input counts (16 total)  $e_1$  goes high. This steps the Multiplexer to  $Q_2$  of the Input Counter, causing the Output Counter to count by two's. Thereafter the mantissa cycles from state 8 to state 15, incrementing the exponent and dividing the count rate by two at each transition from state 15 to state 8. When the counter is full,  $Q_7$  of the Output Counter causes overflow to state 0.

The Output Multiplexer selects the appropriate counter outputs based on the status of NB and Cal n as in Table 3.6. As a result the shift register parallel inputs will conform to one of the three conventions given in Table 3.7. The Channel Identifier,  $B_3$  is connected by jumper to +10 V (Logic 1) on the Channel 1 Data Board. Channels 2, 3 and 4 are connected to ground (Logic 0).

Readout is as follows: P/S goes high and  $Q_1 - Q_{36}$  of the shift register are latched to the state of inputs  $B_1 - B_{36}$  respectively, while the inputs are inhibited. As P/S n goes low BCK n starts its first positive transition. As a result the shift register (now in its serial mode) shifts, and  $Q_{37}$  (the Dat n output) acquires or retains the state loaded at  $B_{36}$ . Simultaneously, RRn (and DRn, if the mode 2 (reset) command is being implemented) is exercised. BCKn is a 36 count 10 KHz square pulse train. As a result the remaining 35 bits are shifted out of Dat n at 100 microsecond intervals.

### 3.2.5 Digital Control Board

The Digital Control Board, Fig. 3.9, generates the control signals for the four data channels from the spacecraft or external control signals. The external control inputs have 10 K pull-up resistors (not shown) to +10 V so an open collector or open drain buffer is required to drive them. Control is exercised by pulling ENB down. The other controls are then active. An open input (+10) is logic "1" or true. As can be seen in Fig. 3.9, ENB is the control input to three DPST transmission gates. The channel code and the normal mode control lines connect either to external inputs or to the internal readout counter.



Figure 3.8 4 x 4 Compression Counter

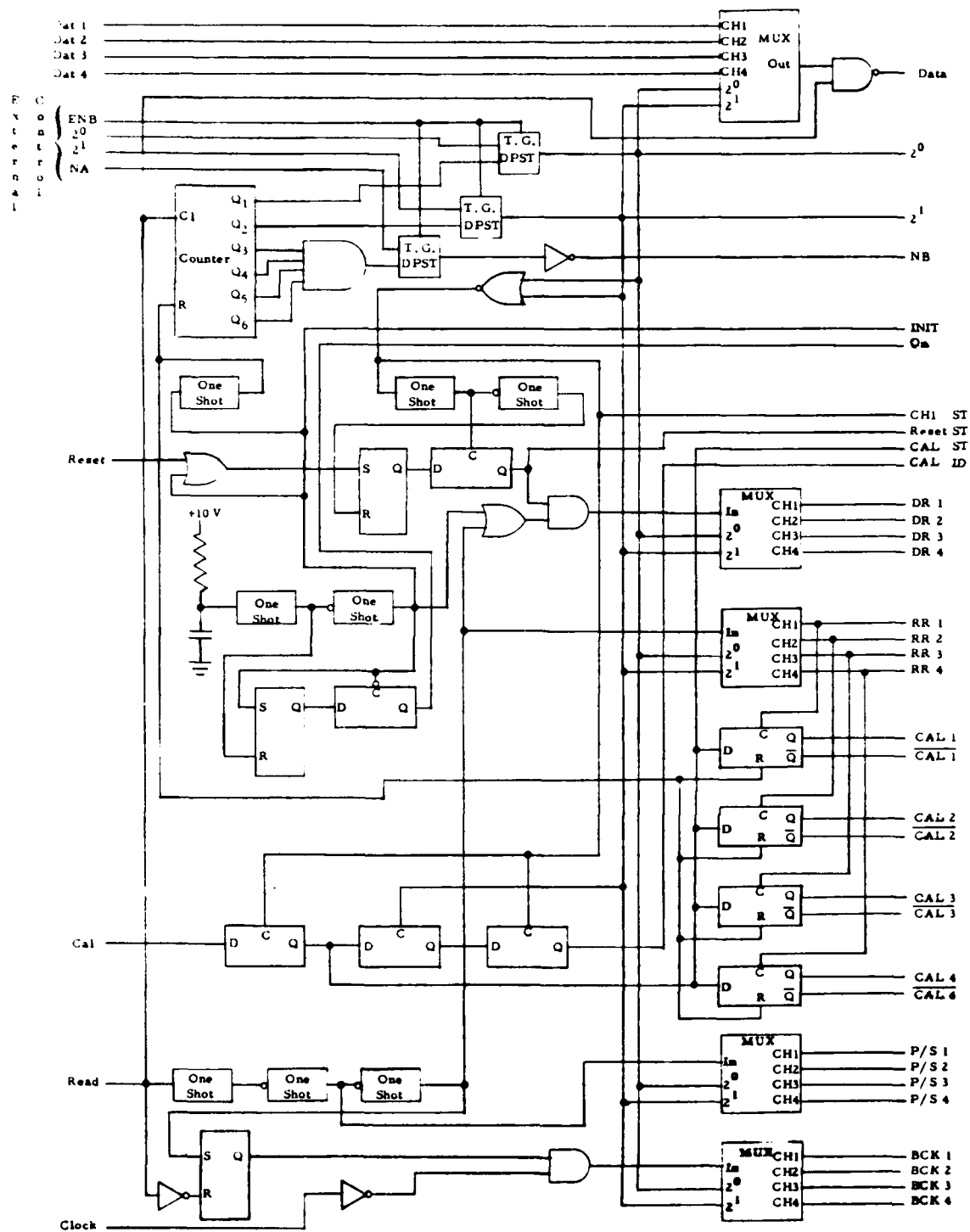


Fig. 3.9 Digital Control Board Block Diagram

Normally the channel and mode control signals NB,  $2^0$ , and  $2^1$  (NA = NB) follows the 64 readout cycle shown in Table 3.9. Each read command clocks the 6 bit Readout Counter to the next state. The two LSB's generate the Channel Code which controls the Channel Multiplexers. A NOR gate decodes state 0 of the code to serve as a trigger to synchronize the initiation of the Cal and Reset commands with channel 1. This signal is also output as CH 1 ST, the channel 1 monitor. An AND gate connected to Q3, Q4, Q5 and Q6 outputs a "1" during states 60-63 of the Readout Counter. This signal is inverted to become the NB (normal mode) control.

The read command also triggers a chain of one shots. The initial delay allows the channel and mode multiplexers to settle after their control inputs are updated as described above. The second one shot generates RRn where n is the channel number corresponding to the current channel code as in Table 3.8. The last one shot generates RRn (and also DRn if Reset ST is set). Simultaneously, BCK n is enabled.

BCK n clocks serial data into Dat n from Digital Data Board n. If the Read signal is high (the usual case), the Digital Control Board data output is the inverse of Dat n. After the last data bit ( $B_1$ ), Read goes low and BCK n is disabled.

The calibration mode is implemented as follows: the Cal input goes high in response to a Mode 1 command from the spacecraft. CAL ST is set on the first CH 1 readout following the command. CAL 1 and CAL 1 are triggered by RR1, placing digitizer #1 and digital data board #1 in the calibration mode. CAL 2 and CAL 2 follow on the next readout. As channel 3 is readout the state of CAL ST is latched into a storage register. CAL 3 and CAL 3 are asserted at this time, and CAL 4 and CAL 4 follow on the next readout. Finally CAL ID comes high by latching the state held in the storage register as CH 1 ST comes high, in response to the fifth readout. Since release of the calibrate command occurs in the same sequence, all Cal outputs are active for integral multiples of 4 readout intervals (nominally 1 second each).

The instrument is reset on power up and in response to a Mode 2 command. On power up the 10V logic supply charges a capacitor through a series resistor. This triggers a one shot with a moderately long (about .1 second) delay. Next, the INIT line is pulsed. At the end of this pulse On is asserted.

The INIT pulse resets the Cal n output latches and the Readout Counter by triggering another one shot. Also, the Reset Latch is set through an OR gate. Since the readout counter has just been reset, CH 1 ST goes high triggering a chain of one shots. The first pulse transfers a "1" from the Reset Latch to Reset ST. This signal is ANDed with INIT and forces DR 1

high for the duration of the INIT pulse. The second pulse from the chain of one shots clears the Reset Latch. Since Reset ST is still high, DR 2 is pulsed on the first readout. DR 3 and DR 4 follow on the second and third readout, respectively. By the fourth readout all four Digital Data Boards have been cleared. Since CH 1 is readout again, a zero is transferred from the Reset Latch to Reset ST. Initialization is now complete. At this time CH 1 has 3-4 seconds of data, CH 2 has 3, CH 3 has 2 and CH 4 has 1 second of accumulated data.

Exercising the Mode 2 command causes Reset to go high for 1.25 milliseconds. This sets the Reset Latch. Since the command timing is random with respect to the Read signal, implementation is delayed. The first CH 1 readout following the command, sets Reset ST and exercises DR 1 simultaneously with RR 1. The three remaining channels are cleared as they are read out. Reset ST is cleared on the following CH 1 readout.

### 3.2.6 Interface/Monitor Board

Fig. 3.10 is a block diagram of the Interface/Monitor Board. The five differential receivers shown are isolated bilevel Schmitt triggers. Their hysteresis is about 1 volt and they will tolerate  $\pm 5$  V common mode signal with respect to the Dosimeter Chassis.

The monitors, with the exception of Am 2, are referenced to Mon Gnd. This input is isolated by a voltage follower. The digital monitor outputs are standard CMOS buffers with a 2K source resistor added. In order to produce the correct output voltages,  $V_{SS}$  follows Mon Gnd and  $V_{DD} = V_{SS} + 5$ . The status inputs must be level shifted in order to accommodate a  $\pm 5$  V variation in Monitor Ground. Since the level shifter inverts, a 10 V status input results in an output of Mon Gnd - .6 V; whereas a grounded input results in a 10 V output.

In order to float Am 1 and Am 3, the Monitor Voltage ( $V_{OS}$ ) is inverted and applied to the inverting input of two differential amplifiers. The 200 V nominal detector bias ( $V_{bias}$ ) is applied to a 200: 1 divider connected to the non-inverting input of the amplifier which outputs Am 1. As a result the voltage at Am 1 ( $V_{m1}$ ) is as follows:

$$V_{m1} = 2 \left[ \frac{V_{bias}}{200} + \frac{V_{os}}{2} \right] = \frac{1}{100} V_{bias} + V_{os}.$$

Similarly, it follows that  $V_{m3} = 2 V_s + V_{OS}$ , where  $V_s$  is the voltage dropped by the sensistor (shown in Fig. 3.2, nominally 1.1 V @ 25°C) in response to a 0.5 mA current source.

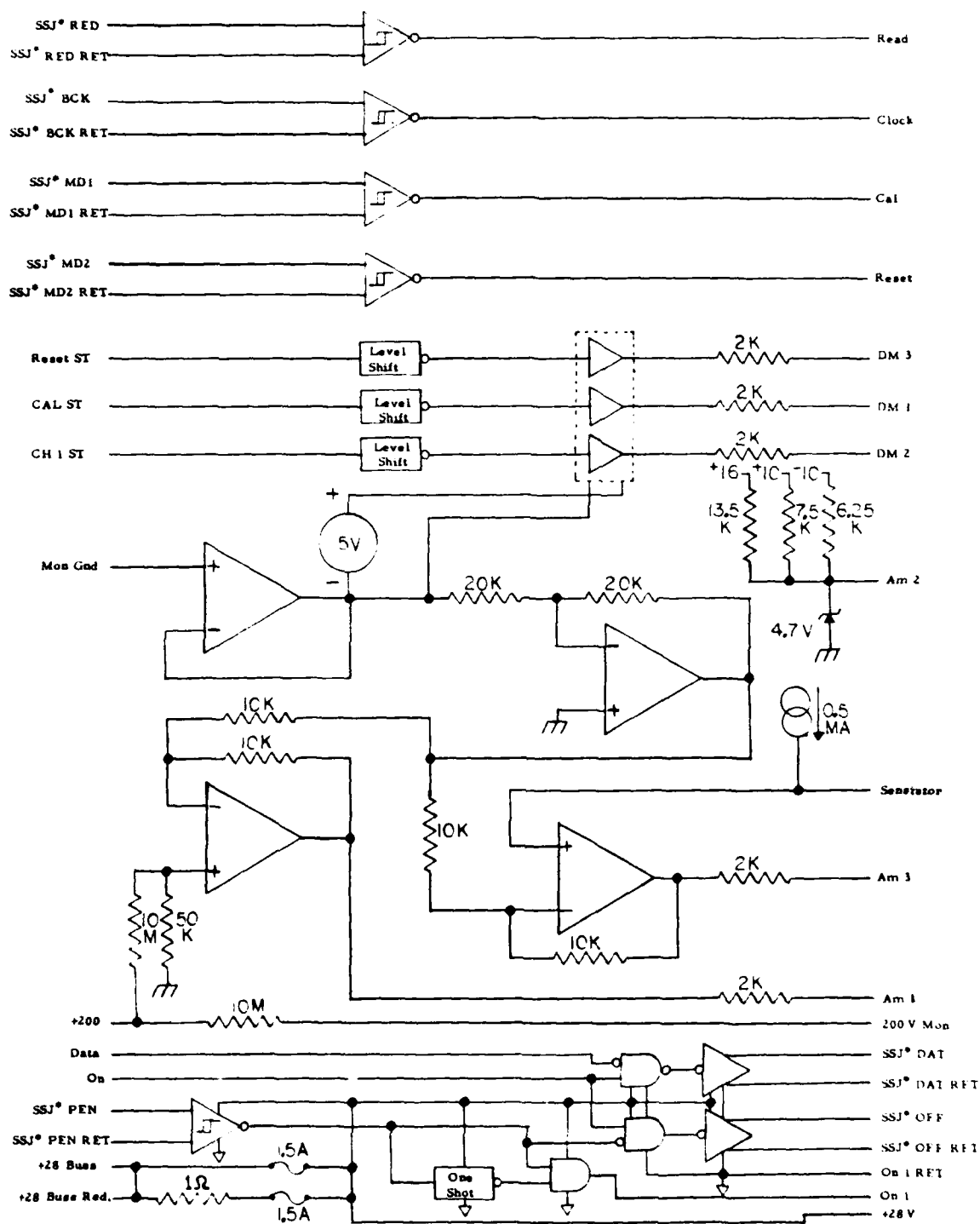


Fig. 3.10 Interface/Monitor Board Block Diagram

Am 2 is the power monitor. If the supply voltages are at their nominal values, one milliamp flows from each of the positive supplies to the -10 V supply. The divider point, Am 2 has an open circuit voltage of 2.5 V. The Zener diode limits the output voltage to  $-.6 \leq \text{Am 2} \leq 4.7$ . This monitor point is not buffered, since a substantial change in either the +16 or -10 V supplies would also affect the Op Amp, making interpretation of the monitor substantially more difficult. As matters stand, the voltage recorded by the spacecraft will include the offset of Mon Gnd with respect to the Dosimeter Chassis.

The output labeled 200 V Mon is a test connection. It has a 10 Meg resistor to limit the current sourced by the bias supply. This also reduces the danger to external circuitry and to personnel.

Operation of the power enable circuitry is as follows: SSJ\* PEN goes high forcing On 1 low and enabling the DC-DC convertor. After a delay, the Digital Control Board confirms that it is powered by sending a 1 to the Interface Monitor Board via On. As a result, SSJ\* OFF goes low to confirm power up, and SSJ\* Dat is enabled. On power down SSJ\* PEN is released, SSJ\* OFF goes high and a one shot is triggered. On 1 remains low until the one shot times out. The DC-DC convertor is disabled as On 1 comes high. As the +10 V supply decays On goes low and forces SSJ\* Dat into a valid zero state.

Primary (or redundant) power enters the instrument at +28 buss and is fused as shown. +28 V powers the DC-DC convertor, the SSJ\* PEN receiver and portions of the SSJ\* OFF and SSJ\* Dat transmitters.

### 3.2.7 DC-DC Convertor

Fig. 3.11 is the block diagram for the DC-DC convertor. The input filter clamps primary buss transients at 43 volts and suppresses the higher frequency components. It also prevents oscillator switching transients from being conducted back into the supply buss. The comparator disables the oscillator if the voltage exceeds about 31 volts. The 820 K resistor provides about .2 volts of hysteresis.

If the buss voltage is within limits, On Test follows On 1 and enables the oscillator. Oscillator output W2 connects the P+ power to the primary center taps of T1 and T3. W1 and W3 alternately conduct to P- thus inducing an alternating magnetic flux in the cores of T1 and T3. The secondary connection to W4 and W5 provides voltage drive to the oscillator, ensuring proper operation under no load conditions.

The  $\pm 10$  Volt outputs are obtained from a center tapped secondary and a full wave bridge rectifier. This is followed by a filter network, a nominal load and output feedthrus. The +16 volt output has the highest



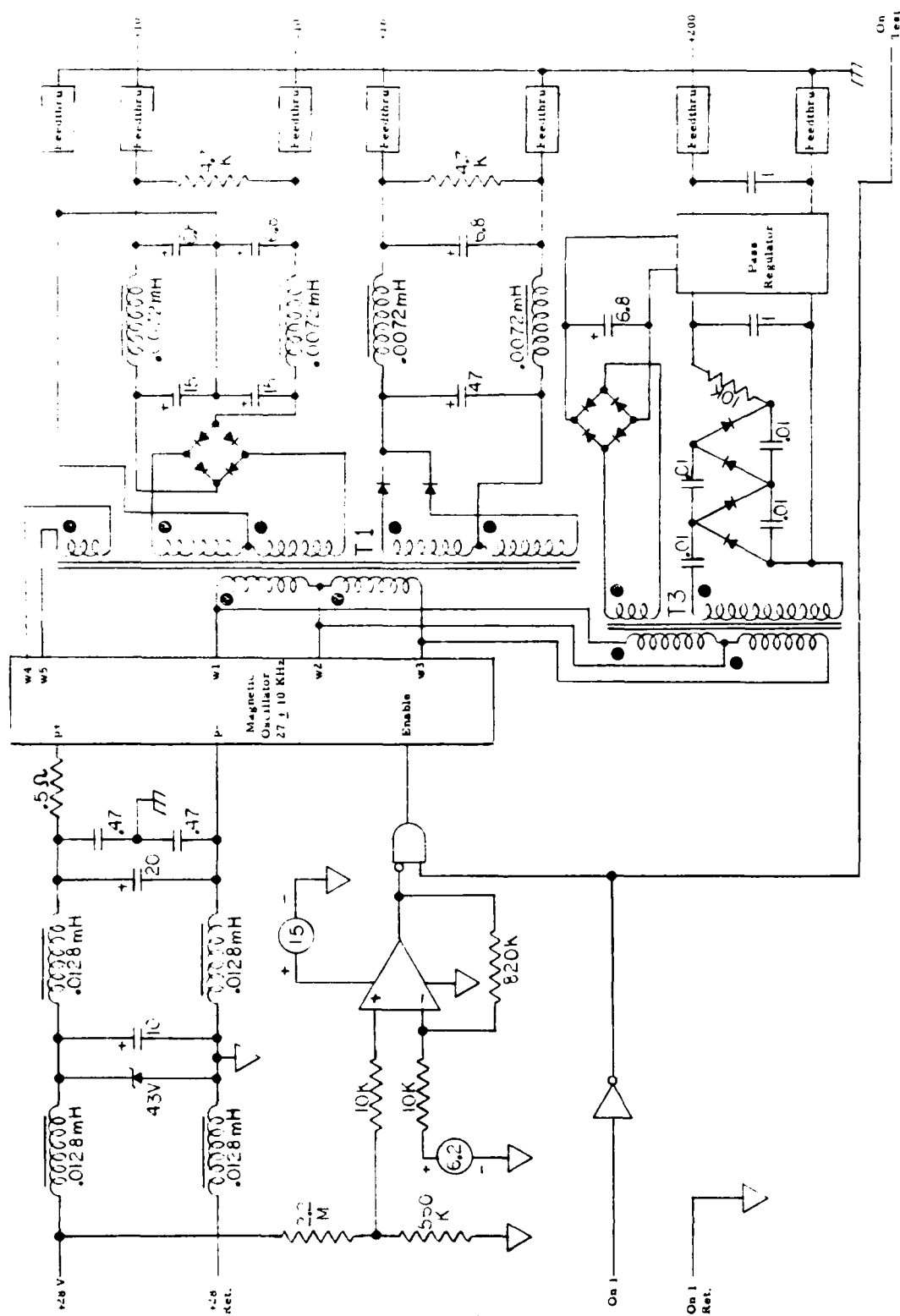


Fig. 3.11 DC-DC Converter Block Diagram

current demand so the split secondary full wave topology used saves the power which would be dissipated in the two additional diodes that a bridge topology would require.

The +200 V output is generated from T3. The upper secondary is rectified and filtered to provide a floating low voltage supply for the pass regulator. The lower secondary drives a voltage quadrupler. Its high voltage output is then regulated down to give the nominal output voltage.

### 3.3 Ground Support Equipment

In addition to the Dosimeter breadboards and flight hardware, several pieces of test equipment were also designed and fabricated. The Test Console simulates the required spacecraft signals, displays the data, monitors various analog and digital signals, and powers the Dosimeter. The Buffer Assembly isolates and provides convenient access to the test signals. A Digitizer Test Controller, and a digital data board tester along with several board test fixtures were also built. This equipment is described in detail in Section 2.3 of the R & D equipment information report (Ref 1.9).

#### 4. OPERATIONAL DESCRIPTION

##### 4.1 Calibration Constants

The four dose channels must be calibrated to provide the  $K_d$  factor in rads (Si)/(output dose count). This allows the telemetered dose counts to be converted directly into total accumulated dose in rads (Si). The channel calibration constant can be calculated from (see Section 2.5.1).

$$K_d \text{ (rads/dose count)} = K_c K / K_e \quad (4.1)$$

where

$$K_c = \text{pulses/dose count} = \text{dose counter prescaler}$$

$$K = \text{rads/MeV (Si)} = 1 / (6.24 \times 10^7 \times M), \text{ where } M \text{ is the detector mass in g.}$$

$$K_e = K_p K_v = \text{pulses/MeV} = \text{dose digitizer conversion factor}$$

The detector properties and channel prescaler counts per output dose count are given in Table 4.1. The listed detector thicknesses are the measured values for the detectors installed in each channel.

Each dosimeter channel has a threshold, 15 digitizer levels, and an upper level for the electron dose (50 keV to 1 MeV energy loss in the detector), and a second set (1 MeV to 10 MeV) for protons, as explained earlier. The electron upper level is the same as the proton lower level and first proton digitizer level. The final values of all thresholds, including the star threshold, and of all digitizer levels, are given in Table 4.2. These values were measured using a precision pulser calibrated from the 5.48 MeV alpha particles from Am-241, and from the 478 keV Compton edge from the 662 keV gamma-rays from Cs-137. The data in Table 4.2 can be used to calculate the channel dose constants  $K_d$  for any given pulse height distribution. The results for a flat spectrum are listed in Table 4.3, along with the nominal design values, which latter have been corrected for the actual detector thicknesses.

Table 4.1  
DOSIMETER Detector Properties  
and Channel Prescaler Values

<u>Channel Designation</u>	<u>Detector Area (cm<sup>2</sup>)</u>	<u>Detector Thickness (microns)</u>	<u>Detector Mass (g)</u>	<u>Dose Counter Prescaler</u>	
				<u>Electron</u>	<u>Proton</u>
D1	0.051	398	$4.73 \times 10^{-3}$	8192	64
D2	1.00	403	$9.39 \times 10^{-2}$	16384	1024
D3	1.00	390	$9.09 \times 10^{-2}$	4096	256
D4	1.00	384	$8.95 \times 10^{-2}$	4096	256

Table 4.2  
Threshold and Digitizer Levels for the Dose Channels

<u>Level Designation</u>	<u>Electron energies (keV)</u>				<u>Proton energies (MeV)</u>			
	<u>D1</u>	<u>D2</u>	<u>D3</u>	<u>D4</u>	<u>D1</u>	<u>D2</u>	<u>D3</u>	<u>D4</u>
LL (e/p)	50	50	50	50	1.005	1.020	1.006	1.013
1	65	65	55	65	1.005	1.020	1.006	1.013
2	135	130	115	135	1.27	1.26	1.26	1.25
3	195	195	185	195	1.88	1.93	1.94	1.92
4	255	255	245	255	2.51	2.55	2.56	2.52
5	320	315	310	320	3.14	3.18	3.20	3.15
6	380	380	375	380	3.77	3.81	3.83	3.78
7	445	440	440	445	4.40	4.44	4.47	4.41
8	505	500	505	505	4.98	5.03	5.07	5.02
9	565	565	570	570	5.59	5.64	5.69	5.64
10	630	625	635	625	6.23	6.29	6.33	6.29
11	690	685	705	690	6.87	6.93	6.98	6.94
12	755	755	770	750	7.51	7.57	7.62	7.57
13	815	820	835	815	8.15	8.20	8.27	8.20
14	880	875	905	875	8.77	8.86	9.03	8.84
15	970	990	-	985	9.59	10.02	-	9.97
e/p (UL)	1005	1020	1006	1013	10.11	10.24	10.12	10.29
Star threshold					40.36	40.27	74.88	40.21

\*Particles of lower energies are classified as electrons, so the lower proton levels are never used.

The calibration constants were also measured directly for the electron channels using a Cs-137 gamma-ray source, and simultaneously measuring the digitizer output count rate and the energy loss spectrum of the corresponding detector. The energy loss spectrum was integrated from the electron threshold (50 keV) to the upper level (about 1 MeV) to give the energy loss in the detector in MeV/sec. The digitizer output count rate in pulses/sec was then divided by the energy loss rate to give the  $K_e$  factor, and the  $K_d$  calibration constant was then calculated from (4.1). The results are listed in Table 4.3, and agree with the digitizer calculations for a flat spectrum to within 7%. The differences arise primarily from the lower average energy loss of the Cs-137 produced spectra and the slight non-linearities in the digitizers from normal component tolerances.

The two lowest shielding channels D1 and D2 were also calibrated with a Sr-Y-90 beta source with a 2.24 MeV end point. The results are also shown in Table 4.3, and agree with the digitizer calculation to 1%.

Table 4.3  
Dose Channel Calibration Constants  
From Different Measurement Methods

<u>Calibration Constant - rads/ (output dose count) - for channel</u>				
<u>Item</u>	<u>D1</u>	<u>D2</u>	<u>D3</u>	<u>D4</u>
<u>Electrons</u>				
Design value (corrected for detector thickness)	$1.73 \times 10^{-3}$	$1.76 \times 10^{-4}$	$4.53 \times 10^{-5}$	$4.62 \times 10^{-5}$
Digitizer level value for a flat spectrum	$1.76 \times 10^{-3}$	$1.77 \times 10^{-4}$	$4.61 \times 10^{-5}$	$4.66 \times 10^{-5}$
Cs-137 gamma ray source value	$1.78 \times 10^{-3}$	$1.81 \times 10^{-4}$	$4.30 \times 10^{-5}$	$4.85 \times 10^{-5}$
Sr-Y-90 beta source value	$1.75 \times 10^{-3}$	$1.78 \times 10^{-4}$	-	-
<u>Protons</u>				
Design value (corrected for detector thickness)	$1.37 \times 10^{-4}$	$1.13 \times 10^{-4}$	$2.84 \times 10^{-5}$	$2.89 \times 10^{-5}$
Digitizer level value for a flat spectrum	$1.36 \times 10^{-4}$	$1.11 \times 10^{-4}$	$2.90 \times 10^{-5}$	$2.92 \times 10^{-5}$

The D2 dome has a nominal 2.5 MeV threshold for electrons, and so responded primarily to bremsstrahlung from the source. This was very evident in the measured count rates of the D1 and D2 detectors for the Sr-Y-90 beta source.

The best values for the channel dose calibration constants are given in Table 4.4. For the electron channels the Cs-137 source calibration values were used. Relativistic (1-10 MeV) electrons lose only about 200 keV, on the average, in the detectors, so the Cs-137 spectrum, with an average energy loss near 200 keV, is a good estimate of the electron response. The good agreement (2%) of the D1 response to Cs-137 and to Sr-Y-90 demonstrates the accuracy of the Cs-137 calibration.

The digitizer level values for a flat spectrum are used for the proton dose calibration constants in Table 4.4. Since the proton energy loss spectrum is expected to be much broader than the electron energy loss spectrum, the flat spectrum value should be more accurate. The calibration constants in Table 4.4 are estimated to be accurate to  $\pm 10\%$  for the expected particle flux conditions to be encountered by the Dosimeter.

Table 4.4  
Final Channel Dose Calibration Constants

<u>Calibration Constant - rads/(output dose count)</u>		
<u>Channel</u>	<u>Electrons</u>	<u>Protons</u>
D1	$1.78 \times 10^{-3}$	$1.36 \times 10^{-4}$
D2	$1.81 \times 10^{-4}$	$1.11 \times 10^{-4}$
D3	$4.30 \times 10^{-5}$	$2.90 \times 10^{-5}$
D4	$4.85 \times 10^{-5}$	$2.92 \times 10^{-5}$

The Dosimeter also has an analog temperature monitor with the output on line Am 3. The temperature monitor has been calibrated over the range  $-55^{\circ}\text{C}$  to  $+125^{\circ}\text{C}$ . The complete calibration curve of monitor output voltage vs temperature is given in Fig. 4.1.

#### 4.2 Operating Instructions

The Dosimeter is designed to remain on continuously in order to measure the total accumulated dose. When the dosimeter power is turned on the dose counters are automatically set to zero, since they contain no

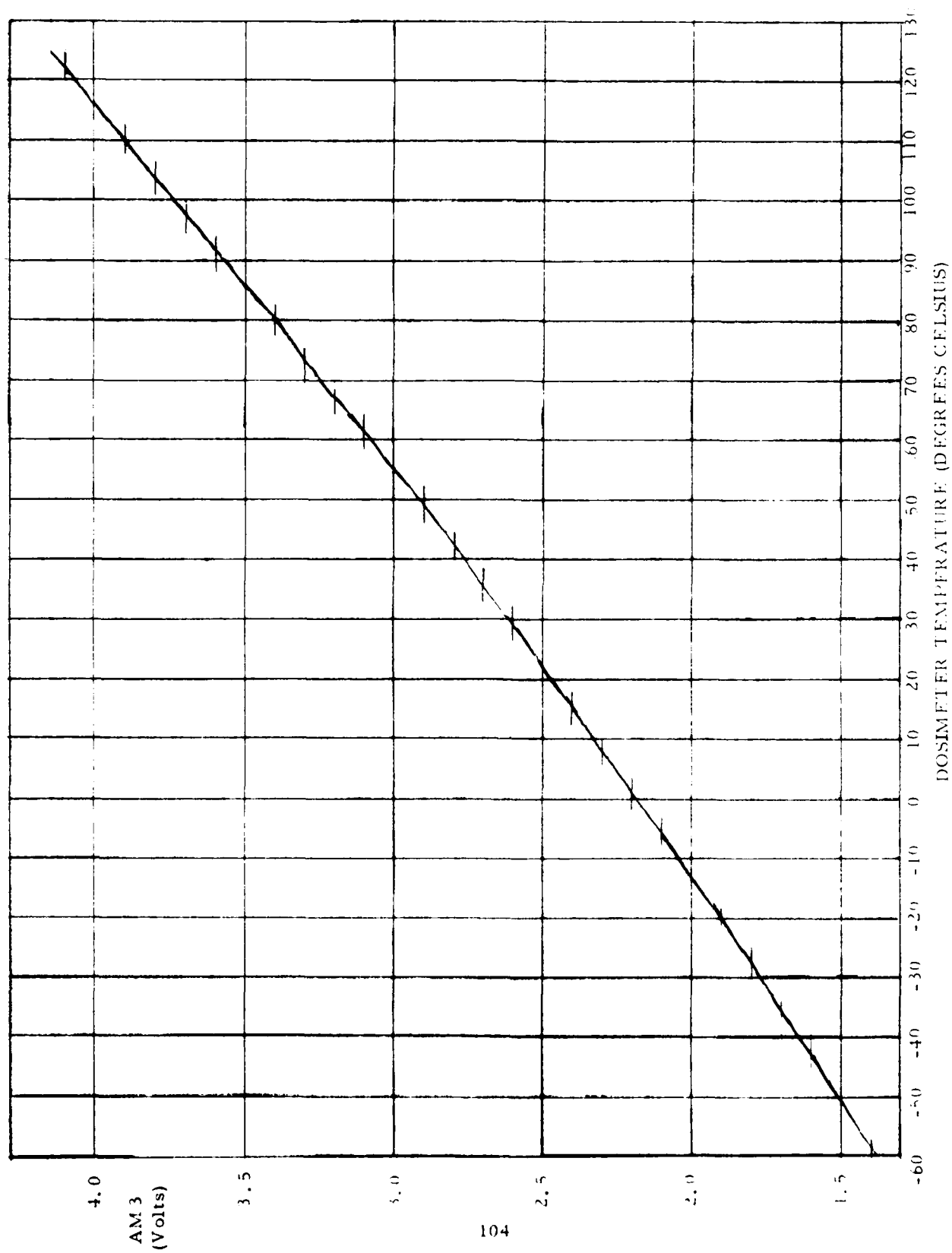


FIG. 4.1 AM 3 VS TEMPERATURE

meaningful data at turn-on. Thereafter the dose counters continue to accumulate total dose from the time of turn-on. The flux counters are reset after each readout, so they provide only a count-rate, i.e. flux, measurement.

The dose counters can be reset by one of two methods. First, a reset command used to reset all four dose counters, and do nothing else. Second, if dosimeter power is turned off, the dose counters are then automatically reset when power is reapplied. The latter mode of dose reset is not a recommended method, but will in no way harm the instrument.

The CAL mode provides information on total depletion of the solid state detectors and on the proper operation of the dosimeter electronics. CAL mode data will be contaminated by any ambient particles producing an energy loss in the detectors of greater than 1 MeV, so it should be activated only during periods of low ambient particle flux. Since the CAL mode disables further accumulation in the total accumulated dose counters, it should be activated only for short periods of time. The dosimeter remains in CAL mode until commanded back into the NORM mode. To avoid inadvertent loss of data by leaving the dosimeter in the CAL mode, the CAL mode operation and subsequent return to NORM mode operation should always be verified in real time operation; i.e. DM1 should go high and B<sub>2</sub> of the serial data should be zero.

The dose counters should not be reset too frequently to avoid complicating the analysis for total dose. The NORM B readouts provide a constant incremental dose reading, providing overflow does not occur. The NORM A readouts provide a constant fractional error in the total accumulated dose, and thus only give a large dose increment resolution at high total accumulated dose. If a finer dose rate resolution is desired when the total accumulated dose is large, then the dose counters should be reset.

#### 4.3 Environmental Precautions

The dosimeter contains four solid state detectors which are sensitive to moisture and chemical contamination. Although the detectors are covered by aluminum dome shields, they are not hermetically sealed and so are subject to degradation by environmental contaminants. It is recommended that prior to launch the dosimeter normally be stored in dry nitrogen, or at least dry air. Exposure to moisture should be absolutely minimized, since moisture can significantly increase detector leakage current, leading to improper detector operation. Exposure to any type of corrosive atmosphere must be avoided, since this could cause permanent damage to the detectors.



The dosimeter can be exposed to normal atmospheric conditions for short periods of time, but it is always best to minimize the exposure to moist atmospheres. When being bled up to atmospheric pressure from vacuum, it is recommended that dry nitrogen be used to avoid introducing moisture into the detector dome volume. Long term storage or shipping should be in a dry nitrogen atmosphere or at least in a sealed container with drying material inside.

#### 4.4 Data Stream Format

The output data format was described in Section 3, and is summarized in Tables 4.5, 4.6, and 4.7. The compression counter assignments for the three modes of data output, NORM A, NORM B, and CAL, are detailed in Table 4.5. Each channel (dome) has the compression counter assignment shown in Table 4.5. The Dosimeter telemetry stream contains one 36-bit data block per second. The breakdown of these 36 bits into mode and channel identification, and into data bits, is shown in Table 4.6. The cycling of mode and channel readouts for Normal Mode Data is shown in Table 4.7. For the CAL mode the only cycling present is from channels 1 to 4, repeated every 4 seconds.

The compression counters for flux are read out completely every four seconds, for all four channels. This is also true for the dose counts in the CAL mode. The dose counts in the Normal Mode require a NORM A and a NORM B readout for the complete ripple plus compression counter output. From Table 4.7 it is seen that a complete NORM A output occurs once every 64 seconds, and is followed by 15 NORM B outputs. The NORM A output provides the dose compression counter exponent and two high-order mantissa bits, giving the total dose to  $\pm 25\%$  at the worst. The NORM B readouts provide the two low-order mantissa bits and the ripple counter bits.

The dose counter prescalers have been selected so that the maximum expected dose rate in the expected orbit is unlikely to change the NORM A readouts by more than 1 low order bit in the mantissa over 64 seconds. Thus for most cases the preceeding NORM A readout is valid for the following 15 NORM B readouts. The exception is when the NORM B readout overflows (all 1's => all 0's) between NORM A readouts. For this case, all NORM B readouts after the overflow use the next following NORM A readout.

Under unusual, and unexpected, conditions of intense dose rate the NORM A readout may change by more than 1 low order bit over the total 64 second readout cycle. This complicates the NORM B interpretation slightly, but the NORM A readouts will always give total dose to  $\pm 25\%$  at the worst. The total dose is still accumulated with complete accuracy, so that after such an intense event the total dose can still be read out to the normal full accuracy.

Table 4.5  
Compression Counter Assignments for the Data

<u>Item</u>	<u>Type Counter*</u>	<u>Bits read out for mode**</u>		
		<u>NORM A</u>	<u>NORM B</u>	<u>CAL</u>
P flux	5 x 3	all 8	all 8	-
E flux	4 x 4	all 8	all 8	-
P dose	4 + 4 x 4	$m_4, m_3, E$	$P, m_2, m_1$	-
E dose	4 + 4 x 4	$m_4, m_3, E$	$P, m_2, m_1$	-
Star flux	5	all 5	all 5	lowest bit (1)
Upper flux	5 x 3	-	-	all 8
Lower flux	4 x 4	-	-	all 8
Upper dose	8	-	-	all 8
Lower dose	8	-	-	all 8

\*Counter types are  $P + M \times E$ ,  $P$  = ripple counter (bits) before the  $M \times E$  compression counter,  $M$  = mantissa (bits), and  $E$  = exponent (bits).

\*\*  $E$  = complete exponent (all bits),  $P$  = complete ripple counter (all bits),  
 $m_4, m_3, m_2, m_1$  = bits of the mantissa  $M$  ( $M = 8m_4 + 4m_3 + 2m_2 + m_1$ ).

Table 4.6  
Breakdown of One Basic 36-bit Data Block

<u>Bit</u> *	<u>Meaning</u>
1	Normal Mode Identification - $\begin{cases} 0 = \text{NORM A MODE} \\ 1 = \text{NORM B MODE} \end{cases}$
2	Calibrate Mode Identification - $\begin{cases} 0 = \text{NORM A or B MODE} \\ 1 = \text{CAL MODE} \end{cases}$
3	Channel (DOME) Identification - $\begin{cases} 0 = \text{Channel (DOME) 2, 3 or 4} \\ 1 = \text{Channel (DOME) 1} \end{cases}$

NORM A MODE		NORM B MODE		CAL MODE	
<u>Bits (1-3) = 00X</u>		<u>Bits (1-3) = 10X</u>		<u>Bits (1-3) = X1X</u>	
<u>Bits</u>	<u>Meaning</u>	<u>Bits</u>	<u>Meaning</u>	<u>Bits</u>	<u>Meaning</u>
4-7	P Dose, exponent	4-5	P Dose, $m_2, m_1$	4-11	Upper CAL Dose
8-9	P Dose, $m_4, m_3$	6-9	P Dose, Ripple Cntr.	12-19	Lower CAL Dose
10-13	E Dose, exponent	10-11	E Dose, $m_2, m_1$	20	Star Flux
14-15	E Dose, $m_4, m_3$	12-15	E Dose, Ripple Cntr.	21-28	Upper CAL Flux
16-20	Star Flux	16-20	Star Flux	29-36	Lower CAL Flux
21-28	P Flux	21-28	P Flux		
29-36	E Flux	29-36	E Flux		

\*Bit 36, the least significant bit of the 36-bit word, is the first bit shifted out of the DOSIMETER in the telemetry stream.

The input counts for a ripple + compression counter are given by

$$C_i = P + R_{ov} [(M + 1/2) 2^E - 1/2 \pm ((1/2) 2^E - 1/2)] \quad (4.2)$$

where P is the ripple count,  $R_{ov}$  the overflow count for the ripple counter, M the mantissa count, and E the exponent count. The count (4.2) gives the average possible input count, with uncertainty range giving the maximum and minimum possible input counts. Where no ripple counter is used  $P = 0$  and  $R_{ov} = 1$ .

Table 4.7  
Breakdown of One Complete Cycle of Normal Mode Data

36-bit word number (also-time lapse in seconds)	Data Content of the 36-bit word	Data Sets
1	NORM A - Channel (Dome) 1	NORM A
2	NORM A - Channel (Dome) 2	
3	NORM A - Channel (Dome) 3	
4	NORM A - Channel (Dome) 4	
5	NORM B - Channel (Dome) 1	NORM B #1
6	NORM B - Channel (Dome) 2	
7	NORM B - Channel (Dome) 3	
8	NORM B - Channel (Dome) 4	
9-12		NORM B #2
61-64		NORM B #15

[Cycle repeats starting at 65 with WORD 1]

The omnidirectional fluxes are given by

$$J_i = C_i / (\Delta T A_{oi}) \text{ particles}/(\text{cm}^2\text{-sec}) \quad (4.3)$$

where  $\Delta T = 4$  seconds is the count time and  $A_{oi}$  is the effective omnidirectional detector area ( $A_{01} = 0.0128 \text{ cm}^2$ ,  $A_{02} = A_{03} = A_{04} = 0.25 \text{ cm}^2$ , for channels (domes) 1 to 4). For the fluxes, the  $C_i$  are derived from the appropriate channel and particle flux count. For the doses the total accumulated dose is given by

$$D_i = C_i K_{di} \text{ rads} \quad (4.4)$$

where  $K_{di}$  for the 8 channel -particle combinations are given in Table 4.4. Dose rates may be obtained by subtracting consecutive measurements and dividing by the time increment (4 seconds).

## 5. CONCLUSIONS AND SUMMARY

A space radiation Dosimeter has been designed, fabricated, calibrated, and integrated into the payload of a DMSP satellite. The Dosimeter measures the total accumulated radiation dose in a solid state detector under four different thicknesses of aluminum shielding. The dose is separated into that from electrons (50 keV to 1 MeV energy deposits) and protons (1 to 10 MeV energy deposits). The four aluminum shields (domes) provide energy thresholds of 1, 2.5, 5, and 10 MeV for electrons, and 20, 35, 51, and 75 MeV for protons. The dose calibration constants for the domes were measured to better than 10% accuracy using a number of radiation sources.

Each Dosimeter dome also measures the integral electron flux, and the proton flux, associated with the corresponding doses. Each dome also has a high energy loss flux channel which counts the rare nuclear star events caused primarily by high energy protons, and the low flux of high energy high- $Z$  cosmic rays (the star flux channels).

The Dosimeter was designed to be usable in any portion of the earth's radiation belts with only minor changes. The fabricated unit had detector areas and prescaler values set for the anticipated 800 km altitude polar orbit of the DMSP satellites. The Dosimeter underwent extensive environmental testing, accurate calibration with radioactive sources, and extensive data on the response to electron and proton beams were taken.

The SSJ\* Dosimeter should provide extensive dose (electron/proton) and flux (electron/proton/star) data after launch. The total accumulated dose is measured, so continuous data coverage is not required; the Dosimeter must, however, remain on at all times. The accumulated dose capacities are such that overflow and recycling should not occur for about one year in the DMSP orbit. The accumulated doses can be reset by ground command should greater dose rate resolution be desired after large doses have been accumulated. Since each overflow/recycle or reset simply requires the addition of a fixed, known dose to the later dose readouts to provide the total accumulated dose, and since such overflows and resets are expected to occur infrequently, the Dosimeter should be able to provide many years of total accumulated dose data.

## REFERENCES

- 1.1 Technical Proposal to Design, Fabricate, Calibrate and Test Space Radiation Dosimeter. Panametrics, Inc. (22 May 1978).
- 1.2 Solicitation F1968-78-R-0129 by Electronic Systems Division (PKR) Air Force Systems Command, USAF Hanscom Air Force Base, MA 01731 to Design, Fabricate, Calibrate and Test a Space Radiation Dosimeter.
- 1.3 R & D Evaluation Report for Design, Fabrication, Calibration, and Testing of a Space Radiation Dosimeter (Panametrics 3 December 1979; Revised 2 July 1980 and 29 September 1980).
- 1.4 Special Sensor/Spacecraft Interface Specification for the Block 5D-2 Configuration of the DMSP System, Spec. No. IS-YD-811A, Code Ident 07868 (30 August 1978).
- 1.5 Special Sensor/OLS Interface Specification for Block 5D-2 Configuration of the DMSP System (IS-YD-817) (January 1975), Change 1 (1 June 1978).
- 1.6 Special Sensor/OLS Interface Specification for the Block 5D-2 Configuration of the DMSP System (9RA6605) Westinghouse Defense & Electronic Systems Center, Baltimore, MD USA
- 1.7 OLS and SSJ\* 5D-2 Sensor Electrical Interface Test (T928532) (3-28-81) Westinghouse
- 1.8 Technical Operating Report, 5D-2 Mission Sensors OLS and J\* Electrical Interface Test (BVS 0989) (24 August 1981) Westinghouse CDRL Item 017A1, Contract F04701-81-C-0033, Task 81-06
- 1.9 R & D Equipment Information Report for Energetic Particle Dosimeter, SSJ\* Sensor for DMSP Satellite Panametrics, Inc. (November 1981).
- 2.1 M. J. Berger and S. M. Seltzer, "Tables of Energy Losses and Ranges of Electrons and Positrons," NASA SP-3012 (1964).
- 2.2 J. F. Janni, "Calculations of Energy Loss, Range, Pathlength, Straggling, Multiple Scattering, and the Probability of Inelastic Nuclear Collisions for 0.1-to 1000 -MeV Protons," AFWL-TR-65-150 (Sept. 1966).

# REFERENCES (Continued)

- 2.3 A. L. Vampola, J. B. Blake, and G. A. Paulikas, "A New Study of the Outer Zone Electron Environment: A Hazard to CMOS," SAMS0-TR-77-127. (June, 1977).
- 2.4 J. W. Wilson and F. M. Denn, "Implications of Outer-Zone Radiations on Operations in the Geostationary Region Utilizing the AE4 Environmental Model," NASA TN D-8416 (May, 1977).
- 2.5 K. W. Chan, D. M. Sawyer, and J. I. Vette, "Trapped Radiation Population," Section 4 in "The Trapped Radiation Handbook," J. B. Cladis, G. T. Davidson, and L. L. Newkirk, Compilers and Editors-in-Chief, DNA 2524H (up to -Change 5, 21 Jan. 1977).
- 2.6 E. G. Stassinopoulos, and J. H. King, "An Empirical Model of Energetic Solar Proton Fluxes with Applications to Earth Orbiting Spacecraft," NASA/GSFC X-601-72-489 (Dec. 1972).
- 2.7 F. S. Mozer, D. D. Elliott, J. D. Mihalov, G. A. Paulikas, A. L. Vampola, and S. C. Freden, "Preliminary Analysis of the Fluxes and Spectrums of Trapped Particles after the Nuclear Test of July 9, 1962," J. Geophys. Res. 68, 641-9 (1963).
- 2.8 G. A. Paulikas, and S. C. Freden, "Precipitation of Energetic Electrons into the Atmosphere," J. Geophys. Res. 69, 1239-49 (1964).
- 2.9 S. C. Freden, and G. A. Paulikas, "Trapped Protons at Low Altitudes in the South Atlantic Magnetic Anomaly," J. Geophys. Res. 69, 1259-69 (1964).
- 2.10 S. C. Freden, J. B. Blake, and G. A. Paulikas, "Spatial Variation of the Inner Zone Trapped Proton Spectrum," J. Geophys. Res. 70, 3113-6 (1965).
- 2.11 G. A. Paulikas, J. B. Blake, and S. C. Freden, "Inner-Zone Electrons in 1964 and 1965," J. Geophys. Res. 72, 2011-20 (1967).
- 2.12 G. A. Paulikas, J. B. Blake, and S. S. Imamoto, "ATS-6 Energetic Particle Radiation Measurement at Synchronous Altitude," IEEE Trans. Aerospace and Electronic Systems, AES-11, no. 6, 1138-44 (Nov. 1975).

## REFERENCES (Continued)

- 2.13 S. A. Gary and R. E. Cashion, "Solar Proton Monitor for TIROS-M and ITOS Spacecraft," COM-73-10138 (Dec. 1971).
- 2.14 Solar-Geophysical Data, Descriptive Text, No. 318 (Supplement) (Feb. 1971), U.S. Dept. of Commerce (Boulder, Colo., U.S.A. 80302), Solar Cosmic Ray Protons, pp. 52-56.
- 2.15 R. N. Grubb, "The SMS/GOES Space Environment Monitor Subsystem," NOAA TM ERL SEL-42 (Dec. 1975).
- 2.16 TRW Defense and Space Systems Group, "Space Instruments and Experiments," Brochure which includes a description of a radiation dosimeter.
- 2.17 R. A. Cliff, V. Danchenko, E. G. Stassinopoulos, M. Sing, G. J. Brucker, and R. S. Ohanian, "Prediction and Measurement of Radiation Damage to CMOS Devices on Board Spacecraft," IEE Trans. Nucl. Sci. NS-23, No. 6, 1781-8 (Dec. 1976).
- 2.18 G. Keil, "A Semiconductor Detector for Low Energy Particle and Quantum Spectroscopy at Room Temperature," Nucl. Instr. and Meth. 78, 213-8 (1970).
- 2.19 I. B. McDiarmid, E. E. Budzinski, B. A. Whalen, and N. Sckopke, "Rocket Observations of Electron Pitch-Angle Distributions during Auroral Substorms," Can. J. Phys. 45, 1755-69 (1967).
- 2.20 M. J. Berger and S. M. Seltzer, "Additional Stopping Power and Range Tables for Protons, Mesons, and Electrons," NASA SP-3036 (1966).
- 2.21 Pruett, R. G., Comparison of DMSP and NTS-2 Dosimeter Measurements with Predictions, J. Spacecraft 17, 270-74 (1980).



LINE

DATE  
FILME

04-8

DTIC